UNIVERSITY OF GENOVA

POLYTECHNIC SCHOOL

DIME

Department of Mechanical, Energy, Management and Transportation Engineering

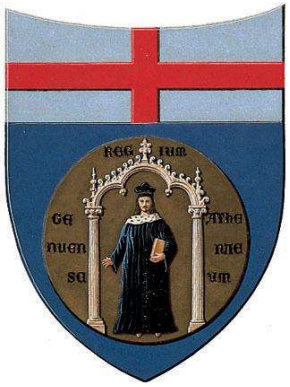

Ph.D. THESIS

Investigation of Laminar Separation Bubble on Flat Plate with Adverse Pressure Gradient

Supervisor:

Prof. Ing. Pietro Zunino

Co Supervisor:

Prof. Ing. Daniele Simoni

Ing. Dario Barsi

Candidate:

Yonglei Qu

May 2020

Declaration

I hereby declare that except where specific reference is made to the work of others, the contents of this dissertation are original and have not been submitted in whole or in part for consideration for any other degree or qualification in this, or any other university. This dissertation is my own work and contains nothing which is the outcome of work done in collaboration with others, except as specified in the text and Acknowledgements.

Yonglei Qu
May 2020

Abstract

The performance of turbomachinery blade profiles, at low Reynolds numbers, is influenced by Laminar Separation Bubbles (LSB). Such a bubble is caused by a strong adverse pressure gradient (APG), and it makes the laminar boundary layer to separate from the curved profile surface, before it becomes turbulent. The present dissertation consists on a joint experimental and numerical investigation on a flat plate with adverse pressure gradient. The experiment provides detailed results including distribution of wall pressure coefficient and boundary layer velocity and turbulence profiles for several values of typical influencing parameters on the behavior of the flow phenomena: Reynolds number, freestream turbulence intensity and end-wall opening angle, which determines the adverse pressure gradient intensity. The numerical work consists on carrying out a systematic analysis, both with Reynolds Average Navier-Stokes (RANS) and Unsteady Reynolds Average Navier-Stokes (URANS) simulations. The results of the numerical simulations are critically investigated and compared with the experimental ones in order to understand the effect of the main physical parameters on the LSB behavior. For RANS simulations, different turbulence and transition models are compared at first to identify the adaptability to the flow phenomena; then, the influence of the three aforementioned parameters on the LSB behavior, is investigated under a typical aggressive adverse pressure gradient. Boundary layer integral parameters are discussed for the different cases in order to understand the flow phenomena in terms of flow time-mean properties. For URANS simulations, the analysis focuses on the surveys of the instantaneous velocity vector, normalized velocity and vorticity maps to highlight the dynamics of the large-scale structures shedding from the bubble maximum thickness position. In addition, the response of shedding vortex phenomenon to the variation of Reynolds number and freestream turbulence intensity under fixed APG condition is also systematically investigated. By quantifying the spatial wavelength and frequency of shedding vortices with FFT (Fast Fourier Transport) to analyze the dynamic influence factor to K-H instability progress.

Acknowledgments

Towards the end of the present work, my heart is full of mixed feelings. The moment when I just came to this faraway and strange city three years ago, seems it was just yesterday. Nowadays, when I am about to hand in my answers to the more than 1000 days and nights of studying abroad, my heart is full of perturbed and expectation.

It's very lucky for me to meet Prof. Pietro Zunino at a critical moment in my life. He generously provided me with the opportunity to study in Italy, which enriched my life experience by enabling me to appreciate European culture while studying. During my Ph. D. course, the honorific professor not only imparted me abundant professional knowledge, but also trained me good scientific literacy and improved my ability to engage in scientific research. Prof. Pietro Zunino also gave me careful guidance and helped me in the process of choosing topics, implementing research and writing a doctoral dissertation. Especially for the cultivation of logical thinking ability of scientific problems, I have gained a lot. In life, he is my mentor and friend, giving me meticulous care, let me experience the pure flavor of Italian life. I would like to express my sincerest thanks to Prof. Pietro Zunino.

Great thanks to the assistant tutors who helped me selflessly in my study, Prof. Daniele Simoni and Ing. Dario Barsi, they inspired me a lot in my thesis work. Prof. Daniele Simoni is a scholar with rich knowledge and practical experience. The experimental part of dissertation is completed under his guidance. His quick thinking, rigorous logic and strong scientific research ability impressed me deeply, and I am very fortunate to work with such a handsome Italian man who looks like Elvis Presley. Ing. Dario Barsi has a solid theoretical foundation and rich experience in numerical simulation. When I encounter bottlenecks in the process of research, he helps me to solve many difficulties, which has greatly benefited me in numerical simulation. His excellent academic report is a good example for me to improve my ability of academic expression.

Many thanks to the teachers and friends of College DIME who worked with me together. Prof. Marina Ubaldi and Prof. Francesca Satta's courses have enabled me to systematically learn professional theoretical knowledge, laying the foundation for future work. Dr. Matteo Dellacasagrande has greatly helped me with my experimental work and data processing, improving my ability to analyze data. Thank all the teachers of DIME College, I can't list them all here. Also, thank the University of Genoa for providing me with valuable learning opportunities.

Many thanks to Harbin Engineering University of China for providing support and encouragement for my international exchanges!

Thank you for studying in Genoa with me together: Prof. Tao Sun, Dr. Lianfeng Yang, Dr. Aoyu Ren and so on. I don't feel lonely with yours help and accompany.

Special thanks to my best loved relatives, especially my wife Nan Zhang and my son Yifan Qu. Thousands of rivers and mountains cannot block my yearning for you. However, yours support and care force and encourage me keep on moving forward!

Contents

Declaration I
Abstract II
Acknowledgments..... III
Chapter 1 Introductions 1
1.1 The Phenomena of Laminar Separation Bubble 1
1.2 Consequences of LSB 2
1.3 Effect on Turbomachinery 3
1.4 Brief Summary of Previous Research 4
1.5 Objectives of the Thesis 6
Chapter 2 Fundamentals of Boundary Layer Theory 9
2.1 Boundary Layer Concept 9
2.2 Boundary Layer on a Flat Plate at Zero Incidence 12
2.2.1 Laminar flow 13
2.2.2 Turbulent flow 15
2.2.3 Viscous sublayer 15
2.3 Boundary Layer on an Airfoil 17
2.4 Boundary Layer Separation 18
2.5 Boundary Layer Integral Parameters 20
2.6 Transition Mechanisms 23
2.6.1 Natural transition 25
2.6.2 Bypass transition 26
2.6.3 Separation induced transition 26
2.6.4 Wake induced transition 28
2.7 Stability Theory 29
Chapter 3 Numerical Method 31
3.1 Governing Equations 32
3.2 RANS Simulation 33
3.3 Turbulence and Transition Models 35
3.3.1 Shear Stress Transport （SST $k-\omega$） model 36
3.3.2 Transition Shear Stress Transport model 39
3.3.3 Transition $k-kl-\omega$ model 41
3.4 Unsteady RANS (URANS) Simulation 45

3.5 Summary 46
Chapter 4 Experimental Research of LSB 47
4.1 Introduction 47
4.2 Test Section 48
4.3 Measurements Setting and Test Matrix 50
4.3.1 LDV measurements for defining boundary conditions 51
4.3.2 Field measurements by TR-PIV in the time varying boundary layer 51
4.3.3 Main overall influence parameters 52
4.4 Phenomenological Analysis of Transition Mechanisms 52
4.4.1 Time-averaged flow field 52
4.4.2 The dynamics performance of LSB 56
4.5 Summary 59
Chapter 5 Numerical Investigation of LSB 60
5.1 Introduction 60
5.2 Computational Domain and Mesh Independency 60
5.3 Mathematical Scheme 62
5.4 Validation of Turbulence Models 63
5.5 Analysis of RANS Results 68
5.5.1 Analysis of APG D12-7 68
5.5.2 Effect of APG on LSB Characteristics 80
5.5.3 Effect of incidence angle on LSB characteristics 81
5.6 Analysis of URANS Results 82
5.6.1 The choice of time step size 82
5.6.2 Dynamic analysis of URANS results 83
5.6.3 Vortex shedding procedure 86
5.6.4 The influence of flow parameters 89
5.6.5 The difference between RANS and URANS simulation 96
5.7 Summary 97
Chapter 6 Conclusions 99
References 101
Nomenclature 108
Appendix A 110
Appendix B 113

Chapter 1

Introduction

Under conditions of low Reynolds numbers, Laminar Separation Bubble (LSB) may occur in a wide range of engineering applications, such as turbomachinery blade profiles and airplane airfoils, hence the performance of these external flow aerodynamics is strongly influenced by LSB.

1.1 The Phenomena of Laminar Separation Bubble

A laminar separation bubble is formed when the previously attached laminar boundary layer encounters an Adverse Pressure Gradient (APG) of sufficient magnitude to cause the flow to separate from the profile surface, before it becomes turbulent. A typical schematic diagram of the LSB with turbulent transition is depicted in Fig. 1.1 [1]. When the LSB occurs in the part near to the profile or airfoil surface, the boundary layer flow can be roughly divided into two main regions.

The first region is bounded by the mean dividing streamline and the wall surface, which represents the relatively slow re-circulatory flow and forming the bubble. The mean dividing streamline is generally regarded as the collection of points across each velocity profile at which the integrated mass flow is zero, and its two intersections with the wall are recognized as “Separation” point and “Reattachment” point, respectively. The second flow region consists of the free shear layer contained between the outer edge of the boundary layer and the dividing streamline. This separated shear layer undergoes transition at a location denoted by “Transition” point due to disturbance amplification occurring in the unstable laminar layer. Momentum transfer due to turbulent mixing eventually eliminates the reverse flow near the wall and the flow reattaches at reattachment point. However, the LSB is also composed of two regions along the flow direction: laminar (separation-transition) and turbulent (transition-reattachment), separately. This process of separation, transition and reattachment results in a LSB that has a predominate effect on the entire profile or airfoil flow field.

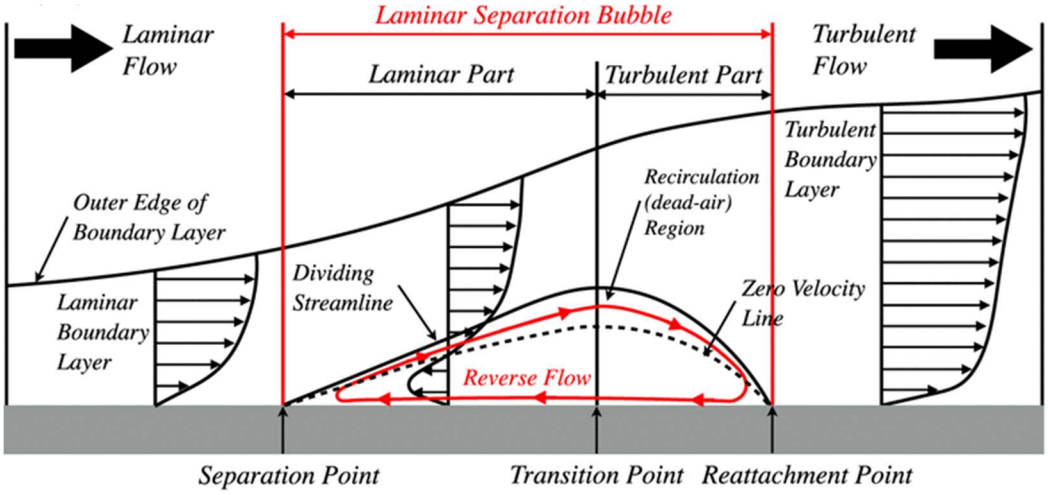

Fig. 1.1 – Structure of Laminar Separation Bubble

The behavior of the separated laminar shear layer strongly influenced the flow development after the detachment point. When the transition to turbulence appears shortly after the separation point due to the instability of the shear layer, the entrainment with the external flow increases, and thus reattachment to the surface is caused, hence a relatively stagnant flow region is formed, that is a short bubble. Under specific conditions that the adverse pressure gradient cannot be overcome, the reattachment delays or fails, which means a long bubble or an open bubble (completely separated flow) is formed. Although the difference between a short bubble and a long bubble is difficult to determine, the formation of a long bubble reorganizes the pressure distribution over the profile or airfoil surface more obviously than that does by a short type. Hence the effect on the pressure distribution is different in the two cases: local and limited in the case of a short bubble, but more influential for a long bubble.

1.2 Consequences of LSB

LSB is caused by a strong adverse pressure gradient, and usually it makes the laminar boundary layer to separate from the curved profile surface, hence it can have large, negative aerodynamic effects. Generally, an increasing boundary layer thickness together with additional drag will be induced due to the displacement of the outer flow, which results in decreased suction over the forward portion of profile and reduced pressure recovery in the rear parts. The drag increment can be several times than that of the airfoil without a separation bubble. Lift and moment are also influenced by a laminar separation bubble, which can lead to problems with stability, especially to blades of turbomachinery, both in compressors and turbines. The key influence factor to the increasing of pressure drag is the geometry parameter of the LSB, especially its thickness in the normal direction to the profile surface. Moreover, a more dramatic effect will occur once the transition process in the separated shear layer is relatively slow and the adverse pressure gradient is relevant. Proceeding to the next step, turbulent momentum transport is not sufficient to close the bubble and a large separation occurs that extends right to the trailing edge. This causes a sudden loss of lift and a strong increase of drag along with significant hysteresis effects of force coefficients with varying angle of attack [2]. Fig. 1.2 shows the pressure coefficient (Cp) distributions along the profile surface, both with and without LSB. The obvious difference between two curves corresponds to a reduced pressure recovery in the LSB region. Out of this portion, they are highly coinciding. Meanwhile, the velocity profiles indicate an increasing trend of boundary layer thickness along the main flow direction.

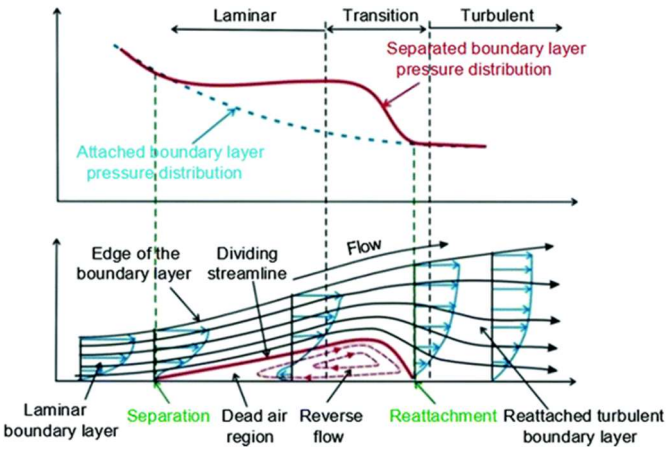

Fig. 1.2 – Cp distributions along the profile surface

1.3 Effect on Turbomachinery

The performance of blade profiles for turbomachinery components is strongly influenced by many aerodynamic phenomena. Among them, LSB is of primary importance for Low-Pressure Turbines and Compressors (LPT and LPC) applications, especially when high-lift profiles operating at low Reynolds number conditions are considered. Hence, the aerodynamic design of LPT and LPC profiles needs an accurate prediction of the transition onset as well as of the separation extension in order to avoid the risk of performance deterioration due to the flow separation, which may occur at low Reynolds numbers.
The fluid mechanics of the flow around compressor and turbine blades are especially complicated, due to leading-edge and suction-side curvature, strong pressure gradients and the complexity of the free-stream or passage flow above the boundary layer. In a low-pressure stage of turbomachinery, the Reynolds number is relatively modest, and the flow may be transitional over a significant proportion of the blade, especially in a turbine stage. Transition thus frequently occurs on the aft part of the blade, encouraged by migrating wakes and free-stream turbulence. In very recent turbomachine designs, the number of blades is lower than in earlier configurations, in order to reduce weight and costs, thus requiring an increase of the loading on each blade. As a result, the suction-side boundary layer is more prone to separation, particularly in the compressor stage. The separated shear layer then usually becomes turbulent soon after separation and reattaches quickly, usually upstream of the trailing edge. The separation bubble formed as a consequence of this process alters the effective shape of the blade, thus degrading the blade performances and increasing losses. The transition process is especially sensitive to free-stream turbulence, with increasing levels resulting in earlier reattachment and a reduction in the length of the recirculation bubble. This interaction is thus especially important to capture in any prediction procedure.

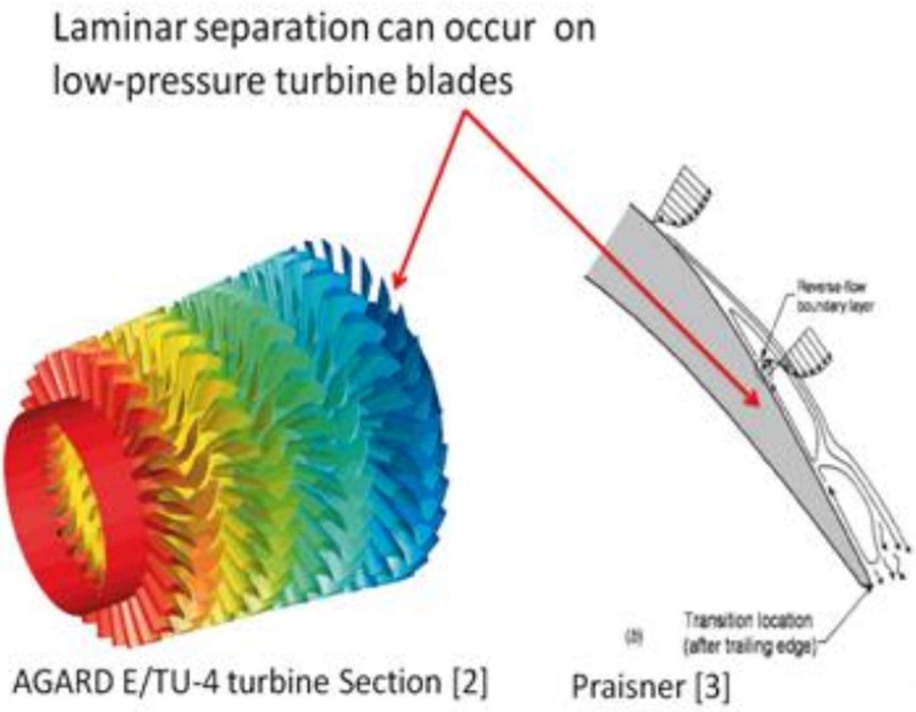

Fig. 1.3 – LSB possible position in turbomachinery

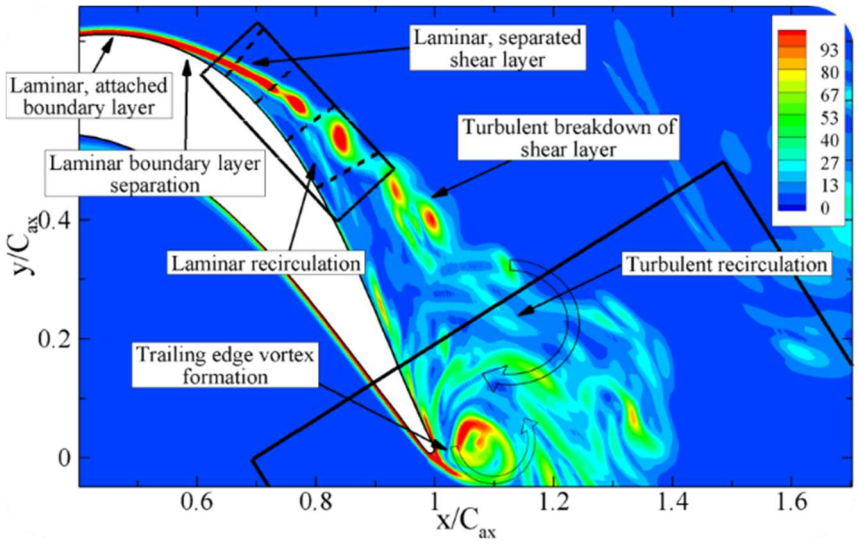

Fig. 1.4 – Influence of LSB to the LPT flow field

The possible position that LSB occurs in typical turbomachinery is plotted in Fig. 1.3. While figure Fig. 1.4 describes the influence of LSB to the LPT flow field. On the suction side of turbine blade, the separation of the boundary layer creates a large circulation area that extends downstream, on the other hand, it breaks down the boundary shear layer. A shedding vortex is also formed at the trailing edge, which brings negative influence to the downstream flow field.

1.4 Brief Summary of Previous Research

Based on the investigations on the stalling progress of airfoils, the existence of LSB together with the influence on an airfoil was proposed by Jones [3]. Gault [4, 5] further investigated the behavior of LSB close to stall conditions, and recognized LSBs into three types, which corresponding to leading edge, trailing edge and thin airfoil stall, respectively. In fact, the most important and notable meaningful research works for later investigations of LSB were done by Gaster [6]. Tremendous bubbles were produced on a flat plate surface in order to understand LSB's structure and behavior meticulously. By means of place an auxiliary airfoil in upside-down position above the flat plate, the preferred adverse pressure gradient was created; thus, this configuration allowed Gaster to carry out pressure and hot-wire measurements of many bubbles, corresponding to different Reynolds number and pressure gradients. The results of Gaster's investigation show that LSB can be short, long or open, depending on the various Reynolds number, the adverse pressure gradient and the freestream turbulence. Meanwhile, two non-dimensional parameters, such as separation Reynolds number and pressure gradient parameter, are also proposed by Gaster as criterions to quantify the bursting onset. Tollmien-Schlichting instabilities are observed during the turbulence measurements progress, which gives us an insight to the oscillation of LSB bursting.

Hatman and Wang et al. [7-10] also described the transition progress induced by separation bubble, with the classification based on the effect of the bubble on the static pressure distribution. For stable freestream conditions (both turbulence intensity and adverse pressure gradient), the bubble size increases as Reynolds number reducing, while the progress of

bursting means the transform from a short bubble to a long one. Once the extreme low Reynolds number is reached, a massive separation will take place without reattachment downstream, that means an open separation occur; thus, the lower the Reynolds number is, more the losses and lower the efficiency [11]. In a short bubble case, a weak perturbation to the pressure distribution will be caused and the suction peak is also retained, which is proportional to the increasing of attack angle of the flow. On the contrary, a long type bubble has the capability to alter the pressure distribution greatly by emerge the suction peak on the surface.

Based on the results of Gaster, Horton [12] developed a semi-empirical bubble model, which combined the advances in both laminar [13] and turbulent [14] boundary layer theory, as subscribed previously in Fig. 1.1 and Fig. 1.2. In the subsequent decades, more semi-empirical models were proposed from Horton's model, but the physical descriptions of the LSB are quite same according to the original one. Meanwhile, an obvious shortcoming of these semi-empirical models is the failure of predicting the structure of LSB in all conditions, including the behavior when it is close to the stall condition. Therefore, it clearly shows that the semi-empirical model is lack of the capability in capturing the bubble's physical progress. In Horton's theory, a fully turbulent flow is obtained in the reattachment region of LSB, also any fluctuation at detachment position and in the laminar portion of the bubble should be neglected, which is different from the experimental data, especially the separation bubble behavior at low Reynolds number. Hence these differences further indicate that if the physical processes involved cannot be understood, the obtained models are still inadequate. Thanks to the progress of both experimental methods and numerical simulation technology, many achievements have been made in the following study of the unsteady characteristics of separation bubbles and the influence of freestream, which further improves the understanding of LSB model.

In fact, the low frequency oscillations of separation bubbles have been observed in Gaster's experiments. These oscillations are more evident in the low Reynolds number range, i.e. corresponding to long types of laminar separation bubbles. Compared with the shorter type ones, a high frequency turbulent region can be formed intermittently in the early transition stage of the long separation bubble, which makes the continuous turbulent signal develops downstream. Gleyzes used visualization method to study the condition of ONERA LC-100-D airfoil with Reynolds number more than 500000, and analyzed the transition characteristics of the airfoil surface flow. The results show that a clear vortical structure is formed in the rear region of the separated bubbles on the airfoil and can be maintained continuously in the subsequent turbulence, which is considered to be the first stage performance of the development in the turbulent boundary layer. Although similar investigations have been done in the works of B. Carmichael [15] and P. B. S. Lissaman [16], the correlation between these vortical structures, hence the characteristics of the turbulent boundary layer behind bubbles are not further understood at that time.

In contrast, although the transition mechanism in laminar bubbles and the correlation of the degree and substance of flow disturbances to the transition process are still controversial, more studies on instability and transition in separated bubbles have been carried out by researchers [17,18]. In the early 1990s, it was still difficult to accurately measure the unstable structures in laminar separation bubbles. Thanks to the advances in computational methods, numerical simulation began to be more used to study the characteristics of unsteady separation bubbles. Using an unsteady laminar Navier-Stokes solver, Pauley [19] reproduced Gaster's experiment by simulation numerically. Based on the vortex shedding phenomenon from shear layer separated laminar flow, she confirmed the flow structure mentioned above.

The results of both time-averaged and unsteady flow show that the pressure distributions on the surface are consistent with the discovery of Gaster, and the streamlines also present the classical separation bubble closure mode under steady conditions. At the same time, the numerical simulation of Eppler 387 profile also shows a similar regulation. Pauley believes that one of the possible reasons for this phenomenon is that the measurement used in the experiment at that time was static, hence when the turbulent fluctuation frequency is higher than the natural frequency of the instrument, it cannot reflect these unsteady processes, which is equivalent to the measurement link itself has the characteristics of filtering. Similar numerical simulation results also confirm the shedding vortices of separation bubbles, such as Tatineni's [20] research on APEX airfoil and so on. Although these studies are based on two-dimensional flows, the effect of small-scale turbulent vortices cannot be fully considered, the results obtained clearly show that the laminar part of bubble is not a region of static flow, but a region that can be adequately defined and periodically shedding vortices. These structures have the ability to strongly influence the subsequent turbulence and transition processes. Based on these results, it is generally considered that the assumption of transition at laminar separation point [21] is inadequate, and the prediction of transition occurrence is more challenging [22].

Whether the rupture of separation bubble is caused by the changes of their own stability characteristics or by the external potential flow [6], which is related to the overall stability of the flow, is still not a unified conclusion. However, the unstable characteristics of laminar separation bubbles play an important role in correctly analysing the bubble's bursting problem. In the traditional steady laminar separation bubble model, the bursting of the separation bubble can be considered as instantaneous rupture (in the case of long separation bubble) or definitive rupture (in the case of leading-edge stall) in the process of turbulent shear layer reattachment. Therefore, in this model, the bursting of separation bubbles can be defined as the failure of the turbulent shear layer reattachment process. However, the model failed to explain the different flow patterns (thin airfoil stall and leading-edge stall) caused by the breakdown of separation bubbles, nor can it successfully predict the occurrence of breakdown. Although it is believed that the strong unstable structure of separation bubbles may be a clue to a better understanding of the problem, it is still not clear that how unstable behavior affects the emergence of ruptures. Early results of Pauley [23] suggested that long separation bubbles were stable, while short separation bubbles were unstable. Meanwhile, the end of unstable behavior marks the emergence of bursting. But Pauley's following work [24,25] denied the view that the vortices shedding from long separation bubbles were stronger than those corresponding to short ones. In the numerical simulation study completed by Alam [26], laminar separation bubbles are analysed by DNS, and it is considered that bursting can be used as a criterion to distinguish relatively unstable short separation bubbles from absolutely unstable long separation bubbles, which mainly depends on the amount of reflux. But they only analysed short and small type of separated bubbles, which was not enough to support their argument. On the other hand, the similar DNS studies of separation bubbles in literature [27] show that even a small type of separation bubbles exhibits absolute instability.

1.5 Objectives of the Thesis

With the development of research methods, the flow mechanism of laminar separation bubbles is being more and more understood. The influence of laminar separation bubbles on turbomachinery, especially on aerodynamic performance in low pressure environment, and control measures have also been developed rapidly. Overall, the development trend of

modern Civil Aero-engine is to reduce emissions and fuel consumption as much as possible on the basis of ensuring power and efficiency, which requires the weight of each component of the whole propulsion system to be reduced. In order to achieve this goal, designers can usually shorten the length of the intermediate turbine diffuser, which developing towards aggressive or ultra-aggressive geometric design, or reduce the number of Low-Pressure Turbine blades, according to the reason that Low-Pressure Turbine accounts for a large proportion of the total engine weight. Although reducing the weight of Low-Pressure Turbine can also decrease manufacturing costs, it also means that fewer blades are used to ensure the same stage processing capacity and efficiency, that is, the remaining blades will have higher aerodynamic loading, thus increasing the risk of stall. While providing high lift, the working environment of suction side of modern Low-Pressure Turbine blades also face stronger adverse pressure gradient and lower flow Reynolds number. Under cruise condition, the Reynolds number is about 100000. At this time, the boundary layer on the suction side is laminar, and the strong adverse pressure gradient cannot be overcome. Finally, the separation of the boundary layer is formed, and then bubbles' separation is induced in the laminar-turbulent transition portion. In the investigation of Mayle [11], the laminar-turbulent transition process and its role in the aerodynamic performance of modern gas turbine devices are described. Its follow-up work and the researches of Hatman and Wang [10] put forward some concepts such as empirical correction formula and intermittency function for the occurrence of transition. Curtis et al. [28] studied the loss caused by the development of boundary layer on the suction side of turbine blade, and analyzed its influence on the overall loss of gas turbine. These works play an important role in correctly predicting the evolution of separation and transition phenomena, also for designing new high-lift and high efficiency blade profiles. A large number of modern research works are carried out in order to systematically investigate the mechanism of the separation in laminar boundary layer flow nowadays, including theoretical researches, experiments and numerical simulations.

In recent years, both experimental and numerical simulation methods for boundary layer flow have been greatly improved, which provides an effective means to study the internal flow in detail, also to deepen the understanding of the flow mechanism. In the field of experimental research, high-precision measuring equipment has been put into a lot of research work, including Hot-Wire (HW) anemometer with high response speed, Laser Doppler Velocimetry (LDV) with high resolution and Particle Image Velocimetry (PIV), etc. At the same time, more reasonable data post-processing has also been applied, such as Proper Orthogonal Decomposition (POD) method and so on. In numerical simulation investigation, both steady and unsteady computational methods have developed the mechanism of laminar separation bubbles. By using turbulence models with different transition criterions, the prediction of time-averaged flow in laminar separation is achieved. For unsteady simulation, Direct Numerical Simulation (DNS) and Large Eddy Simulation (LES) methods have very high turbulence resolution and the capability to capture the most real details of turbulence, but they still need a lot of computing resources, as well as a long calculation period, especially DNS method, which limits their application in the overall performance analysis of separation flow. Comparatively speaking, although the Unsteady Reynolds Average Navier-Stokes (URANS) method cannot obtain enough small vortices, it has advantages in engineering application because of the computing resources are far less than the two methods mentioned above.

The present thesis consists on a joint experimental and numerical investigation on a flat plate with adverse pressure gradient. The experiment provides detailed results including distribution of wall pressure coefficient and boundary layer velocity and turbulence profiles

for several values of typical influencing parameters on the behavior of the flow phenomena: Reynolds number, freestream turbulence intensity, turbulence length scale and end-wall opening angle, which determines the adverse pressure gradient intensity. The numerical work consists on carrying out a systematic analysis, both with Reynolds Average Navier-Stokes (RANS) and Unsteady Reynolds Average Navier-Stokes simulations. The results of the numerical simulations are critically investigated and compared with experimental ones in order to understand the effect of the main physical parameter on the LSB behavior. For RANS simulations, different turbulence and transition models are compared at first to identify the adaptability to the flow phenomena; then, the influence of the four aforementioned parameters on the LSB behavior, is investigated under a typical aggressive adverse pressure gradient. Boundary layer integral parameters are discussed for the different cases in order to understand the flow phenomena in terms of flow time-mean properties. For URANS simulations, the analysis focuses on the surveys of the instantaneous velocity vector maps which highlight the dynamics of the large-scale structures shed near the bubble maximum displacement. Several typical cases are simulated by URANS in order to further understand the spatial and temporal characteristics of laminar separation flow.

Chapter 2

Fundamentals of Boundary Layer Theory

The concept of viscosity was not introduced into early development of fluid dynamics by researchers. Until the end of 17th century, Newton put forward the concepts of Newtonian fluids and viscous which are ubiquitous in fluids. Also, with the help of Newton's contribution in differential calculus, many breakthroughs have been made in the field of idealized inviscid fluid dynamics by the following researchers, such as Bernoulli, Daramber and Euler as typical representatives. Among them, Euler developed the mathematical description based on infinitesimal fluid element, and deduced the governing equation of inviscid problem by combining the conservation of mass and Newton's second law. On the basis of ignoring the viscous effect, Euler completed the derivation of a series of nonlinear partial differential equations of fluids, which promotes the development and perfection of theoretical fluid dynamics. In the 19th century, after Euler et al., the next important theoretical progress is the addition of frictional drag term to Euler's inviscid equation and the introduction of viscous coefficient μ, which established the famous Navier-Stokes (N-S) equations. Despite the strong interest of mathematicians, up to now, only a few special solutions of N-S equations are given, but their general solutions cannot be obtained. Although it has been known that the great difference between the results of classical fluid dynamics and the reality in many cases is based on neglecting the viscous effect theoretically. However, due to the lack of an effective mathematical treatment method for the integral equation of motion of viscous flow, engineers also developed a practical-based hydrodynamics, that is hydraulics. Depending on a large number of experimental data, it is quite different from theoretical hydrodynamics in terms of methods and objectives. For a long time, theoretical and experimental fluid dynamics developed in their respective directions, with little in common.

Until 1904, Ludwig-Plandtl put forward the concept of boundary layer on the Third International Mathematics Congress in Heidelberg, by establishing a high degree of connection between theory and experiment, unimaginable success in the field of modern fluid dynamics was achieved, and clarified that the two divergent directions of fluid dynamics are possible to unify [29]. Through theoretical considerations and some simple experiments, Prandtl showed that the flow over an object can be divided into two regions: a very thin layer near the object (boundary layer) where the viscosity is important, while the other one is the remaining region outside the layer which its viscosity can be neglected. With the help of this concept, not only the importance of viscosity in the given resistance problem is explained convincingly physically, but also a path is set for the theoretical treatment of viscous flow by greatly reducing the difficulty of mathematics. It has been proved that the theory of Prandtl's boundary layer or frictional layer is very useful. Since the beginning of 20th century, it has played a considerable role in promoting the study of fluid dynamics. Driven by the development of flight technology, the theory developed rapidly, making airfoil theory and aerodynamics the cornerstone of modern hydrodynamics.

2.1 Boundary Layer Concept

In Prandtl's theory of boundary layer, it is believed that the effect of friction is to make the fluid near the wall adhere to the surface. On the other words, he assumes the non-slim

boundary condition near the wall, and the friction effects only inside the boundary layer, a very thin area. While for the outside of the boundary layer, the inviscid flow is basically considered, just like the investigations carried on two centuries ago. The concept of boundary layer is described in the Fig. 2.1. In such kind of flow that has connection to the aerodynamic object, the length scale of boundary layer is smaller in comparison with the object. Let's take a look at Prandtl's description with this photograph.

"A very satisfactory explanation of the physical process in the boundary layer between a fluid and solid body could be obtained by the hypothesis of an adhesion of the fluid to the walls, that is, by the hypothesis of a zero-relative velocity between fluid and wall. If the viscosity was very small and the fluid path along the wall not too long, the fluid velocity ought to resume its normal value at a very short distance from the wall. In the thin transition layer however, the sharp changes of velocity, even with small coefficient of friction, produce marked results"

One of the obvious results from Fig. 2.1 is that the velocity of an object immersed in a fluid varies sharply in a very short distance in the vertical direction of its surface. In other words, the boundary layer is a region with a maximum velocity gradient. According to Newton's law of shear stress, that is, the shear stress is directly proportional to the velocity gradient, thus the shear stress in the boundary layer is also very large. As a result, the surface friction force acting on an object cannot be neglected, which is contrary to what researchers believed at the beginning of the 19th century. For the two regions of flow, the external inviscid flow can strongly affect the characteristics of the internal boundary layer; in fact, the external flow determines the boundary conditions on the outer edge of the boundary layer and the velocity distribution within the boundary layer. On the other hand, the thickness of the boundary layer is so thin that there is no visible effect on the external inviscid flow. This rule is invalid only when the flow separation exists. At this time, the external inviscid flow will be greatly affected by the presence of the flow separation region. Prandtl describes it as follows:

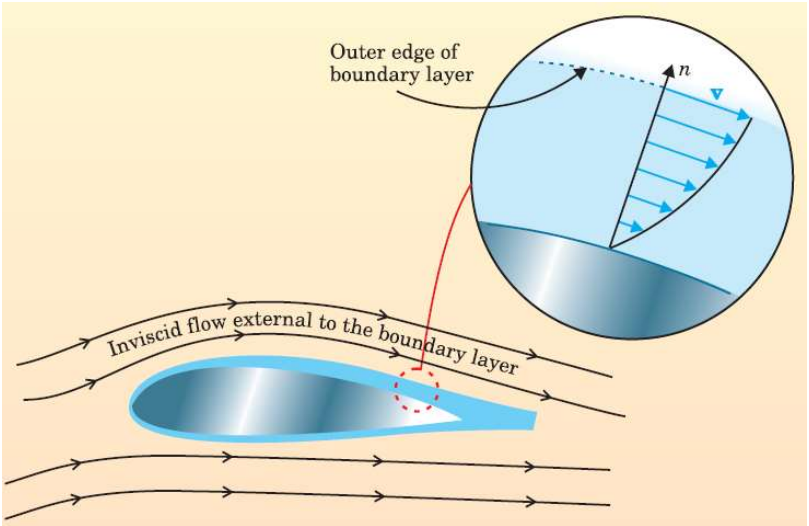

Fig. 2.1 – Boundary layer around airfoil

"While dealing with a flow, the latter divides into two parts interacting on each other; on one side we have the "free fluid", in which is dealt with as if it were friction-less, according to the Helmoholtz vortex theorems, and on the other side the transition layers

near the solid walls. The motion of these layers is regulated by the free fluid, but they for their part give to the free motion its characteristic feature by the emission of the vortex sheets."

The concept of Prandtl boundary layer makes it possible to calculate aerodynamic drag quantitatively. Because of the inability to solve the N-S equations, engineers at the beginning of the 20th century were unable to correctly predict the shear stresses attached to solid surfaces in fluids. Although it is known that the force acting on the airfoil is actually the result of the pressure and shear stress distribution, the pressure distribution on the airfoil can also be calculated by referring to the inviscid theory, but the shear stress is the result of the viscous force, therefore, in this case, the N-S equations must be considered. Prandtl also points out that for the boundary layer, the N-S equations can be reduced to a simplified form and applied only in the boundary layer. The results, called boundary layer equations, are similar to the N-S equations corresponding to each coupled system. They are all nonlinear partial differential equations and can be analyzed and solved in some basic flow configurations (e.g. Blasius solutions of flat plates).

The main breakthrough of the boundary layer theory in mathematics is that the boundary layer equations show a completely different mathematical behavior from the N-S equations. The N-S equations are elliptical, which means that the whole flow field needs to be solved simultaneously to meet the specific boundary conditions defined along the whole flow boundary. On the contrary, the boundary layer equations have a parabolic mathematical behavior, which provides tremendous analytical power and computational simplification. They can be gradually solved by moving downstream from the direction where the flow meets the object, under specific inflow conditions and specified boundary conditions at the outer edge of the boundary layer. The calculation of the system provides the variables of the boundary layer flow field, including the velocity gradient at the wall. The shear stress at the wall also means that the surface friction resistance can be obtained directly through these velocity gradients.

This step-by-step method for solving boundary layer flows began several years after Prandtl's 1904 report and was mainly completed by his students at the University of Gottingen. Among these solutions, it is possible to accurately predict the surface friction resistance of objects in some cases, as well as the location of flow separation points, and the corresponding shape resistance and pressure resistance. In a brief paper in 1905, Prandtl gave the boundary layer equation in two-dimensional steady flow field, and proposed solutions to these equations. The frictional resistance of the plate was calculated roughly, and the boundary layer separation under the circumstance of counter-pressure gradient was discussed. These are pioneer contributions.

In 1908, Heinrich Blasius, a student of Prandtl, published a paper on boundary layer in small frictional fluids in a well-known journal. The boundary layer flow of two-dimensional plates and cylinders were discussed, and the solutions of these two problems were given. For a plate, he obtained a more accurate solution of surface friction than that in Prandtl's paper. For the flow around a circular cylinder, he gave the solution of the separation point on the back of the cylinder. As previously described, although the boundary layer equations are simpler than the N-S equations, they are still coupled, non-linear partial differential equations. However, in a particular type of pressure gradient flow, they can be reduced to an ordinary differential equation. For example, for the flow direction parallel to the plate, it can be considered that the pressure remains unchanged, i.e. the zero angle of attack condition. This is the Blasius equation that we are familiar with today.

Despite the important work done by Blasius and the subsequent publication of several theoretical articles on boundary layer by the Prandtl Research Group, aerodynamics has not attracted enough attention, especially outside Germany. Later in 1921, Theodore von Carmen, an early student of Prandtl and a professor at Aachen University, obtained a momentum integral equation by simply integrating the boundary layer equations. This equation has been proved to be applicable to a large number of engineering problems. As a result, the boundary layer theory has received more attention and has been accepted by the Scientific Committee.

In the mid-1920s, the research on boundary layer theory grew exponentially, focusing mainly on advanced, extended and applied aspects. These works brought a boom period for fluid mechanics and aerodynamics. An important industrial application of boundary layer theory appeared at the end of 1920. Designers began to apply this theory to predict frictional resistance of spacecraft and aircraft surfaces. Until then, they had to use only empirical data obtained mainly from aerodynamic experiments. These data are usually the total resistance, and it is difficult to eliminate the friction effect. Later, it was well known that wind tunnel data were inaccurate, and conservative designers were reluctant to put their designs on it. But since the late 1920s, when the precise data obtained from the boundary layer theory and the surface friction equation began to be more widely accepted, the results of the boundary layer theory began to become the standard tool used by aircraft designers.

2.2 Boundary Layer on a Flat Plate at Zero Incidence

After Prandtl proposed the concept of boundary layer, many works have been completed by researchers to improve this theory. An idealized model is the flat plate boundary layer at zero angle of attack [30]. Fig. 2.2 illustrates the boundary layer of a flat plate in an incompressible two-dimensional flow environment. Here, the horizontal plate is parallel to the inflow direction, i.e. the inflow angle is 0. When the uniform incoming flow contacts the front edge of the plate, the velocity distribution on the plate surface begins to change. It can be seen that there exists a very thin boundary layer in the area adjacent to the surface of the plate, and its internal velocity is much lower than that corresponding to the location where there is a certain distance from the wall. This is because both friction and molecular diffusion between adjacent regions can transfer shear stress, increase the fluid velocity near the wall, and slow down the fluid velocity in faster regions. As the distance from the leading edge is becoming longer, the fluid layer with reduced friction becomes larger as more and more fluid mass are captured by deceleration. Therefore, the thickness of the boundary layer δ (x) is a monotonic increasing function of x. However, it must be clearly pointed out that the concept of boundary layer thickness δ is introduced artificially. The transition from boundary laminar flow to external flow, at least in the case of laminar flow, occurs continuously, hence, the precise boundary cannot be given in principle. Because the concept of boundary layer thickness is very vivid, it is often used in practice. Normally, the boundary is arbitrarily given, i.e. the point at which the velocity reaches a certain percentage of the external velocity, e.g. 99%. For clarity, the commonly used definition is delta δ_{99}. Another obvious feature is along the progressive flow, the boundary layer of a flat plate is also divided into laminar, turbulent and intermediate transition zones. The variation of boundary layer thickness is also different under varied flow conditions. The subsequent analysis will make it clear that the boundary layer in the turbulent region develops faster than the laminar boundary layer. The boundary layer transition is developed on the basis of Reynolds' theory of laminar instability, which has been proved for many years. The influence of other parameters on the transition section (pressure gradient, suction, Mach number, heat transfer) is clarified by using the

boundary layer stability theory. This theory has been applied to very low drag airfoils (laminar airfoils).

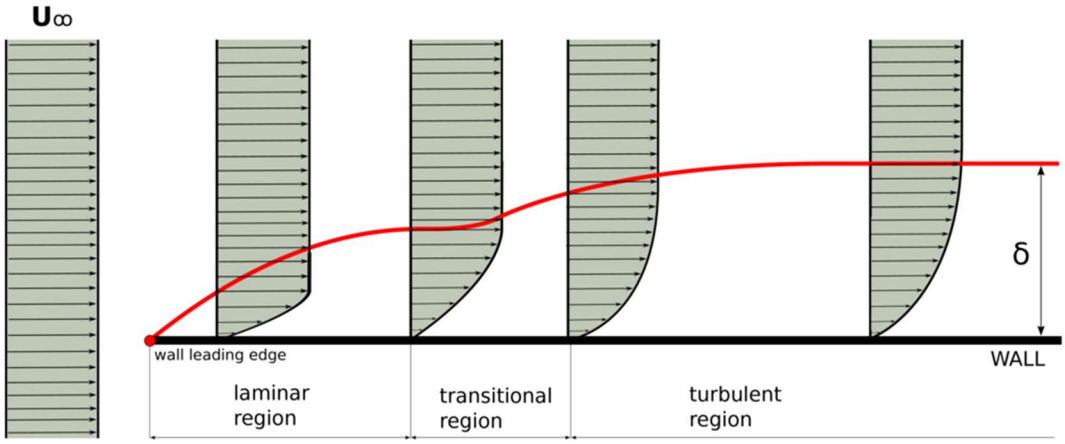

Fig. 2.2 – Boundary layer on flat plate with 0 incidence

2.2.1 Laminar flow

For laminar boundary layer at zero angle of attack, Blasius [31] took the lead in giving the solution under two-dimensional incompressible conditions, and gave both the expressions of boundary layer thickness and surface friction coefficient. In laminar flow, inertial force and friction force are balanced. According to dimensional analysis, the inertial force has the dimension of $\rho u_\infty^2/x$, while the friction force has the dimension of $\mu u_\infty/\delta^2$, therefore

$$\frac{\rho u_\infty^2}{x} \sim \mu u_\infty/\delta^2$$

While the thickness of boundary layer should be

$$\delta \sim \sqrt{\frac{\mu x}{\rho U_\infty}} = \sqrt{\frac{\nu x}{U_\infty}} \tag{2.1}$$

Blasius gave the exact solution in 1908 for the unknown proportion coefficient in the relation. Ultimately, the expression is

$$\delta_{99}(x) = 5\sqrt{\frac{\nu x}{U_\infty}} \tag{2.2}$$

The thickness of boundary layer can be obtained by dimensionless plate length.

$$\frac{\delta_{99}(x)}{l} = \frac{5}{\sqrt{R_e}}\sqrt{\frac{x}{l}} \tag{2.3}$$

Here, the Reynolds number corresponds to the total length of the plate. It can be seen from the equation that the thickness of laminar boundary layer decreases with the increase of Reynolds number. Therefore, when the Reynolds number tends to infinity, the boundary layer will disappear. At the same time, it is also known from the equation that the thickness

of the boundary layer increases with the increase of the distance and is proportional to the power of 1/2 of x.

As previously described, the thickness of the boundary layer is arbitrarily specified. Usually, a meaningful and measurable boundary layer thickness in hydrodynamics is displacement thickness δ_1, defined as

$$U\delta_1(x) = \int_{y=0}^{\infty} (U-u)dy \tag{2.4}$$

Where U is the velocity value on the outer boundary layer corresponding to position x. As shown in Fig. 2.3, the area of the two shadows must be equal. The displacement thickness can tell us the extent to which the external mainstream migrates outward due to the existence of boundary layer. For the laminar flow of a flat plate with zero angle of attack, the displacement thickness given by Blasius is

$$\frac{\delta_1(x)}{l} = \frac{1.721}{\sqrt{R_e}}\sqrt{\frac{x}{l}} \tag{2.5}$$

By comparison, the displacement thickness is about 1/3 of the nominal thickness.

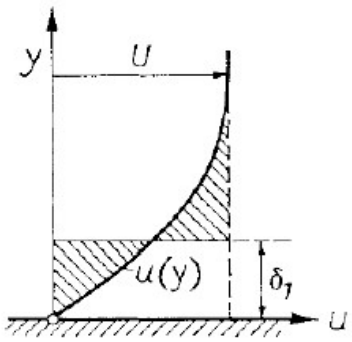

Fig. 2.3 – Displacement thickness

Friction prediction. Similar to the thickness of the boundary layer, the wall shear stress and the overall friction resistance of the plate can be predicted. According to Newton's law of friction, there are equation (2.6). Subscript *w* denotes the value at the wall. According to the dimensional theory, then equation (2.7) can be obtained.

$$\tau_w(x) = \mu\left(\frac{\partial u}{\partial y}\right)_w \tag{2.6}$$

$$\tau_w(x) = \mu U_\infty \sqrt{\frac{\rho U_\infty}{\mu x}} = \sqrt{\frac{\mu\rho U_\infty^3}{x}} \tag{2.7}$$

From this we can know that the wall shear stress is proportional to the 3/2 power of velocity, and it is worth noting that it is proportional to the -1/2 power of x. This shows that the wall shear stress is not unchanged on the plate, but decreases with the increase of x. The shear stress near the leading edge of the plate is particularly large. According to the relationship, the wall shear stress is inversely proportional to the thickness of the boundary layer, for example, the thin boundary layer corresponds to larger shear stress. The proportional

constants in equation (2.7) can be determined again from the exact solution. After deduction, the surface friction coefficient corresponding to the laminar flow state is equation (2.8).

$$C_f = \frac{\tau_w(x)}{\frac{1}{2}\rho U_\infty^2} = \frac{0.664}{\sqrt{R_e}}\sqrt{\frac{x}{l}} \tag{2.8}$$

According to the coefficient of friction, the resistance of plate can be obtained by integrating the whole plate, and then the resistance coefficient can be obtained. In this case, the drag coefficient of a flat plate with an area of S=b×l is 2.10. When the Reynolds number is greater than power of 10^4, the measured results are very close to the theoretical values. According to the formula, the drag coefficient is also a function of Reynolds number.

$$C_D = \frac{D}{\frac{1}{2}\rho U_\infty^2 lb} = \frac{1.328}{\sqrt{R_e}} \tag{2.9}$$

2.2.2 Turbulent flow

As mentioned earlier, the laminar flow regime is not always maintained in the flat boundary layer. When the flow moves downstream, the Reynolds number will reach a level sufficient to trigger a transition, thus generating a turbulent boundary layer. The leading edge near the plate is laminar flow, and the turbulence develops downstream after the critical point, and the position of the critical point depends on the critical Reynolds number. Although the transition from laminar flow to turbulence is a limited region, it still can be represented by a point, and it is often assumed that the transition is instantaneous. The value of critical Re depends largely on the degree to which the external flow is undisturbed. The transition process will be discussed in detail in Section 2.6. With the failure of Blasius solution, other semi-empirical modified formulas are proposed, such as equation (2.10) and equation (2.11).

$$\delta_{turb} = \frac{0.37x}{R_{e_x}^{\frac{1}{2}}} \tag{2.10}$$

$$C_{fturb} = \frac{0.027}{R_{e_x}^{\frac{1}{7}}} \tag{2.11}$$

The formula shows that the thickness of turbulent boundary layer varies by 4/5 power of the leading-edge distance and has a faster rate than that of laminar flow. The surface friction coefficient is proportional to the Reynolds number -1/7 power and has a larger friction coefficient. This faster growth rate is mainly based on the greater mixing effect of near-wall basin fluids.

2.2.3 Viscous sublayer

In laminar flow, the boundary layer is a region affected by viscous, but not in turbulent boundary layer. The whole flow region is divided into two regions, one is the external flow region without turbulence (or at least without turbulence characteristics), the other is the turbulence region within the boundary layer, which is characterized by random fluctuating motions. The turbulent boundary layer is also called the friction layer because of the obvious friction resistance. In the turbulent frictional layer, the viscous effect is confined to a thin

layer which is much thinner than the boundary layer near the wall. It is called the viscous bottom layer or the viscous sublayer, hence the turbulent boundary has two layers. The larger part is a friction layer, which is mainly due to the obvious friction caused by turbulent fluctuations and is not affected by viscosity. In the very thin bottom zone, the effect of viscous force causes real friction. Although the transition between the two layers is continuous, the concept of viscous bottom thickness is also used in practice. This thickness increases very slowly as x moves away from the leading edge. Dimensionless viscous sublayer thickness with total boundary layer thickness is also used in some empirical formulas, such as equation (2.12)

$$\frac{\delta_v}{\delta} = 680\frac{ln^2 Re_x}{Re_x} \tag{2.12}$$

With the increase of local Reynolds number Re_x, the viscous sublayer of the total friction layer becomes smaller and smaller.

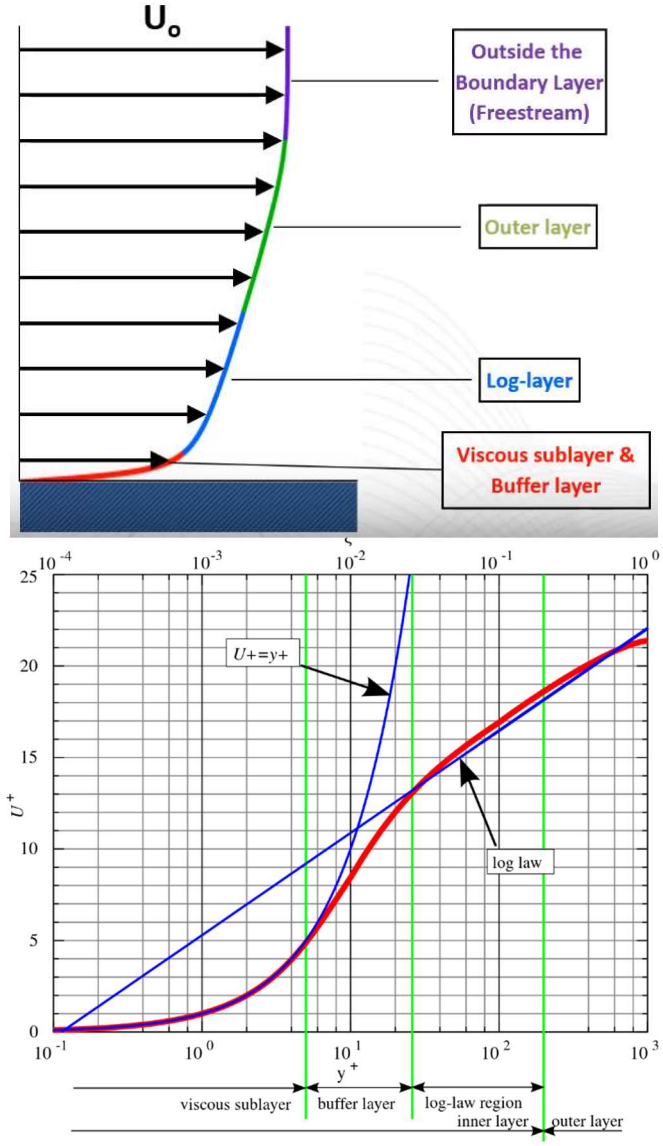

Fig. 2.4 – Viscous sublayer (y+<5), Buffer layer (5<y+<30) and Fully turbulent or Log-low region (y+>30).

Two dimensionless parameters are used to describe the turbulent boundary layer: the distance y+ in the viscous unit and the dimensionless velocity u+, their relationship is plotted in Fig. 2.4. Because of the viscous effect, the viscous sublayer exists in the region of y+<5, i.e., the laminar flow state is maintained. y+>30 corresponds to logarithmic region, which flow is turbulent and has strong velocity fluctuation, including density and direction. For this reason, the shape of turbulent boundary layer is thicker than that of laminar boundary layer near the wall. The region between them is defined as a buffer zone, whose physical parameters are gradient changed from one state to another. The concept of viscous sublayer is very important in numerical simulation. It will be introduced in detail in the following chapters.

2.3 Boundary Layer on an Airfoil

The zero-attack-angle plate boundary layer described above is an ideal model, because the outer flow is inviscid and the solution obtained is based on the steady pressure in the whole flow range. In fact, the flow through an arbitrary shape will cause additional pressure. Fig. 2.5 depicts the boundary layer around the airfoil surface. For clear reasons, the transverse dimension is greatly increased. Similar to plate flow, the laminar boundary layer first appears at the leading edge of the airfoil. When the surface profile exceeds the critical position, laminar-turbulent transition occurs, and the flow develops into turbulence after the critical position. Because of the change of airfoil, there is a distribution of pressure rise outside the boundary layer flow.

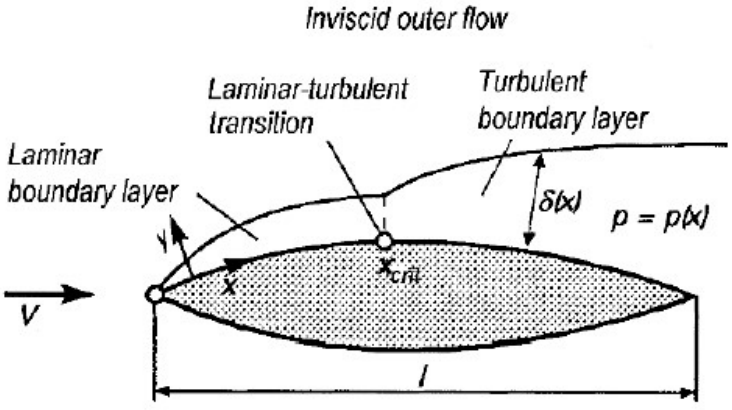

Fig. 2.5 – Development of the boundary layer around airfoil

This pressure distribution forces the pressure at any position x on the boundary layer, and the pressure perpendicular to the wall remains unchanged. Therefore, the pressure distribution on the outer boundary is consistent with that on the wall. Any difference between these two pressure distributions can only be caused by streamline curvature and pressure gradient perpendicular to the mainstream to compensate for centrifugal force. Because the boundary layer is very thin compared with the curvature radius of the contour at high Reynolds number, the pressure gradient perpendicular to the wall will not appear. The pressure on the boundary layer is confined to the outer mainstream and is only a function of x. In addition, the correlation mentioned in the case of plate boundary layer is also valid: as the boundary layer develops along the contour of the object, the thickness of the boundary

layer δ（x）usually increases and the wall shear stress τ_w decreases. In the case of turbulent boundary layer, the thickness of downstream boundary layer increases more than that of laminar flow. With the increase of Reynolds number formed by the free flow velocity V and the characteristic L, length of body, the thickness of boundary layer decreases to zero in the limit case. The pressure distribution exerted by outflow plays an important role in the formation of boundary layer. For example, the location of laminar-turbulent transition depends largely on it. If the pressure in the flow direction increases substantially, the boundary layer may be separated from the wall if it may occur in the area facing the back of the wing or on the back of the blunt body. This extremely important phenomenon of boundary layer separation will be discussed in more detail in the next section.

2.4 Boundary Layer Separation

Another important conclusion proposed by Prandtl is the separation of flow, which occurs when the flow is in a strong adverse pressure gradient condition. In the case shown in Fig. 2.6, Prandtl points out that the boundary layer separates from the surface and extends downstream. A separated flow with low flow energy will form a wake region behind the object, which is essentially a dead zone with low pressure characteristics. The strength of pressure loss depends on the size of the bubbles formed. Prandtl's original text is described as follows:

"In given cases in certain points fully determined by external conditions, the fluid flow ought to separate from the wall. That is, there ought to be a layer fluid which, having been set in rotation by the friction on the wall, insinuates itself into the free fluid, transforming completely the motion of the latter, and therefore playing there the same part as the Helmholtz surfaces of discontinuity."

Prandtl believes that at the separation point, a large part of kinetic energy of the fluid mass in the deep boundary layer dissipates due to friction, which does not provide enough energy for the fluid to enter the area of pressure increasing, and then the velocity distribution near the wall is exhausted. At the separation point, there is a transition progress, and after the separation point, the boundary layer will simply lift off the surface. The description of boundary layer separation can also be referred in Fig. 2.7. As a result of the backflow near the wall, the thickness of the boundary layer is obviously thicker and the mass in the boundary layer flows into the outer layer. At the separation point, the streamline leaves the wall at a particular angle. The specific location of separation is determined by the velocity gradient condition perpendicular to the wall direction, for example, the wall shear stress disappears to 0. The location of the separation point can only be determined by accurate calculation (integral of boundary layer differential equation).

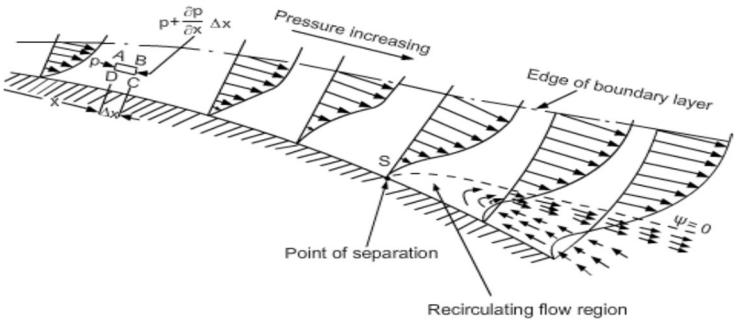

Fig. 2.6 – Flow in boundary layer before and after the point of separation

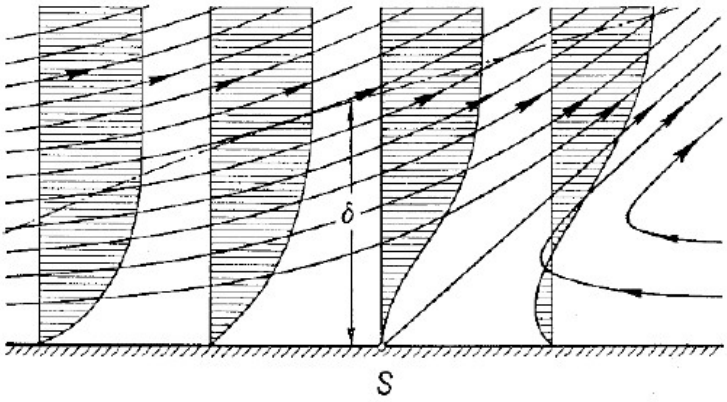

Fig. 2.7 – Boundary layer close to separation point

Generally speaking, the greater increase in the adverse pressure gradient region, the greater risk of separation, especially in the rear zone of the blunt body. This explains why the pressure distribution of the slender airfoil is so consistent with the theoretical inviscid flow. The reason is that the pressure rise behind the slender airfoil is not obvious, so the boundary layer will not separate. As a result, the overall resistance is mainly composed of frictional resistance, while the shape resistance is very small. Once the separation of flow occurs, the pressure component on the surface of the object will change fundamentally. The change of pressure distribution caused by flow separation produces obvious flow resistance, that is, a large unbalanced force acts in the direction of free flow - the direction of resistance. When the separation range is enlarged, the pressure resistance will usually be much greater than the surface friction resistance. The type of external inviscid flow that promotes boundary layer separation is the flow that produces an adverse pressure gradient, i.e. the pressure increases along the flow direction. In this regard, Prandtl's explanation is as follows:

"On an increase of pressure, while the free fluid transforms part of its kinetic energy into potential energy, the transition layers instead, having lost a part of their kinetic energy (due to friction), have no longer a sufficient quantity to enable them to enter a field of higher pressure, and therefore turn aside from it."

Because of the vortices generated by the boundary layer rolling up, the appearance of boundary layer separation will also lead to high loss, which is the reason for the high shear stress. As Prandtl described, the external conditions produced by free-stream affect the development of the boundary layer, while the viscous effect is confined to the thin layer near the wall. Outside this region, the viscous effect can be ignored. Therefore, under the condition of large separation, due to the separation of viscous layer from wall, viscous layer can sensitively change the potential flow around it (i.e., viscous non-viscous interaction). Therefore, the occurrence of boundary layer separation changes the pressure distribution around the body immersed in the flow (such as wing airfoil or blade profile), that is, the load distribution.

Under certain conditions, the transition behind the laminar separation zone is completed in a short distance, i.e. to turbulent state, then the boundary layer will appear the behavior of reattachment. At this point, the laminar separation zone is confined to a range close to the wall and travels in a relatively closed shape, that is, the laminar separation bubble described in Section 1.1 and Fig. 2.8. It can be seen that the boundary layer theory is the basis for the study of laminar separation bubbles, or that the study of laminar separation bubble is an extension of the boundary layer theory.

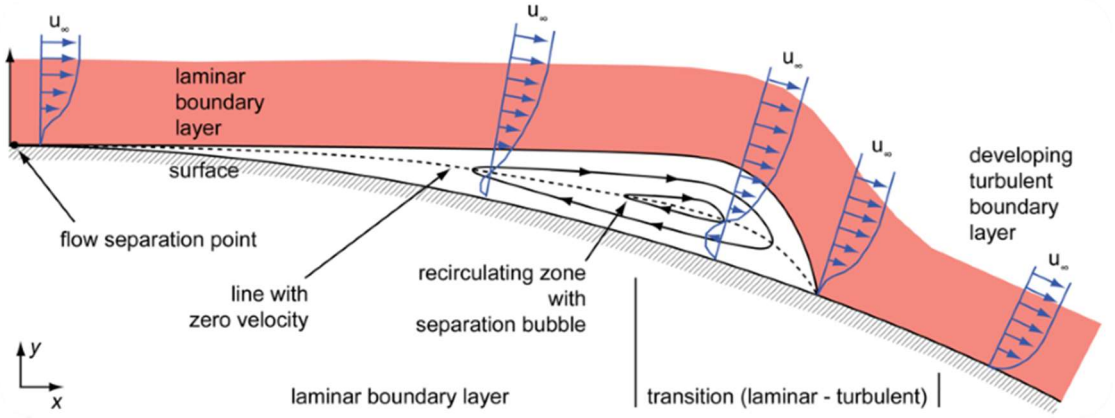

Fig. 2.8 – Laminar separation bubble structure

2.5 Boundary Layer Integral Parameters

It is very useful to introduce the integral parameters in the analysis of boundary layer flow with transition and separation. These parameters simplify the flow in the whole boundary layer into a function only related to the flow direction x. In order to achieve this goal, it is usually not necessary to know the detailed information that only affects the solution of the minimum flow-field in the boundary layer, but to know the integral parameters associated with the total loss.

Although the nominal thickness of the boundary layer is introduced earlier, this concept is not suitable for specific quantitative calculation, and its engineering application value is limited. Therefore, people defined the relevant thickness concept, such as following.

The first integral parameter is the displacement thickness of the boundary layer, δ*, which is related to the loss of flow mass due to the existence of the boundary layer, as shown in Fig. 2.9.

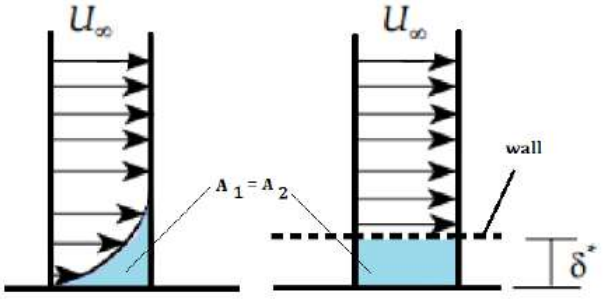

Fig. 2.9 – Boundary layer displacement thickness scheme

The flowrate of downstream can be calculated as an integral of the area defined by the velocity profile and the *y* axis. Considering a two-dimensional channel flow with a unit width, the volume flowrate should be:

$$Q = \int_0^\infty u(y)dy \tag{2.13}$$

To define δ*, the velocity distribution characteristics of the same flowrate Q are cited on the right side of Fig. 2.9. This typical velocity distribution considers no viscous effect; hence the velocity is uniform in the vertical direction. In order to make the two mass flows equal, the bottom area of the two velocity distributions must be equal. This equivalent velocity

distribution offsets an equivalent thickness of δ* on the wall at its initial position, and the velocity in this thickness is 0. The loss of flow is the same for the two velocity distributions, which can be expressed as

$$\delta^* U_\infty = \int_0^\infty [U - u(y)]dy \tag{2.14}$$

Therefore, the result of displacement thickness can be expressed as

$$\delta^* = \int_0^\infty \left[1 - \frac{u(y)}{U_\infty}\right] dy \tag{2.15}$$

According to equation (2.15), the displacement thickness represents the increase of the volume thickness required to generate a non-viscous virtual flow with the same flowrate as the actual viscous flow. In other words, it represents the degree of outward deflection of streamlines caused by the viscous effect on the plate. One application of this conclusion is to simplify the calculation of aerodynamics involving boundary layer flows. In order to simulate the effect of boundary layer flow, the thickness of the object can be increased to the size equivalent to the displacement thickness, and then the turbulence problem is solved according to the inviscid fluid.

Another integral parameter that must be used in boundary layer analysis is the momentum thickness, θ. The definition of its physical meaning is similar to that of displacement thickness of a boundary layer. According to Fig. 2.9, the reduction of the momentum in x direction related to the mass flow in a boundary layer could be expressed as

$$M_{loss,BL} = \int_0^\infty \rho u[U - u(y)]dy \tag{2.16}$$

Compare to the case of velocity loss in the boundary layer, the momentum of the flow also decreases according to the ideal flow. Consider a uniform velocity distribution, the momentum loss caused by displacement can be expressed as

$$M_{loss,displacement} = \rho U_\infty^2 \theta \tag{2.17}$$

Certainly, the two momentum losses should be equal, hence there must be

$$\rho U_\infty^2 \theta = \int_0^\infty \rho u[U - u(y)]dy \tag{2.18}$$

Then, the expression of momentum loss thickness can be deduced as follows.

$$\theta = \int_0^\infty \frac{u(y)}{U_\infty}\left[1 - \frac{u(y)}{U_\infty}\right] dy \tag{2.19}$$

The momentum displacement thickness gives the boundary layer loss directly related to the momentum loss. It can be proved that θ at the given station x=x_1 is proportional to the comprehensive friction coefficient from leading edge, x=0, to the considering position.

$$\theta \propto \frac{1}{x_1}\int_0^{x_1} c_f \, dx = C_f \tag{2.20}$$

Here, c_f is the local surface friction coefficient, while C_f is the average friction coefficient in the length of the surface from x = 0 to x=x_1. Therefore, the concept of momentum thickness is very useful for predicting the coefficient of friction.

In addition, according to the two dimensions mentioned above, a dimensionless parameter, shape factor H_{12}, can be introduced. It is defined as the ratio of displacement thickness to momentum thickness.

$$H_{12} = \frac{\delta^*}{\theta} \tag{2.21}$$

The value of shape factor is very useful for determining the flow state, because this parameter has distinct values in the two discrepant flow states. For incompressible pressure-free gradient flow on a flat plate, the values are as follows respectively

$H_{12} = 2.554$ in case of a laminar boundary layer;

The value decreases to $H_{12} = 1.43$ when the boundary layer is turbulence.

In fact, although these two solutions are only applicable to the above cases, the values of H_{12} are consistent with the same trend when the fluid is sensitive to the effects of pressure gradient and other disturbance factors.

The Von Karman integral equation can be deduced by further considering the integral parameters. Considering the momentum equation of the control volume is shown in Fig. 2.10, including the length *dx* of the boundary layer, the equilibrium of momentum flux M can be written as following:

$$\sum F_{ext} = \sum M_{out} - \sum M_{in} \tag{2.22}$$

After some simplification, it could be obtained that

$$-\delta \frac{dp}{dx} dx - \tau_w dx = \frac{d}{dx}\left[\int_A^B \rho u^2 dy\right] dx - U_e \frac{d}{dx}\left[\int_A^B \rho u dy\right] dx \tag{2.23}$$

The equation can now be rearranged to introduce boundary layer integral parameters:

$$\tau_w = \frac{d}{dx}\left[\rho U_e^2 \int_A^B \frac{u}{U_e}\left(1 - \frac{u}{U_e}\right) dy\right] + \frac{dU_e}{dx} \int_A^B \rho U_e \left(1 - \frac{u}{U_e}\right) dy \tag{2.24}$$

Reviewing the definitions of both δ* and θ, also introducing friction coefficient C_f

$$C_f = \frac{\tau_w}{\frac{1}{2}\rho U_e^2} \tag{2.25}$$

Von Karman equation can be obtained.

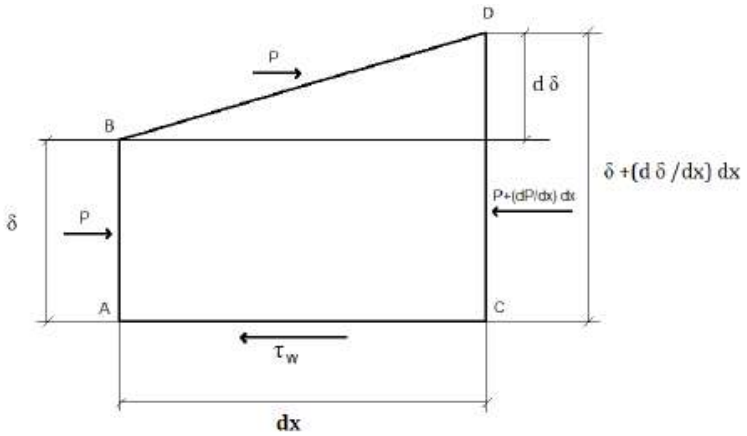

Fig. 2.10 – Sketch of control volume of Von Karman Equation

$$\frac{C_f}{2} = \frac{d\theta}{dx} + \frac{\theta}{U_e}\frac{dU_e}{dx}(2 + H_{12}) \tag{2.26}$$

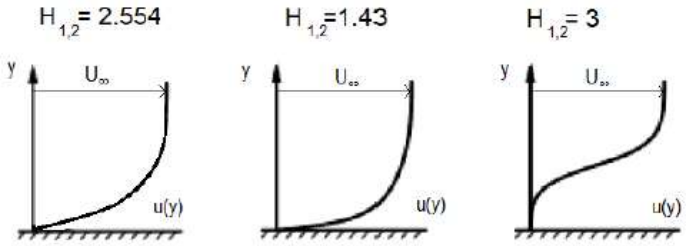

Fig. 2.11 – Boundary layer profile for a laminar (left) turbulent (middle) and separation (right) with the related H_{12} value

From equation (2.26), the strong dependence of velocity variation and pressure gradient on the increase of momentum thickness can be determined. It is also noted that in the definition of displacement thickness, 1-u/U_e is always greater than u/U_e(1-u/U_e), then H_{12} is always greater than 1. For the attached flow, the upper limit of shape factor is 3, and the typical value of initial separation is shown in Fig. 2.11, compared with both turbulence and laminar boundary layer.

Recalling the Blasius solution introduced in Section 2.1, similar to δ_{99} and C_f, for laminar boundary layer, the relation of integral parameters can be derived.

$$\theta = \frac{C_f}{2} = \frac{0.664x}{\sqrt{Re_x}} \tag{2.27}$$

θ and friction coefficient are inversely proportional to the square root of Reynolds number and to $x^{1/2}$. For displacement thickness, it is found that:

$$\delta^* = \frac{1.721x}{\sqrt{Re_x}} \tag{2.28}$$

This shows that the momentum displacement thickness has the same trend, but the linear coefficient is higher, which makes the momentum displacement enlarge with the increasing of the slope.

2.6 Transition Mechanisms

In many conditions, the real flow is essentially different from the laminar flow treated in the previous chapter. Their characteristics are belonged to turbulent flow. When the Reynolds number increases, both the typical internal flow in a pipe or in a channel and the process of the external boundary layer passing through an object surface belong to the transition from laminar flow to turbulent model. This transformation is referred to as the transition of laminar flow to turbulence, or the emergence of turbulence. It is a very important and fundamental problem for fluid mechanics.

In this case, the overall characteristics of the flow, especially the forces acting on the surface, are closely related to whether the boundary layer flow is laminar or turbulent. The transition progress of boundary layer flow on a solid surface is affected by many parameters, among which the most important are Reynolds number, external pressure distribution, solid wall itself (such as roughness) and disturbance of external freestream, i.e. turbulence intensity.

As the velocity distribution reforms in the transition region, the shape factor will decrease significantly. For the plate boundary layer, it decreases from 2.59 in the laminar region to 1.4 in the turbulent region, just as shown in Fig.2.12.

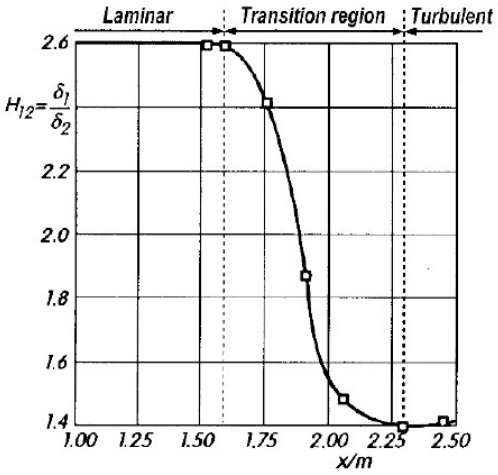

Fig. 2.12 – Shape factor variation for the plate boundary layer near the transition

In the process of transition, the resistance of flow changes obviously. In the boundary layer, the pressure gradient along the surface has a significant effect on both the region and the exact position of a transition. In areas where pressure decreases (in accelerated flow), the boundary layer usually remains laminar. However, even a slight increase in pressure could usually cause the onset of the transition. For an object with slender shape (airfoil, streamline body), the friction resistance can be greatly reduced by choosing the appropriate shape, and then the transition point can be moved downstream as far as possible. This is achieved by moving the widest position of the airfoil backwards. This kind of airfoil can maintain laminar flow state in a long distance; hence it is also called laminar airfoil. Its friction resistance is usually half of that of ordinary airfoil.

For the boundary layer around a blunt body, when the Reynolds number is greater than the critical one, the drag coefficient will decrease significantly. This large reduction is first found in the flow around a sphere, accompanied by a series of boundary layer transitions. When the boundary layer is turbulent, the separation point is greatly moved back, and the subsequent wake region will be limited to a fairly narrow range.

When transition occurs, the flow behavior transits from orderly parallel flow to chaotic one, accompany with the generation of turbulent spots, the cushioning function of the fluid viscosity is no longer effective. At this moment, turbulent spots can be observed in the boundary layer, which is independent with the mechanism described before. Turbulence spots begin to propagate downstream at the transition position. With their developments, the flow will thoroughly transfer into turbulent one [11], as shown in the Fig. 2.13.

A static method for determining the position of transition occurrence is the intermittent parameter γ and the turbulence point occurrence rate N, which represents the rate of turbulence spot occurrence per unit distance in the spreading direction, as described by Narashima [32]. Intermittence factor is not related to the mechanism of transition, but it is defined as the fraction of time flowing through a point on the turbulent surface:

$$\gamma(x) = 1 - exp\left[\frac{N\sigma}{u}(x - x_t)^2\right] \tag{2.29}$$

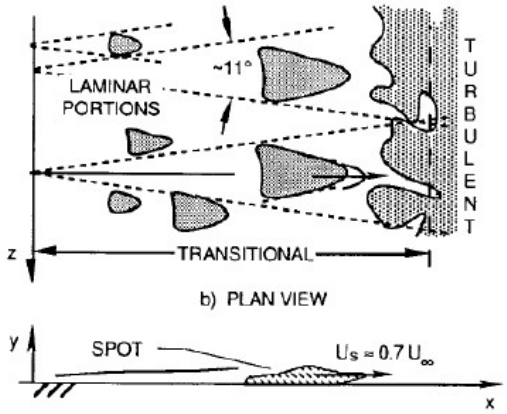

Fig. 2.13 – Turbulent spots propagation and growth in a transitional boundary layer

Among them, *u* is the velocity of freestream, while σ is the dimensionless Emmons turbulent spot propagation parameter related to the shape and velocity of turbulent spot. When γ=0, the flow is in a complete laminar state, while when γ=1, the flow is in a complete turbulent state.

In the progress of modelling a boundary layer flow from laminar to turbulent in turbomachinery with RANS equations, four distinct transition mechanisms can be recognized, they are Natural Transition, Bypass Transition, Separation Transition and Wake induced Transition, respectively.

Natural Transition: takes place when the turbulence intensity of a laminar boundary layer is relatively low, with a first component of the instability phase, known as Tollmien-Schlichting (T-S) waves, grow linearly in time and space.

Bypass transition: Occur when turbulence or other flow disturbances level are high, T-S waves also play a dominant role.

Separation Transition: When laminar boundary layer separation occurs, it is usually based on a strong adverse pressure gradient and driven by the specific linear inviscid mechanism of K-H instability mentioned in the literature.

Wake induced Transition: Usually, it can occur in the blade environment of turbomachinery, which is caused by wake disturbance caused by upstream cascade. Therefore, it has periodicity and is a forced unsteady transition process.

2.6.1 Natural transition

Natural transition occurs in a statically stable time-averaged flow field, i.e. in the boundary layer of attached flow with low turbulence intensity. T-S type unstable waves mark the beginning of transition: T-S waves are flow-directional and two-dimensional unstable waves associated with viscous flow begin to occur when the disturbance interacts with the boundary layer. The steady laminar flow gradually enlarges its modulus with the advancing of the flow until it increases sufficiently to cause a non-linear geostrophic transition into turbulence. Following this phenomenon, three-dimensional instability will occur, which will lead to the formation of an extended periodic vortex (with a specific production rate) in the far downstream, leading to the breaking of the laminar boundary layer and the generation of turbulence spots. Turbulence spots occur in a narrow spatial band. The final convergence of these spots will lead to the formation of turbulent boundary layer. Fig. 2.14 depicts the above process. Natural transition is a relatively slow process and requires a sufficient length in the direction of flow: it usually occurs in external flows and has very low freestream turbulence

intensity. It is a process susceptible to various disturbances, which the influence factors are including both turbulence intensity and pressure gradient.

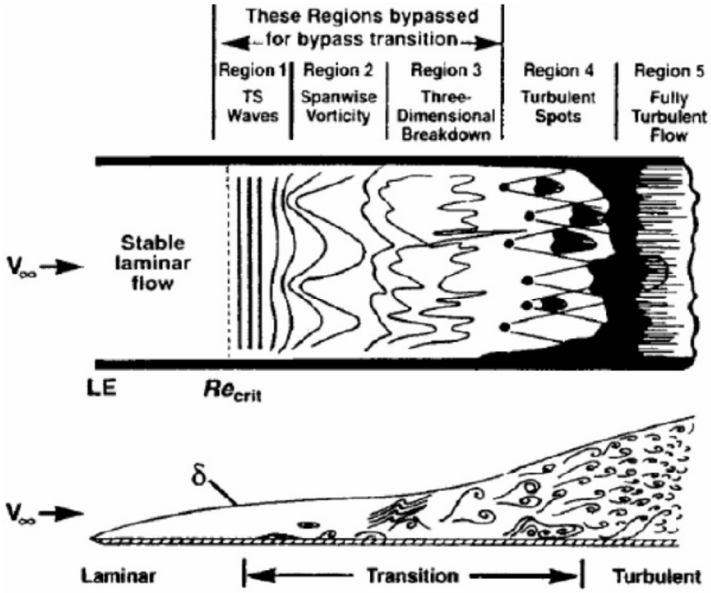

Fig. 2.14 – Mechanisms involved in the natural transition and bypass transition processes

2.6.2 Bypass transition

Bypass transition occurs at a sufficient high turbulence level, usually above 0.5-1%. In such condition, there is a flow-oriented slender disturbance near the wall in the boundary layer of attached laminar flow: these instabilities are mainly streaking structure or Klebanoff distortions. They are jet-like disturbances that move back and forth, alternate periodically in the wing span direction, and have the same wavelength order as the thickness of the boundary layer. The streaks are caused by the depth penetration of the low-frequency interference which cannot be buffered by the laminar shear layer, contrary to the high-frequency interference. This damping effect is called shear-sheltering. The laminar boundary layer is disturbed by streaks and vulnerable to instability. A marked feature is that the streak pattern has the characteristics of large wavelength, while the unstable pattern is a short wave. This means that although the unstable mode can be damped by the boundary layer, it is very easy to be stimulated by high frequency disturbances. The streak structures grow in length and amplitude downstream and eventually break down, resulting in turbulent spots in flow direction, which the progress is the bypass transition. Therefore, the unstable mechanism is caused by bypass transition of T-S waves, and can complete the flow breakup faster.

2.6.3 Separation induced transition

In the condition of adverse pressure gradient, the separation of the laminar boundary layer occurs on the curved surface, while the transition occurs near the surface in the free shear layer flow. The phenomena and progress of separation have been described in Section 2.4. If laminar separation bubbles are formed, the flow state will transfer from laminar to turbulent flow. The transition of separated flow has universality in turbomachinery, including the minimum pressure point on the suction side of high-loaded gas turbine or compressor blade.

A pressure distribution with characteristics of laminar separation bubble is obtained in the region that close to separation, as shown in Fig. 2.15. At the position of separation starts, the effect of displacement thickness on the outer layer flow is given due to the existence of separation bubble, with a pressure plateau appears. Therefore, there are two kinds of separation bubbles and two corresponding separation mechanisms: long bubbles and short bubbles, which the difference lies in the effect on the overall pressure distribution. Short separation bubbles only have the effect of local displacement, while the pressure distribution before and after separation bubble is very close to that predicted by the surface without separation. Long separation bubble interacts with external flow, resulting in a significant change in the pressure distribution on the surface. Both the changes of blade flow-stream angle of attack or velocity (Reynolds number) can cause the sudden variation of separating bubbles from short size to large size: the long separating bubbles produce more substantial flow losses, also the exit flow deviation should be avoided.

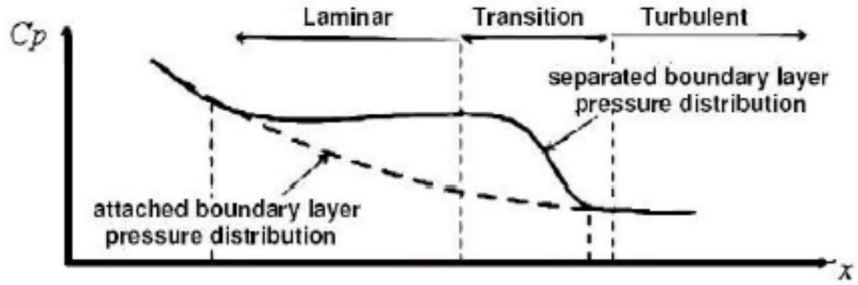

Fig. 2.15 – Effect of the separation bubble on the pressure distribution along a solid wall

Conversely, short and small separation bubbles can be used as a means of forcing flow into turbulence to improve the performance, especially in low-pressure turbine and compressor of medium-sized engines [11]. The variation from short separation bubbles to large ones is called bursting. The sudden occurrence of passages from one type to another involves a significant increase in losses and a sudden change in the direction of flow away from the trailing edge on a flat plate or turbomachinery blades. The burst can be activated by small variations of the Reynolds number, being a discontinuous process. The transition process can be described as follows, as suggested by Simoni et al.: the boundary layer is still attached to the wall upstream of the separation point, and the low-frequency disturbance causes the generation both of high-speed and low-speed streaks, similar to the bypass transition mechanism. During the downstream movement, they are amplified and become to have the characteristics of non-uniformity along the spreading direction within the flow. These vibrations interact with the separated shear layers and develop with an algebraic growth, resulting in deeper low-frequency disturbances. When the growth process reaches saturation, the streaks break up, which results in higher frequency disturbance in the flow. These high-frequency components correspond to the frequency range of Kelvin-Helmholtz (K-H) waves and produce disturbances in the boundary layer. In this condition, the disturbances are amplified exponentially through the unstable mechanism until they cause the separation shear layer to roll up. As a result, large-scale vortices are released around the maximum thickness of the separation bubble. The breakup of these structures causes a transition of the downstream shear layer: at this point, the mixing effect associated with turbulent conditions causes momentum to propagate towards the near-wall layer, leading to flow reattachment. Hatman and Wang [10] identified three possible separation models, which are different from laminar separation and transition separation. For short or large laminar separation, transition

occurs downstream of separation point. When T-S waves appear before separation, they can be identified by the buffer or amplification process of the separation shear layer. Short separation bubbles, whose length ranges from 100 to 1000 times of δ*, occur under suitable Reynolds number and weak adverse pressure gradient. After separation bubbles, boundary layer reattachment will occur. Long separation bubbles are larger than 10000 times the size of δ*, usually occurring at lower Reynolds number and stronger adverse pressure gradient. Although there is the possibility of T-S wave occurrence, the transition is delayed at the maximum thickness of the separation bubble and can cause K-H instability, which has nothing to do with the development and separation of flow. Separation transition occurs at suitable Reynolds number, where it is laminar boundary layer and ahead of separation point that caused by T-S waves or streaks, depending on the turbulence level of the incoming flow. It is terminated by K-H instability, coupled periodically, amplified and interacted with the wall and forced reattachment of flow, as described by Simoni.

2.6.4 Wake induced transition

The fourth transition mode is induced by wake. In turbomachinery, the wakes generated by impacting upstream blades play a fundamental role, and they interact with the attached boundary layer. When the disturbance driven by wakes is moderate, due to the typical free-flow turbulence intensity level of turbomachinery, the distortion characteristics similar to the statistically stable mean flow can be obtained, and the bypass transition characterized by streaks can be obtained. The mechanism of wake induced transition is referred in Fig. 2.16.

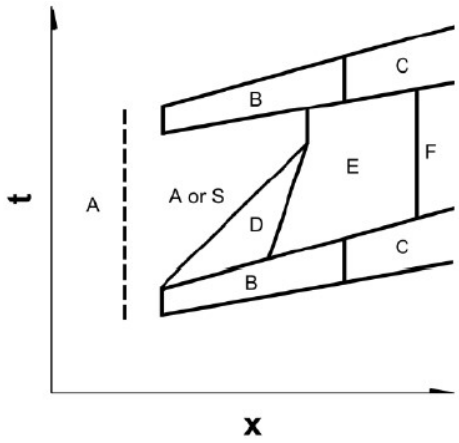

Fig. 2.16 – Wake induced transition diagram. The A zone stands for laminar flow, B is for transitional under wake impact, C represent turbulent flow after the impact, D is the calmed zone, E and F are, respectively, transitional and turbulent between the passage of two wakes. S represents the condition of separated boundary layer.

Along the path under wakes of the blade surface, the attached boundary layer begins as laminar and undergoing transition as it moves downstream until it becomes turbulence. Between two wakes, the evolution of the boundary layer is similar to that of the wake passing through, but its transition appears and ends later. This is mainly due to the relaxation of the boundary layer towards the laminar flow state, while the velocity profile maintains the characteristics of the turbulent boundary layer, and the turbulence level suddenly decays. The mixing effect of these phenomena makes the boundary layer stable, which increases its resistance to transition and separation in the calmed region. If a separation zone precedes the

transition one in laminar flow, turbulent spots generated by the wakes can periodically suppress or reduce the size of the separated bubbles.
A transition process can be altered by strong kinematic impact of wakes. In the turbine stator, wakes generated by upstream rotor can generate a jet with pressure of the guide vane moving towards suction side. The acceleration caused by leading part of the jet in the boundary layer can cause transition and local backflow in the front of jet due to the adverse pressure gradient. K-H instabilities can then occur in outer part of boundary layer, leading to a much faster bursting than with by-pass transition in a statistically steady mean flow [33].

2.7 Stability Theory

The basic idea of stability theory comes from the conjecture of O. Reynolds (1894), that laminar flow is always the possible solution of the equation of motion, but becomes unstable and turbulent above a certain limit (i.e. undifferentiated Reynolds number). These theoretical studies assume that laminar flow is affected by small disturbances, which may come from the entrance of pipeline or from the irregularity of wall roughness or external flow in the boundary layer of an object. The theory follows the rate of variation of the disturbance superimposed on the laminar basic flow. The decisive question here is whether these disturbances disappear or keep pace with time. If the disturbance disappears in time, the basic flow is considered to be stable; if the disturbance increases, the basic flow is unstable, and laminar-turbulent transition may occur. In this way, the stability theory of laminar flow can be developed. The purpose is to determine the undifferentiated Reynolds number for a given laminar flow.

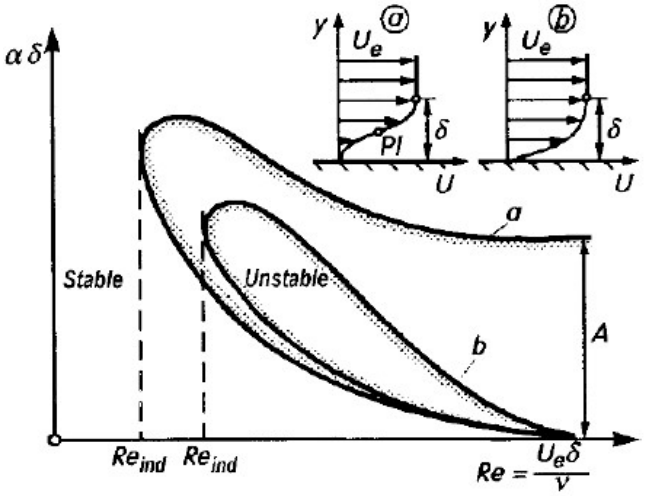

Fig. 2.17 – Curves of neutral stability of a plane boundary layer for two-dimensional incompressible perturbations: curve "a"-inviscid instability, curve "b"-viscous instability

In the study of laminar flow stability, the flow is divided into basic flow and small disturbance superimposed on it. Among them, the basic flow is the solution of N-S equations or boundary layer solution, and it is generally considered that the magnitude of small disturbance is much smaller than that of the basic flow. Furthermore, the goal of stability research is to determine whether the disturbance will disappear with time for a given basic flow, so that the basic one can be divided into stable flow and unstable flow. For two-dimensional incompressible flow problems, the stability analysis of laminar boundary layer

is transformed into the eigenvalue problem of perturbation differential equations with specific boundary conditions by introducing appropriate flow functions. In a given basic flow, the eigenvalues Cr and Ci form a neutral stability curve in the plane composed of flow parameters α and Re. Therefore, the stable and unstable solutions of the perturbed differential equations are distinguished, as shown in Fig. 2.17. However, the minimum Reynolds number corresponding to the curve is the critical value. Under this critical value, all modes can be blocked, while in the cases that the values are above the critical Reynolds number, some modes will be amplified. The minimum Reynolds number on the neutral stability curve is the theoretical undifferentiated Reynolds number of the laminar flow studied, that is, the stability limit. Applying this process to Blasius solution, the neutral stability curve and critical Reynolds number of the plate boundary layer can be obtained, which are not explained detailed here.

The stability theory first proposes the conclusion that the Reynolds number as the stability limit has the same order of magnitude as the experimental critical Reynolds number. The core idea of this theory is that small perturbations based on a certain wavelength and frequency are amplified, while those perturbations with smaller and larger wavelength ranges are blocked, assuming that the Reynolds number exceeds the above limit. According to this theory, long-wave disturbances with wavelength equal to several times the thickness of the boundary layer are more dangerous. The amplification of unstable disturbance sources is believed to ultimately lead to the transition of laminar to turbulent flows.

Chapter 3

Numerical Method

With the rapid development of Computational Fluid Dynamics (CFD) technology, more and more works began to study laminar separation flow phenomena and the mechanism of transition process from the perspective of numerical simulation. The ability to accurately predict the fluid characteristics of the transition process is of great importance to the systematic engineering design, including the field of turbomachinery concerned in the present work. At present, many CFD methods for solving boundary layer flow with transition problem are available: from the early "engineering perspective" based highly empirical methods, such as selecting the appropriate transition position and only applying the turbulence model downstream of the location, or the method which using turbulence model that reflects the actual process of transition, and then to the application of Direct Numerical Simulation (DNS) method [34]. Although the calculation ability is not as accuracy as that of Large Eddy Simulation (LES) and Direct Numerical Simulation (DNS), from the design point of view, the Reynolds Average Navier-Stokes (RANS) solving method means a compromise between the accuracy and cost of solution, which has been adopted by a large number of researchers and developed a variety of boundary layer transition prediction strategies. The simplest solutions based on RANS are the low Reynolds number eddy-viscous turbulence models without modification. These methods have been successfully applied in predicting transition flows [35-38]. Recent critical studies of several such models have shown that their ability to simulate transition is actually an accidental product of the model rather than a reflection of any real prediction [39], but they are still useful choices, especially in engineering simulations.

For a long time, researchers carried out a large number of studies on turbulence models based on RANS to predict the flow transition behavior. There are two methods adopted by commercial software. One is to couple the full turbulence model with the empirical transition correction, and the other is to add the transport equations to the turbulence model in order to consider the effect of the transition flow. The former is modified appropriately based on experimental data which can be obtained from relatively simple models and flow conditions. Several well-known modified models for predicting the onset of transition are introduced in literature [11] and [40-42], and some new versions are being developed [43]. Empirical correlation couples the turbulence model with some assumptions, such as assuming that transition is completed instantaneously at a certain position in the flow field, or incorporating the transition region into the numerical simulation through the general intermittent profiles proposed by Dhawan and Narasimha. This method encountered some difficulties in the implementation process, especially for a complex 3D geometry. Generally, the correlation is based on the downstream distance (x) or the momentum thickness (θ) of the boundary layer. Compared with the single-point model commonly used for complete turbulence, non-local or global parameters are needed in the simulation. The development of techniques for calculating such non-local quantities is an area of current research, but there are still problems in the use of these methods for more complex three-dimensional geometries [44-46].

The more common method is to use additional transport equations, or model terms, to contain the prediction of flow transition. Typical examples include phenomenological

models [47-49] or correlation-based models [50-52]. Within each category, most models still require model terminology to contain the information about non-local or integral parameters, which makes it difficult to incorporate them into general CFD code. Recent studies have focused on the use of single-point models, including Wang's and Perot's phenomenological models, Walters and Leylek's phenomenological model currently used in commercial CFD code Fluent (Ansys, Inc., Canonsburg, PA), and Menter's et al. correlation-based model that is currently used in the commercial code CFX (Ansys, Inc., Canonsburg, PA). They are the most general and easy-to-implement CFD prediction method for laminar, transition and turbulent flows in the single point model of commercial specifications. Up to now, the correlation form of two equations eddy viscosity models and the additional transport equations have been used in the proposed model. These equations include turbulent potential terms, intermittency and transition Reynolds number terms or laminar flow energy to represent pre-transition fluctuations in laminar wall-attached or separated boundary layers. Each method aims at the same goal: providing a relatively simple, single-point, RANS-based model for predicting laminar-turbulent transition for CFD end users, and ensuring the accuracy, efficiency and stability of the model. None of these methods is likely to be a "magic bullet" for predicting transitions, but their availability provides designers and application engineers with useful new tools for analyzing complex flow systems.

3.1 Governing Equations

The continuity equation and Navier-Stokes equations in an incompressible and viscous three-dimensional flow, which also neglecting forces of volume, can be used as the basis of the boundary layer flow differential equations.

$$\frac{\partial u}{\partial t}+u\frac{\partial u}{\partial x}+v\frac{\partial u}{\partial y}+w\frac{\partial u}{\partial z}=-\frac{1}{\rho}\frac{\partial P}{\partial x}+\nu\left(\frac{\partial^2 u}{\partial x^2}+\frac{\partial^2 u}{\partial y^2}+\frac{\partial^2 u}{\partial z^2}\right) \tag{3.1}$$

$$\frac{\partial v}{\partial t}+u\frac{\partial v}{\partial x}+v\frac{\partial v}{\partial y}+w\frac{\partial v}{\partial z}=-\frac{1}{\rho}\frac{\partial P}{\partial y}+\nu\left(\frac{\partial^2 v}{\partial x^2}+\frac{\partial^2 v}{\partial y^2}+\frac{\partial^2 v}{\partial z^2}\right) \tag{3.2}$$

$$\frac{\partial w}{\partial t}+u\frac{\partial w}{\partial x}+v\frac{\partial w}{\partial y}+w\frac{\partial w}{\partial z}=-\frac{1}{\rho}\frac{\partial P}{\partial z}+\nu\left(\frac{\partial^2 w}{\partial x^2}+\frac{\partial^2 w}{\partial y^2}+\frac{\partial^2 w}{\partial z^2}\right) \tag{3.3}$$

$$\frac{\partial u}{\partial x}+\frac{\partial v}{\partial y}+\frac{\partial w}{\partial z}=0 \tag{3.4}$$

Apply the equations above to *x*-*y* plane in a Cartesian coordinate system, where the coordinate axes *x* and *y* correspond to the flow direction and perpendicular to the flow direction, respectively.

$$u\frac{\partial u}{\partial x}+v\frac{\partial u}{\partial y}=-\frac{1}{\rho}\frac{\partial P}{\partial x}+\frac{1}{\rho}\frac{\partial}{\partial x}\left(\mu\frac{\partial u}{\partial x}\right)+\frac{1}{\rho}\frac{\partial}{\partial y}\left(\mu\frac{\partial u}{\partial y}\right) \tag{3.5}$$

$$u\frac{\partial v}{\partial x}+v\frac{\partial v}{\partial y}=-\frac{1}{\rho}\frac{\partial P}{\partial y}+\frac{1}{\rho}\frac{\partial}{\partial x}\left(\mu\frac{\partial v}{\partial x}\right)+\frac{1}{\rho}\frac{\partial}{\partial y}\left(\mu\frac{\partial v}{\partial y}\right) \tag{3.6}$$

$$\frac{\partial u}{\partial x}+\frac{\partial v}{\partial y}=0 \tag{3.7}$$

For the boundary layer along a flat plate with length L, the dimension analysis is applied to correlate the terms in the equations with the flow-related physical quantities, thus further simplifying the equations. Among them, x and L have the same order of magnitude, u and inflow velocity U_e have the same order of magnitude, y corresponds to boundary layer thickness δ, and viscosity ν to the ratio of the first three, i.e.

$$u \sim U_e \quad x \sim L \quad y \sim \delta \quad \nu \sim U_e \frac{\delta}{L}$$

It is noted that the length L of the plate in the direction of flow is much larger than the thickness of the boundary layer δ, that is $\delta/L \ll 1$. The laminar boundary layer equations can be further simplified as following by substituting these terms into the equations and ignoring the higher order terms.

$$u\frac{\partial u}{\partial x} + v\frac{\partial u}{\partial y} = -\frac{1}{\rho}\frac{\partial P}{\partial x} + \frac{1}{\rho}\frac{\partial}{\partial y}\left(\mu\frac{\partial u}{\partial y}\right) \tag{3.8}$$

$$\frac{\partial P}{\partial y} = 0 \tag{3.9}$$

$$\frac{\partial u}{\partial x} + \frac{\partial v}{\partial y} = 0 \tag{3.10}$$

In particular, it can be found from equation (3.9) that the pressure is constant along the direction perpendicular to the wall in the boundary layer flow.
Apply these equations to laminar and turbulent boundary layer respectively, we can obtain the results with engineering application value. The laminar flow result in an incompressible zero-angle-of-attack plane boundary layer is the Blasius solution (see Section 2.2). Accordingly, both density and viscosity keep constant in such conditions.

3.2 RANS Simulation

Typical turbulence is the result of an unstable laminar flow which developing to a certain critical Reynolds number. In such flow, these instabilities are caused by the amplification of higher order nonlinear inertial terms' perturbations. According to the widely accepted "energy cascade" theory proposed by Kolmogorov, turbulence is composed by vortices of different geometric scales, and each vorticity corresponds to a certain energy depending on its dimension. Usually, large-scale vortices break up into small-scale ones, which will break down into smaller vortices. During this process, energy will be transferred from large-scale vortices to lower-level vortices until the breakdown reaches the minimum scale that can be achieved. Ultimately, these are equivalent to the minimum-scale vortices with molecular-level viscosity, which dissipate turbulent energy effectively in the form of heat.
In addition to using DNS or LES methods to calculate vortices at full or partial scales, the most effective method in engineering is still based on using Reynolds averaged turbulence model. Its static average is not based on spatial averaging, but on the appropriate time averaging. The key is to decompose the flow variables into time averages and fluctuations, and to substitute them into the governing equations. By this method, the continuous process in time is discretized to a limited extent, and when the statistical time scale is small enough, the approximate continuous process satisfying the accuracy can be obtained.

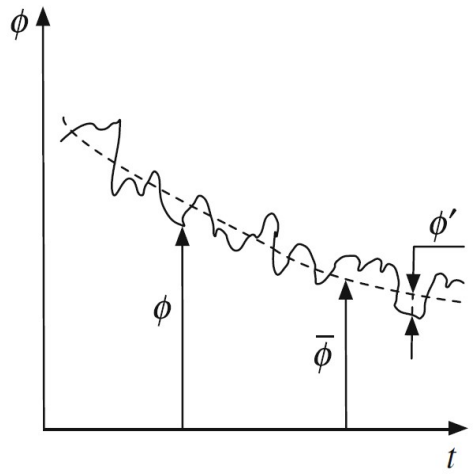

Fig. 3.1 – Fluctuating and mean variable components

In Reynolds averaging, the solution variables in the instantaneous (exact) Navier-Stokes equations are decomposed into the mean (ensemble-averaged or time-averaged) value and the fluctuating components. For example, each velocity component can be decomposed as:

$$u_i = \bar{u_\iota} + u_i'$$

where $\bar{u_\iota}$ and u_i' are the mean and fluctuating velocity components ($i = 1,2$) respectively. Likewise, for pressure and other scalar quantities, there is:

$$\phi_i = \bar{\phi_\iota} + \phi_i'$$

where ϕ denotes a scalar such as pressure, energy, or species concentration. The relationship of averaged variable and fluctuations is explained in Fig. 3.1.
Substituting expressions of this form for the flow variables into the instantaneous continuity and momentum equations and taking a time (or ensemble) average (and dropping the overbar on the mean velocity) yields the ensemble-averaged momentum equations. They can be written in Cartesian tensor form as:

$$\bar{u}\frac{\partial \bar{u}}{\partial x} + \bar{v}\frac{\partial \bar{u}}{\partial y} = -\frac{1}{\rho}\frac{\partial \bar{P}}{\partial x} + \frac{1}{\rho}\frac{\partial}{\partial x}\left(\mu\frac{\partial \bar{u}}{\partial x} - \rho\overline{u'^2}\right) + \frac{1}{\rho}\frac{\partial}{\partial y}\left(\mu\frac{\partial \bar{u}}{\partial y} - \rho\overline{u'v'}\right) \quad (3.11)$$

$$\bar{u}\frac{\partial \bar{v}}{\partial x} + \bar{v}\frac{\partial \bar{v}}{\partial y} = -\frac{1}{\rho}\frac{\partial \bar{P}}{\partial y} + \frac{1}{\rho}\frac{\partial}{\partial x}\left(\mu\frac{\partial \bar{v}}{\partial x} - \rho\overline{u'v'}\right) + \frac{1}{\rho}\frac{\partial}{\partial y}\left(\mu\frac{\partial \bar{v}}{\partial y} - \rho\overline{v'^2}\right) \quad (3.12)$$

$$\frac{\partial \bar{u}}{\partial x} + \frac{\partial \bar{v}}{\partial y} = 0 \quad (3.13)$$

They are called Reynolds-Averaged Navier-Stokes (RANS) equations, which have the same general form as the instantaneous Navier-Stokes equations, with the velocities and other solution variables now representing ensemble-averaged (or time-averaged) values. Additional terms now appear that represent the effects of turbulence, such as $\overline{u'v'}, \overline{u'^2}$ and $\overline{v'^2}$. They are Reynolds stress tensor components both in tangential and normal directions, the mathematical representation of the stresses induced in the fluid by turbulent phenomena. Also applying the same considerations on orders of magnitude as in the laminar case, the system of equations can be simplified, as the equations for the turbulent boundary layer:

$$\bar{u}\frac{\partial \bar{u}}{\partial x}+\bar{v}\frac{\partial \bar{u}}{\partial y}=-\frac{1}{\rho}\frac{\partial \bar{P}}{\partial x}+\frac{1}{\rho}\frac{\partial}{\partial y}\left(\mu\frac{\partial \bar{u}}{\partial y}-\rho\overline{u'v'}\right) \tag{3.14}$$

$$\frac{1}{\rho}\frac{\partial \bar{P}}{\partial y}=0 \tag{3.15}$$

$$\frac{\partial \bar{u}}{\partial x}+\frac{\partial \bar{v}}{\partial y}=0 \tag{3.16}$$

Observed results show that there is still a negligible pressure gradient perpendicular to the wall in the turbulence equations. The tangential component of the additional Reynolds stress term appearing in the equation has a mixed effect in the boundary layer, leading to more unknowns and makes the equations not closed, hence that is the main problem need to be solved in RANS calculation.

The direct modeling of Reynolds stress tensor is based on Boussinesq hypothesis, which is similar to Newtonian flow and assumes that Reynolds stress is a linear function of average velocity gradient. For incompressible flows, the expression is

$$\rho\overline{u_i u_j}-\frac{1}{3}\rho\overline{u_k u_k}\delta_{ij}=-2\mu_T S_{ij} \tag{3.17}$$

Where μ_T is turbulent or vorticity, viscosity.

In particular, k is defined as turbulent energy, which is an important parameter in both subsequent calculation and turbulence model. Its expression is as follows:

$$k=\frac{1}{2}\overline{u_i' u_i'} \tag{3.18}$$

The classical two-equation turbulence model also uses turbulent dissipation rate ε. For Reynolds stress models based on the ε-equation, the dissipation tensor ε_{ij} is modeled as

$$\varepsilon_{ij}=\frac{2}{3}\delta_{ij}\rho\varepsilon(1+2k/a^2) \tag{3.19}$$

With this approximation, the problem of calculating the Reynolds stress components is transformed into computing the turbulent kinetic energy and turbulent viscosity. This is a common model based on the basic CFD of RANS nowadays. Its primary advantage lies in its simplicity, while the primary challenge lies in the fact that the corresponding effect of velocity fluctuation must be based on the single parameter of eddy viscosity. Based on the emphasis of this work, the turbulence models described below are all focused on the determination of laminar-turbulent transition.

3.3 Turbulence and Transition Models

In the process of RANS simulation, a turbulence model is needed to add to Reynolds stress term in the momentum equation in order to close Navier-Stokes equations system, while the turbulence model with two equations allows the turbulent length and time scale to be determined by solving two independent transport equations. The standard $k-\varepsilon$ model is one of the representative models. It is based on the turbulence kinetic energy (k) and its dissipation rate (ε). Since Launder and Spalding [53] proposed the standard $k-\varepsilon$ model, it has been adopted by commercial code and become the main force of actual engineering flow

calculation. Robustness, economy and reasonable accuracy for a wide range of turbulent flows explain its popularity in industrial flow and heat transfer simulation.

The standard $k-\varepsilon$ model is a semi-empirical model, and the derivation of its model equation depends on phenomenology and experience. The transport equation k is derived from the exact equation, while the transport equation ε is derived from physical reasoning, which has little similarity with mathematically exact transport equation of the model. In the derivation of the model, it is assumed that the flow is completely turbulent and the effect of molecular viscosity can be neglected. Therefore, the standard model can only be applied to a complete turbulence, i.e. high Reynolds number conditions, or free flow far away from the wall. As the advantages and disadvantages of the standard $k-\varepsilon$ model are gradually known, people have improved it and developed different $k-\varepsilon$ models to improve its performance. However, the solution with high accuracy cannot be obtained for the flow with laminar-turbulent transition process in the region near to the wall.

To this end, researchers continuously proposed new turbulence models through in-depth study of the transition mechanism [54]. The turbulence models described below are representative of them, they are Shear Stress Transport model, Transition Shear Stress Transport model and Transition $k-kl-\omega$ model, respectively. Among them, the first two have similar basis and inheritance-development relationship, but different transport equations are adopted. In Ansys Fluent, the latter two are labeled as transition-type models, due to the reason that both of the two models use a separate parameter as criterion of transition. These three models have been verified in practical applications, and their specific differences will be described in detail.

3.3.1 Shear Stress Transport（SST $k-\omega$）model

To compensate for the shortcomings of $k-\varepsilon$ model, researchers have developed $k-\omega$ model to calculate the flow near the wall, such as Wilcox $k-\omega$ model and improved standard $k-\omega$ model. The standard $k-\omega$ model is still an empirical model, which is based on two transport equations, one of which is still the turbulence kinetic energy k equation, and the other is the specific dissipation rate ω instead of the dissipation rate, ε. At the same time, the standard $k-\omega$ model incorporates modifications for low Reynolds number effects, compressibility, and shear flow spreading. As the $k-\omega$ model has been modified over the years, production terms have been added to both k and ω equations, which have improved the accuracy of the model for predicting free shear flows.

The $k-\omega$ model can be applied to the bottom region of the boundary layer without damping functions. Therefore, it is simpler than the previous two-equation models. Meanwhile, it also has better numerical stability than previous models in practical application. In the prediction of mean flow profile, it is as accurate as other models. Without any other modifications, Wilcox developed the $k-\omega$ model and applied it to rough wall flow and surface mass injection problems. The $k-\omega$ model has also been used in the logarithmic region of the boundary layer, which has been proved that it outperforms the $k-\varepsilon$ model in the logarithmic region of the equilibrium flow with APG condition and compressible flow.

Although it can be applied to the near-wall region, the asymptotic behavior of turbulence near the wall cannot be correctly predicted by $k-\omega$ model, which is the same as the previous models. However, Taylor series expansion of Navier-Stokes equations, which is the basis of analysis, is only valid as it directly approaches the wall. The eddy viscosity is much smaller than the molecular viscosity when it is close to the surface, while the asymptotic behavior of mean flow profile is independent of the asymptotic form of

turbulence. Therefore, even though the turbulence model is not asymptotically consistent, the predictions of mean flow profile and wall friction are still correct. In addition, the $k-\omega$ model does not accurately represent k and ε distribution in agreement with DNS data. While the $k-\varepsilon$ model develops a large number of damping functions, which improves its consistency with DNS data.

Researchers have to abandon the $k-\omega$ model in the wake region of boundary layer, especially in the investigation of turbomachinery. The reason is that the $k-\omega$ model is very sensitive to the conditions of freestream outside the boundary layer, which results in the instability of the solution.

For another issue that researchers concerning, the traditional two-equation model, including the $k-\omega$ model, is more restricted to the logarithmic region due to the flow separation induced by the adverse pressure gradient. Although the behavior of the model in logarithmic region is also important, especially in the flow with moderate pressure gradient, the vorticity level in the wake region ultimately determines the ability of the vorticity model to predict the flow with strong adverse pressure gradient. This is clearly demonstrated by the improvement of the Johnson-King model which is superior to the standard algebraic model by reducing the eddy viscosity in the wake region of the adverse pressure gradient flow. The limited influence of logarithmic region on the result of strong adverse pressure gradient is also obvious. Although $k-\omega$ model has superior logarithmic region characteristics, it cannot accurately predict pressure induced separation.

By introducing the characteristics of the $k-\omega$ model, we can see that although it is designed to analyze the near-wall flow, the $k-\omega$ model still has great limitations. On this basis, F. R. Menter developed and proposed two new turbulence models in 1994 [55]: the baseline (BSL) $k-\omega$ model and the shear layer transport (SST) $k-\omega$ model. The BSL model uses the original $k-\omega$ model in the inner region of the boundary layer, while the standard $k-\omega$ model is used in the external free shear flow. Its characteristics are similar to Wilcox model, but it avoids the model sensitivity to freestream. The SST $k-\omega$ model comes from redefining the eddy viscosity contained in the BSL model, i.e. paying more attention to the transport effect of the main turbulent shear stress, so it is called the shear force transport model, and has made remarkable progress in predicting the adverse pressure gradient flow. They are still two-equation eddy-viscous turbulence models based on engineering applications.

The concept implied in BSL model is to ensure the stability and accuracy of the equations in the near-wall region, and to make progress in the independence of $k-\varepsilon$ model to freestream in the outer boundary layer. In order to obtain the required features in different regions, the high Reynolds number version of the standard $k-\varepsilon$ model will be transformed into the $k-\omega$ equation. The original model is then multiplied by a function F_1 and the transformed model by a function $(1-F_1)$, and both are added together. The mixed function will be designed as 1 in the sublayer and logarithmic region of the boundary layer, but will gradually switch to 0 in the wake region. This means that the BSL model will be based on the $k-\omega$ common formula. The original Wilcox model will be activated in the near wall region and the standard $k-\varepsilon$ model will be activated in the outer wake region and the free shear layer. After the above process, the transport equations are as follows:

$$\frac{D(\rho k)}{Dt}=\tau_{ij}\frac{\partial u_i}{\partial x_j}-\beta^*\rho\omega k+\frac{\partial}{\partial x_j}\left[(\mu+\sigma_k\mu_t)\frac{\partial k}{\partial x_j}\right] \tag{3.20}$$

$$\frac{D(\rho\omega)}{Dt} = \frac{\gamma}{\nu_t}\tau_{ij}\frac{\partial u_i}{\partial x_j} - \beta\rho\omega^2 + \frac{\partial}{\partial x_j}\left[(\mu + \sigma_\omega\mu_t)\frac{\partial\omega}{\partial x_j}\right] + 2\rho(1-F_1)\sigma_{\omega 2}\frac{1}{\omega}\frac{\partial k}{\partial x_j}\frac{\partial\omega}{\partial x_j} \tag{3.21}$$

The coefficients in the new model are expressed as φ, in the Wilcox $k-\omega$ model as φ_1, and in the standard $k-\varepsilon$ model as φ_2, then the relationship among them is as follows:

$$\varphi = F_1\varphi_1 + (1-F_1)\varphi_2 \tag{3.22}$$

The coefficients in the equations and the mixed function are not explained in detail here.
In the second step, the definition of eddy viscosity will be modified according to the transportation of the main turbulent shear layer. The resulting model will be referred to as the shear layer transport model. It will greatly improve the performance of the initial $k-\omega$ model and the standard $k-\varepsilon$ model. The BSL $k-\omega$ model described previously combines the advantages of the Wilcox and the $k-\varepsilon$ model, but still fails to properly predict the onset and amount of flow separation from smooth surfaces. The main reason is that both models do not account for the transport of the turbulent shear stress. This results in an over-prediction of the eddy-viscosity. But in SST $k-\omega$ model, the proper transport behavior can be obtained by a limiter to the formulation of the eddy-viscosity, the definition is as following:

$$\mu_T = \frac{\rho k}{\omega}\frac{1}{max\left[\frac{1}{a^*}, \frac{SF_2}{a_1\omega}\right]} \tag{3.23}$$

where S is the strain rate magnitude, while the coefficient a^* damps the turbulent viscosity causing a low Reynolds number correction. F_2 is another blending function which is given by

$$F_2 = tanh(\phi_2^2) \tag{3.24}$$

$$\phi_2 = max\left[2\frac{\sqrt{k}}{0.09\omega y}, \frac{500\mu}{\rho y^2\omega}\right] \tag{3.25}$$

According to the definition, when the product of S and blending function F_2 are very small, μ_T will be restored to the initial form, which corresponds to the region far from the wall. On the contrary, when the product of S and blending function F_2 increase gradually, the value of μ_T decreases gradually. When the product of the two terms is quite large, the viscosity μ_T will be limited. At this time, the corresponding wall distance y is very small, that is, the area near the wall. Therefore, the process can be regarded as a Viscosity Limiter, which results in better agreement with experimental measurements of separated flow.
In addition, similar to the functional relationship used among coefficients in BSL function, the coefficients of the new model are

$$\varphi = F_2\varphi_1 + (1-F_2)\varphi_2 \tag{3.26}$$

Among them, the coefficients adopted by φ_2 are consistent with those of BSL model, while φ_1 adopts new values. Finally, the constant coefficients used in the model are as follows:

$$\sigma_{k,1} = 1.176, \sigma_{\omega,1} = 2.0, \sigma_{k,2} = 1.0, \sigma_{\omega,2} = 1.168$$

$$a_1 = 0.31, \beta_{i,1} = 0.075, \beta_{i,2} = 0.0828$$

The SST $k-\omega$ model includes all the refinements of the BSL $k-\omega$ model, and in addition accounts for the transport of the turbulence shear stress in the definition of the turbulent viscosity. These features make the SST $k-\omega$ model more accurate and reliable for a wider class of flows (for example, adverse pressure gradient flows, airfoils, and transonic shock waves) than the standard and the BSL $k-\omega$ models.

3.3.2 Transition Shear Stress Transport model

Menter summarizes the characteristics of turbulence models developed for prediction of transition, and he believes that the engineering prediction of transition is mainly based on two model concepts. The first is the application of the low Reynolds number turbulence model, which its wall dumping function implied in the turbulence model causes transition. This concept is positive because it is based on transport equation and can be effectively implemented in realizable CFD code applications. However, in reality, the difficulties are that many factors that affect the transition cannot be truly reflected, including turbulence, pressure gradient and separation, turbulence length scale, Mach number, wall roughness, streamline curvature and so on [56-58]. The reason is that the low Reynolds number model is a coincidence for predicting transition, but it does not give an internal explanation of a completely different and complex physical process reliably by optimizing the function used to suppress viscous sublayer turbulence. Although some low Reynolds number models with explicit information about the transition mechanism have been developed, together with significant improvements have been made in prediction, they are still limited by the correlation between the transition calibration and the viscous bottom equation. Hence, they are not widely used in engineering computational fluid dynamics.

The second method uses experimental correlation and is popular in the field of low Reynolds number engineering. Reynolds number of momentum thickness $Re_{\theta t}$ is usually correlated with the occurrence of turbulence intensity Tu in the freestream. Although this method proves to be accurate enough, it challenges the numerical calculation and programming of Navier-Stokes codes. For the classical correlation-based transition model, it is necessary to compare the real Reynolds number of momentum thickness Re_θ with the correlation-based transition value $Re_{\theta t}$. In the actual calculation process, the factors such as the unstable search algorithm caused by the insufficient definition of boundary layer edge, the difficulty of unstructured mesh to provide the basic conditions for integrating global boundary layer parameters, and the incompatibility between code and general parallel CFD program, make the model usually valid only for specific situations and geometric shapes within special internal CFD code. The modified model is closely related to the intermittency transport equation. In any case, these models need non-local information to excite the source term in the intermittency equation. Due to the fact that the main input is provided by experimental correlation, the prediction ability of the transport equation itself is limited, even when physical demonstration is used in the derivation process.

In 2002, Menter et al. [59] proposed a new correlation-based transition model, which is strictly based on local variables and avoids the need for non-local information. In the formulation, only local information is used to activate the source term in the intermittency equation. The connection between the correlation and the intermittency equation is established by using the vorticity Reynolds number. As a result, the model is compatible with computational fluid dynamics applications, such as unstructured grids and large-scale parallel computing. The model is based on two transport equations, one is the intermittency

transport equation, and the other is the criterion equation of transition onset based on the Reynolds number of momentum thickness. The proposed transport equation does not attempt to simulate the physical process of the transition (unlike the turbulence model), but to form a framework for implementing the correlation-based model into a general CFD method. Nevertheless, the model still cannot meet the practical application requirements of the transition prediction in engineering, and it needs further improvement both in numerical behavior and calibration.

Subsequently, Menter et al. made a lot of improvements to the previous equations and proposed a new model in 2006 [52]. Among them, the first equation is still intermittency transport equation, which can be used to induce the transition process. The equation is optimized and generalized on the basis of the original one. The second transport equation avoids the increase of non-local information introduced by the quantities used in the experimental correlations. Correlations are mainly based on freestream data, such as turbulence intensity or pressure gradient outside the boundary layer. The additional equation is established by using the Reynolds number of transition occurrence $Re_{\theta t}$. Outside the boundary layer, the transport variables are forced to follow the $Re_{\theta t}$ values provided by the experimental correlation. This information is diffused into the boundary layer through the standard diffusion term. By this mechanism, strong variations in turbulence intensity and pressure gradient, i.e. the typical information observed in industrial flows, can be taken into account.

Menter also argues that the new transport equation does not depend on the physical mechanism of the transition process (unlike the turbulence model), but on the method of bringing the correlation-based model into the overall purpose of CFD. The physics of the transition process is entirely contained in the experimental correlation provided to the model. Therefore, the formula is not only limited to a specific transition mechanism, such as bypass transition, but also can be applied to all mechanisms as long as the appropriate correlation can be provided. That is also adaptable to the study of other transition mechanisms.

The validated model was integrated by ANSYS Fluent and named Transition Shear Stress Transport (Transition SST) model, also known as ($\gamma - Re_\theta$) model. Like known to us, the model is based on the coupling of the SST $k-\omega$ transport equations with two other transport equations, one for the intermittency and one for the transition onset criteria, in terms of momentum-thickness Reynolds number. Hence, it is actually a four-equation model. In the Transition SST model, the transport equations of turbulence kinetic energy k and specify dissipation rate ω are still resolved, and all terms are the same as SST $k-\omega$ model, except for three terms, which including the production (P_k), the diffusion (D_k) and the blending function F.

In the production term, P_k is multiplied by the turbulence intermittency γ, which is the percentage of time that turbulent fluctuations are present in the boundary layer. By means of taking values from 0 to 1, the intermittency states the flow from laminar to fully turbulent. Hence intermittency is damping the production of turbulence where the boundary layer is laminar and transitional. For the dissipation term D_k, it is replaced with

$$D_k \times \min\left(\max(\gamma, 0.1), 1.0\right)$$

Hence it is another limiter that ensures that the dissipation does not drop below 10% of turbulent value. At the same time, the wall still damps turbulence even when the flow is laminar.

Then we have the k equation as following:

In a laminar boundary layer, the k equation is

$$\frac{\partial(\rho k)}{\partial t}+\frac{\partial\left(\rho U_j k\right)}{\partial x_j}=\frac{\partial}{\partial x_j}\left[\left(\mu+\frac{\mu_t}{\sigma_\gamma}\right)\frac{\partial k}{\partial x_j}\right]-0.1D_k \tag{3.27}$$

In a turbulent boundary layer, the k equation is

$$\frac{\partial(\rho k)}{\partial t}+\frac{\partial\left(\rho U_j k\right)}{\partial x_j}=\frac{\partial}{\partial x_j}\left[\left(\mu+\frac{\mu_t}{\sigma_\gamma}\right)\frac{\partial k}{\partial x_j}\right]+P_k-D_k \tag{3.28}$$

While for the blending function F_1 is corrected to prevent to be zero in the laminar boundary layer, which is expressed as followed, to make sure the model will not switch to the $k-\varepsilon$ model in the laminar boundary layer.

$$F_{1,new}=\max\left(F_1,F_3\right) \tag{3.29}$$

$$F_3=e^{-(R_y/120)^3}\ R_y=\frac{\rho y\sqrt{k}}{\mu} \tag{3.30}$$

The transport equation for the intermittency γ is defined as:

$$\frac{\partial(\rho\gamma)}{\partial t}+\frac{\partial\left(\rho U_j\gamma\right)}{\partial x_j}=P_{\gamma1}-E_{\gamma1}+P_{\gamma2}-E_{\gamma2}+\frac{\partial}{\partial x_j}\left[\left(\mu+\frac{\mu_t}{\sigma_\gamma}\right)\frac{\partial\gamma}{\partial x_j}\right] \tag{3.31}$$

While the transport equation for the transition momentum thickness Reynolds number is

$$\frac{\partial\left(\rho\widetilde{Re}_{\theta t}\right)}{\partial t}+\frac{\partial\left(\rho U_j\widetilde{Re}_{\theta t}\right)}{\partial x_j}=P_{\theta t}+\frac{\partial}{\partial x_j}\left[\sigma_{\theta t}(\mu+\mu_t)\frac{\partial\widetilde{Re}_{\theta t}}{\partial x_j}\right] \tag{3.32}$$

The details about the transport equations are introduced in **Appendix A**.
In practical use, the following restrictions are imposed in Transition SST model:
(1) It must be applied to a flow with bounded wall as boundary, but not to free shear flow. Otherwise, free shear flow will be predicted as complete turbulence.
(2) The Transition SST model is not Galilean invariant and should therefore not be applied to surfaces that move relative to the coordinate system for which the velocity field is computed; for such cases the Intermittency Transition model should be used instead.
The Transition SST model is designed for flows with a defined nonzero freestream velocity (that is, the classical boundary layer situation). It is not suitable for fully developed pipe/channel flows where no freestream is present. For the same reason, it is also not suitable for wall jet flows. For such scenarios, the Intermittency Transition model should be used instead.
The Transition SST model has not been calibrated in combination with other physical effects that affect the source terms of the turbulence model, such as buoyancy and multiphase turbulence.
In addition, a very powerful option has been included to allow to enter the user-defined empirical correlation, which can then be used to control the transition onset momentum thickness Reynolds number equation.

3.3.3 Transition $k-kl-\omega$ model

It can be seen from the above introduction that either SST $k-\omega$ model or Transition SST model, its essence is the relevance model based on the experimental results, which belongs to the empirical type. In contrast, researchers have been hoping to fully understand the

physical mechanism of transition and turbulent flow, that is, to establish a physical mechanism-based turbulence model, which belongs to the category of phenomenological modeling. One of the reasons why phenomenological modeling is more difficult and less applicable than empirical models is that the physical mechanism of transition is still not fully understood, and it is indeed an active research field. Therefore, some authors believe that the correlation-based model is more suitable for consistent RANS-based transition prediction than the physical-based one [52]. However, recent analytical, numerical and experimental studies have helped to highlight some basic physical mechanisms and general characteristics of boundary layer flows, including transition and turbulence. Knowledge of relevant scaling mechanisms may allow for reasonable and accurate model forms without resorting to purely empirical methods [34]. The Transition $k-kl-\omega$ model described below is such a turbulence model.

Transition $k-kl-\omega$ model is a new version of single-point eddy-viscous turbulence model with three additional transport equations. Its main idea is based on the general physical laws of transition and turbulent flow developed before. Although $k-\omega$ model is still the basic framework, it essentially improves the previously published models with transition sensitivity. It closes the relevant terms in the model based on physical phenomena rather than empirical methods, and discusses that these terms should have a reasonable form. The additional third transport equation includes the prediction of the low-frequency velocity fluctuation vector modulus in the pre-transition boundary layer, as previously identified for transition. The model has been validated by a large number of numerical examples and applied to commercial computational fluid dynamics software. It has been applied to a large number of related cases, including plate boundary layer flow with or without pressure gradient, and airfoil cases with different geometric characteristics, Reynolds number, turbulence level of incoming flow and angle of attack. These test cases prove that the model has the ability to successfully reproduce the transition flow behavior and has reasonable accuracy, especially for the compressible flow problems that cannot be predicted by the conventional model for laminar-turbulent transition development. This makes it possible to use a relatively simple Reynolds averaged model method to solve all complex transition characteristics and turbulent flow problems. The results show that the new model can provide a useful and practical tool, which has the ability to satisfy the requirements not only for simulation in engineering flow system but also to predict transition flow behavior. Subsequently, the physical basis of the modeling method is continuously expanded, which significantly improves the accuracy of a large number of demonstration test cases.

The conceptual description of Transition $k-kl-\omega$ model was first proposed by Walters and Leylek [49]. It deals with laminar flow, transition flow and complete turbulence in the framework of Reynolds averaging. The effect of unsteady velocity fluctuation on mean flow is represented by the appearance of Reynolds stress term in the time-averaged governing equation. Wang and Perot [48] suggest that, in theory, transition, like turbulent fluctuation, may be modeled by Reynolds stress tensor. When the value of Reynolds stress component is very small, stable laminar flow can be effectively “modeled”.

The concept of laminar flow energy k_L is adopted in the model, which is summarized by instability mechanism and transition mechanism in the process of studying laminar boundary layer. The results are of physical essence. Before transition, the average velocity profile of the boundary layer is completely laminar. For freestream with turbulence intensity less than 1%, the development of low-amplitude pre-transition velocity fluctuation is mainly controlled by self-maintaining instability mechanism, the most famous of which is Tollmien-Schlichting wave [30]. When the incoming turbulence intensity increases, the pre-

transitional boundary layer begins to be disturbed obviously from the typical Blasius profile, with a decrease in momentum in the outer region and an increase in the inner region, even the turbulence in the incoming region is less than 1% [60]. The variation of mean velocity profile is accompanied by flow fluctuation with relatively high-amplitude, and its intensity can reach several times of the freestream level [61]. This process results in the enhancement of surface friction and heat transfer in the pre-transition region, and eventually leads to transition through the rupture of the flow fluctuation. That is to say, the bypass transition introduced in Chapter 2 is caused by the existence of low-frequency/low-amplitude flow vortices in the boundary layer, which are shown as "stripe structures" in flow visualization, Direct Numerical Simulation [62] and Large Eddy Simulation [63].

In fact, this freestream fluctuation is not turbulence in the usual sense, but Klebanoff model [61]. Mayle and Schulz [64] applied this distinction to modelling. They proposed the concept of laminar kinetic energy to describe the development of pre-transition fluctuations leading to bypass transition, and suggested the usage of a second kinetic energy equation to control these fluctuations. Similar approaches have been gradually adopted in subsequent studies to model the pre-transitional region [65,66], which is ultimately defined as laminar kinetic energy k_L. Although the causes of laminar kinetic energy are not fully understood, it has been found that there are two important aspects affected: the selectivity of the boundary layer on the scale of freestream vortices and the average shear amplification of low-frequency disturbances in the boundary layer. Experiments and analysis show that the modelling method based on appropriate scale parameters can better describe the fluctuation growth of Klebanoff model in the pre-transitional region. The initial model considers that the increase of laminar kinetic energy is caused by the freestream of energy to the boundary layer due to pressure diffusion. Reference 17 shows that the formation of k_L is due to the interaction of Reynolds stress related to pre-transition, i.e. non-turbulent velocity fluctuation and average shear. In average velocity profiles, changes due to pre-transition fluctuations represent the loss of average kinetic energy, suggesting that a more traditional strain-based production mechanism is appropriate. Recent Large Eddy Simulations of the transition boundary layer [63] seem to confirm that this description of k_L generation is more physically correct than that based on transport.

The theoretical basis of Transition $k-kl-\omega$ model is that the transition process itself is accomplished by energy transfer from laminar kinetic energy k_L to turbulent kinetic energy k_T. Variables k_T are used to characterize the modes of fluctuations to show the characteristics of complete turbulence, such as strong three-dimensional, multi-scale and time-scale, energy spectrum, and significant viscous dissipation. Initialization of the transition process is based on local (single point) flow conditions, and a shear shielding concept is adopted to suppress the non-linear turbulence breakdown mechanism. At the same time, the method of transition initiation considering the time scales of nonlinear disturbance amplification and dissipation correlation is used to predict more accurately the effect of free turbulence length scale on the transition process.

For Reynolds averaging, transition can be understood as an increase of pressure-strain term in the Reynolds stress equation. The fast and slow pressure-strain terms make the fluctuations return to isotropy, and represent the increase of the intensity of the three-dimensional turbulent fluctuations during the transition process, which also correspond to the decrease of the modulus in the higher anisotropic Klebanoff model. In Transition $k-kl-\omega$ model, the pressure-fluctuation term means that the energy changes from laminar kinetic energy to turbulent kinetic energy, that is, from Klebanoff model to high-order three-dimensional turbulence of fully turbulent flow. The total fluctuation energy is composed of

the sum of k_L and k_T, the transformation of energy from one to another can be interpreted as the redistribution of energy rather than the generation or dissipation of energy.

In the model, the shear-sheltering is achieved by suppressing the generation of the source term, while the initial transition includes the transformation between k_L and k_T equations. The model proposes that the ratio of the time scale of turbulence generation to the time scale of molecular diffusion is a dimensionless correlation leading to the onset of transition. Conceptually, when the time scale associated with the dynamics of turbulence generation is short enough compared with the time scale associated with molecular diffusion, entrainment disturbances in the developing boundary layer will undergo non-linear rupture and amplification. Therefore, the initial transition is considered to occur when the time scale ratio reaches to a critical value. Similarly, the viscous sublayer in a turbulent boundary layer inhibits the generation of partial turbulence because the time scale ratio is lower than the critical value of disturbance amplification. At the same time, the perturbation associated with Tollmien–Schlichting wave can be extended to natural transition by assuming that it has a time scale proportional to the eddy viscosity derivative within the pre-transitional boundary layer. Therefore, the natural transition criterion is a function of the ratio of Tollmien–Schlichting wave time scale to molecular diffusion time scale. Finally, these two dimensionless parameters are used to damp the transition-sensitivity of the turbulence generation term in the model equations.

The transport equations of Transition $k-kl-\omega$ model are given as following. They are based on incompressible condition, with ignoring the volume forces. The continuity equation and momentum equation are controlled by steady Reynolds-averaged scheme, while the Reynolds stress term is governed by a linear eddy-viscous model. The three additional transport equations adopted include turbulent kinetic energy k_T, laminar kinetic energy k_L and scale-determining variable ω.

$$\frac{Dk_T}{Dt} = P_{k_T} + R_{BP} + R_{NAT} - \omega k_T - D_T + \frac{\partial}{\partial x_j}\left[\left(\nu + \frac{\alpha_T}{\alpha_k}\right)\frac{\partial k_T}{\partial x_j}\right] \tag{3.33}$$

$$\frac{Dk_L}{Dt} = P_{k_L} - R_{BP} - R_{NAT} - D_L + \frac{\partial}{\partial x_j}\left[\nu\frac{\partial k_L}{\partial x_j}\right] \tag{3.34}$$

$$\begin{aligned}\frac{D\omega}{Dt} = C_{\omega 1}\frac{\omega}{k_T}P_{k_T} + \left(\frac{C_{\omega R}}{f_w}\right)\frac{\omega}{k_T}(R_{BP} + R_{NAT}) - C_{\omega 2}\omega^2 \\ + C_{\omega 3}f_\omega \alpha_T f_w^2\frac{\sqrt{k_T}}{d^3} + \frac{\partial}{\partial x_j}\left[\left(\nu + \frac{\alpha_T}{\alpha_k}\right)\frac{\partial \omega}{\partial x_j}\right]\end{aligned} \tag{3.35}$$

The different terms in the model equations represent production, destruction and transport mechanism, respectively. Previously, it has been shown that this form improves the accuracy in the transition region [67]. In the ω equation, the fully turbulent production, destruction, and gradient transport terms (first, third, and fifth terms on the right-hand side of equation (3.35) are analogous to the similar terms in the k_T and k_L equations and are similar to terms that appear in other $k-\omega$ model forms [34]. The effect of the transition source term (the second term on the right side) is to reduce the turbulence scale in the transition breakdown process. Similar terms are also included in ε equation of initial model. The fourth term on the right side of the equation is introduced to reduce the length scale of the watershed outside the turbulent boundary layer, which is necessary for accurate prediction in the wake region of boundary layer.

By definition, the total kinetic energy in the fluctuation is the sum of turbulent kinetic energy and laminar kinetic energy, that is

$$k_{TOT} = k_T + k_L$$

The source terms P_{k_L} and P_{k_T} in the equation are functions of sufficient small-scale kinetic energy.

The anisotropic (near-wall) dissipation terms for k_T and k_L take a common form.

$$D_T = 2\nu \frac{\partial\sqrt{k_T}}{\partial x_j}\frac{\partial\sqrt{k_T}}{\partial x_j}$$

$$D_L = 2\nu \frac{\partial\sqrt{k_L}}{\partial x_j}\frac{\partial\sqrt{k_L}}{\partial x_j}$$

The effective diffusion factor α_T contained in the turbulent transport terms of equations k_T and ω is a function of the small-scale turbulent energy. The source term of the boundary layer (which tends to generate appropriate behavior in the wake region of the boundary layer) contains the f_ω of the kinetic energy damping function. In addition, the other terms in the transport equation are related to the laminar-turbulent transition mechanism in the model. As mentioned before, transition occurs as a transfer of energy from k_L to k_T, with a concurrent reduction in turbulence length scale from the freestream value to the value found in an equilibrium turbulent boundary layer. The model terms R_{BP} and R_{NAT} appear with opposite signs in the k_T and k_L equations, representing bypass and natural transition respectively. Specific definitions and correlations of the equations, as well as the specific values of the coefficients used, can be referred to **Appendix B**.

3.4 Unsteady RANS (URANS) Simulation

Turbulent flow in complex geometries often exhibit oscillatory behavior of large-scale coherent structures, even with stable boundary conditions. Recently, a lot of efforts have been made to solve these oscillation problems from the point of view of numerical simulation. However, for these complex flow problems, LES methods often need to invest more in time and memory cost. Therefore, the Unsteady RANS (URANS) method has become an attractive alternative, especially when numerical simulation is used as an optimization tool [68].

URANS are only applicable to non-stationary flows such as periodic or quasi-periodic flows involving deterministic structures (for example, they can occasionally predict vortex shedding i.e. largest unsteady scales) and falls most often short of capturing the remaining large scales. This is because they still solve for the mean flow equations but in addition perform ensemble averaging (i.e. realizations of the mean flow over many instances).

For time-periodic flows, the numerical simulation of URANS must be averaged over a period to compare with time-averaged data. The computational cost and the resolution requirements are mainly related to the vortical flow structures shed by the geometry and wall layers. Although the URANS has a time-dependent and large eddy structure, it is not a simulation of turbulence, but a simulation of its statistical characteristics. In this kind of flow, turbulence model plays an important role in establishing and correctly predicting complex flow behavior [69].

Large eddy simulation (LES) differs from URANS: LES uses spatial averaging rather than generalized statistical averaging. The average scale is sufficient to filter out small vortices,

rather than being solved by a specific grid, but the randomness of the turbulence solution is preserved to the full Navier-Stokes. Therefore, Reynolds-averaged statistics must be evaluated by accumulating enough samples. In the time-periodic flow, in order to obtain the velocity statistics of the turbulent part, samples must be in a fixed phase.

URANS and LES require different meshes and time steps. LES solves the turbulent vortices themselves, while URANS simulates the turbulence and solves the average structure of the flow. Therefore, LES requires higher spatial and temporal accuracy and higher computational costs. It also requires longer computational time to build statistical averaged solutions. On the other hand, URANS usually requires only a few shedding cycles to converge its finite computation.

The URANS equations are obtained by the following procedure. The Navier-Stokes equations for incompressible flow are time-filtered

$$\frac{\partial \overline{u_i}}{\partial t} + \frac{\partial \left(\overline{u_i u_j}\right)}{\partial x_j} = -\frac{1}{\rho}\frac{\partial \bar{P}}{\partial x_i} + \nu\left(\frac{\partial^2 \overline{u_i}}{\partial x_k^2}\right) \tag{3.36}$$

Then the turbulent stress tensor is introduced, which gives the final URANS equations

$$\frac{\partial \overline{u_i}}{\partial t} + \frac{\partial \left(\overline{u_j}\,\overline{u_i}\right)}{\partial x_j} = -\frac{1}{\rho}\frac{\partial \bar{P}}{\partial x_i} + \frac{\partial \tau_{ij}}{\partial x_j} + \nu\left(\frac{\partial^2 \overline{u_i}}{\partial x_k^2}\right) \tag{3.37}$$

Another difference with steady state configurations is that transient systems are modeled using a time stepping procedure. Starting with an initial condition at time $t = t_0$, the solution algorithm marches forward and finds a solution at time $t_1 = t_0 + \Delta t_1$. The solution found is the initial condition for the next time step and is used to obtain the solution at time $t_2 = t_0 + \Delta t_2$. The process is repeated until the required time is reached [70]. In Chapter 5, both the selection of unsteady calculation time step and sampling frequency, together with the analysis of corresponding calculation results will be introduced in detail.

3.5 Summary

In this chapter, the numerical simulation methods used are introduced, including the governing equations for two-dimensional incompressible plate boundary layer flow and the turbulence models for laminar-turbulent transition process. Also, the motivation and the basic fundamentals of URANS are introduced.

Chapter 4

Experimental Research of LSB

4.1 Introduction

With the development of modern testing technology, it provides technical support for people to understand the details of flow field by means of experimental investigation. In order to reveal the flow mechanism, the static and dynamic characteristics of the separated bubble in the plate laminar boundary layer are studied in the present work, with the combining of various test methods. Among them, the single sensor Hot-Wire (HW) allows high accuracy for the evaluation of the boundary layer integral parameters, thus characterize in detail the statistical properties of the transition and explore self-similarity characteristics. While Time Resolved Particle Image Velocimetry (TR-PIV) and Laser Doppler Velocimetry (LDV) data have been acquired to provide the boundary layer evolution, as well as the freestream properties in terms of mean velocity and fluctuating velocity components. To obtain more reasonable post-processing data, the Proper Orthogonal Decomposition (POD) method is applied [71].

By means of TR-PIV and LDV testing technologies, researchers made deeper insights into boundary layer to understand the main dynamics driving the unsteady behavior of separated flows in the past decades. Simoni et al. [72], Marxen and Henningson [73] et al. carried out relevant experimental and numerical simulation studies, and the results show that the shear layer is unstable due to a Kelvin-Helmholtz (K-H) process, leading to rollup vortices. Particularly, after the separation of the flow, the separated shear layer induced by the inviscid K-H instability process amplify the fluctuations of the velocity. Once the separation bubble reaches the position of the maximum value of the displacement, the saturation of the fluctuations also occurs. Then, the large scale vortical structures shed by the bubble initiate transition, the mixing process is strengthened by both coherent and small-scale structures, contributing to the boundary layer reattachment (if any). While the dynamic behavior of laminar separation bubbles has been intensively studied, the effects of flow parameters on separation flow process and its mechanism still need to be further understood.

By using different methods including the amplification of the velocity fluctuations, the response of laminar separation bubbles to external disturbances, the span wise growth rate and wall-normal amplitude of different modes, a large number of research works have been carrying out. For the problem of the amplification of the velocity fluctuations in the fore part of separated flow, investigations from Marxen et al. [74], Häggmark [75] and Yarusevych et al. [76] show that it is typically well predicted by Linear Stability Theory (LST), which is in good agreement with the experimental results. Dovgal et al. [77] reported the stability characteristics of different mean velocity profiles. The theoretical and experimental research works made by Diwan and Ramesh [78] which focus on the wall distance effects on the most unstable frequency clearly show that, when the distance from the wall is far enough, the wall effects vanish and both maximum amplified frequency and growth rate approach the values predicted for a free-mixing layer. For the problem of the response of laminar separation bubble to external disturbances, experiments are carried out by means of controlling upstream perturbing waves. Among them, the investigations carried out at the Stuttgart University provides one of the most comprehensive view of the influences due to different

parameters of the perturbing waves. Maucher et al. [79] presented the response of a laminar separation bubble to monochromatic waves, which mean simply composed wave trains, at the most unstable frequency with different amplitudes, and pointed out the growth rate and the saturation level of the separation bubble is poorly affected. That means the main influence factor to the overall bubble size is the initial wave amplitude. Using the Fourier based decomposition method, Marxen et al. and Lang [80] et al. processed the experimental data from PIV and LDV measurements, in order to identify the growth rate in stream-wise and wall-normal amplitude of different modes. The results show that, the attached part of boundary layer is mainly affected by the span-wise wave, since the amplitude of corresponding modes is larger than those standing for the most unstable frequency of the shear layer. Lang et al. [81] also investigated the influence due to the superposition of span-wise wavenumbers, simulating the presence of streaky structures, to the frequency of unstable shear layer. The investigations mentioned above show the overall view about the development of monochromatic waves. In reality, the unstable source is superposed with a multitude of waves with different amplitude, which should further contribute to the understanding of the dynamics driving laminar separation bubbles.

Unlike the in-depth study of the dynamic behavior of the flow separation process, other previous works focused on determining the overall response of the laminar separation bubble without analyzing the dynamics control of the flow stability mechanism and related shedding phenomena. For example, Volino [82] studied the time-averaged structure characteristics of laminar separation bubbles by hot-wire measurements, and found that with the increasing of Reynolds number, the characteristic scale of laminar separation bubble became smaller. Similar results can be found when the freestream turbulence intensity is increased. The study of Yaras [83] shows that for the plate flow with strong adverse pressure gradient, the relationship between the characteristic points of separation can be constructed by formulas, which means that it is possible to predict the overall structure of separation bubble by using Reynolds number, turbulence intensity and integral scale as variables. Other formulas have been constructed and widely used in the field of turbomachinery [6].

In the experimental part of present paper, the previous research results on laminar separation phenomenon are summarized, and the above experimental measurement methods with high spatial and temporal resolution accuracy are used to obtain the detailed characteristics of dynamic and static behavior of boundary layer under different flow conditions (including turbulence intensity, Reynolds number, adverse pressure gradient, etc.). However, a flat plate is installed in a properly designed test section to obtain the corresponding working environment of the low-pressure turbine blade of modern aero-engine. The main advantage of this design is that with the help of simple geometry, the detailed characteristics of the boundary layer flow field can be realized together with the large-scale flow structure observed. Therefore, due to the special design of the test section, it is possible that the main parameters affecting the development of the boundary layer change in a series of numerical ranges related to the actual application of aero-engine.

4.2 Test Section

Fig. 4.1 gives the plane diagram of the test section. The test section consists of two adjustable end-wall and a flat plate installed in the center of the channel. The pressure gradient along the flow direction of the plate is varied by changing opening angle of the end-wall to obtain the desired experimental conditions. Upstream of the test section, the geometric throat position from the leading edge of the plate to the channel is a fixed portion, while the gradually converged area accelerates the flow, and the smooth transition of end-wall allows

the flow loss in the front part to be controlled. The rear part of the upper and the lower end-wall consists with flat section, both of them are adjustable by rotating around their respective central axes. Therefore, the variation of pressure gradient is confined to the middle and rear parts of the plate, while the front acceleration part remains unchanged.

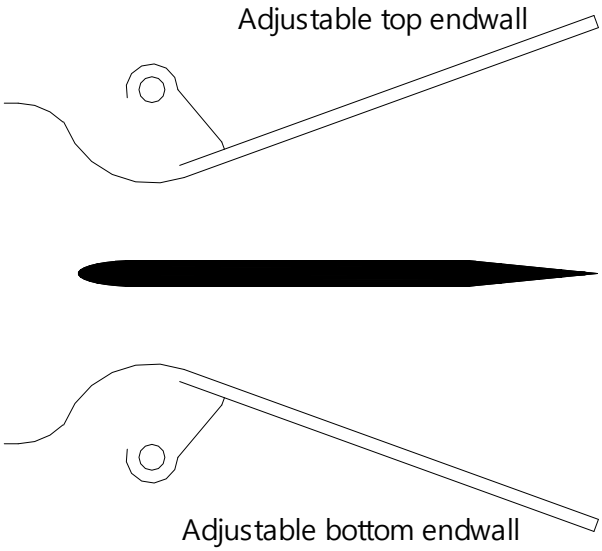

Fig. 4.1 – The layout of test section

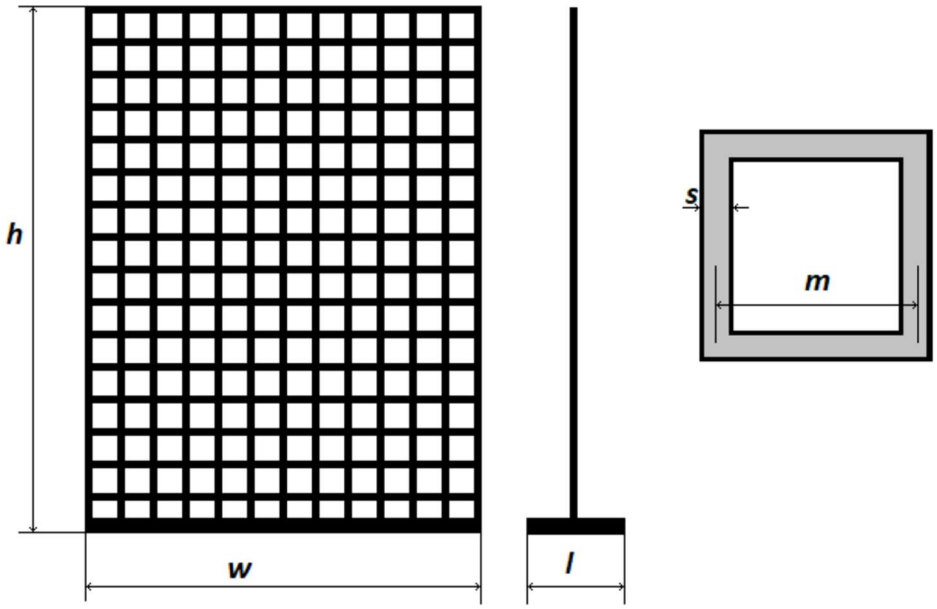

Fig. 4.2 – Scheme of the turbulence generating grids

The leading edge of the plate is a smooth-transition elliptical line, and the length and width of the straight section in the downstream are both 300 mm, so as to ensure the two-dimensional time-averaged flow in the mid-span plane of the blade, and also to improve the maximum spatial resolution. The aspect ratio of the leading-edge ellipsoid is 4:1, which can reduce the uncontrollable wave propagating into the boundary layer caused by the separation of the leading edge, so as to affect the transition process. In addition, the position of the end-wall can be set to a state of asymmetric up and down to control the incidence angle of the leading-edge airflow.

17 pressure measuring points are arranged on the upper and lower surfaces of the plate leading edge in the aims of controlling the appropriate angles required under different conditions, it also guarantees that separation did not occur on the nose of the plate due to flow incidence. 51 pressure measuring points are totally installed along the flow direction on the upper surface of the flat plate section to provide pressure gradient characteristics due to different end-wall settings. The signal from the pressure measuring point is transmitted to the acquisition system for recording data, while the pressure sensor and the acquisition device are connected by a scanning valve to control the orderly transmission of the data signal from the measuring point.

The influence of different integral parameters on flow characteristics should be considered in the experiment. Among them, the change of Reynolds number depends on the power source of wind channel, the adverse pressure gradient is regulated by the end-wall opening angle, and the turbulence intensity of different incoming flows depends on the upstream grid plate. The grid plate has three different mesh scales, which could be inserted the upstream of converge section perpendicular to the flow direction to obtain the required turbulence intensity. A base is provided at the bottom of the grid plate to ensure the air tightness when it is installed in the wind tunnel, which it is tightly combined with the upper and lower surfaces of the wind tunnel to suppress excessive vibration and generate no additional turbulent fluctuations. Fig. 4.2 gives the structural sketch of grid plate. Through laser cutting, rectangular element holes are machined on thin plates with different thickness, and the parameter affecting turbulence intensity is the ratio of width of strip structure between two adjacent cells to the cell area.

4.3 Measurements Setting and Test Matrix

Fig. 4.3 shows the test methods and instrument measurement domain. Measurements are performed with complementary techniques, including pressure testing taps, Laser Doppler Velocimetry (LDV) and Particle Image Velocimetry (PIV). The analysis of the data obtained from the complementary measuring techniques helps us to understand the instability mechanisms involved in the transition/reattachment processes of the separated shear layer in details. The use of high-precision LDV allows investigating reverse flow magnitude and both Reynolds normal and shear stress distributions along the separated flow region, and also guarantees high accuracy determination of the velocity and turbulence evolution in the

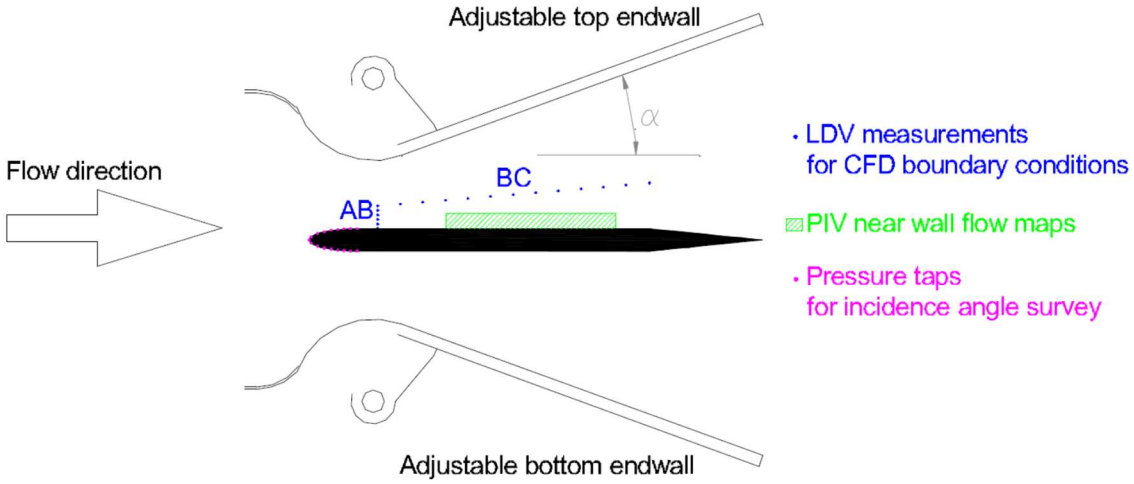

Fig. 4.3 – The layout of testing measurements

freestream both the mean and statistical flow properties along a wall-normal line at the domain inlet, just as line AB and BC. While the amplification process of flow oscillations induced by instability mechanisms can be investigated by high frequency response performance of velocimetry. The instantaneous velocity vector maps given by PIV results complement the flow field analysis, providing information on the generation and evolution of the large-scale coherent structures shed as a consequence of the separated shear layer roll-up. For the average pressure distributions along the plate, it relies on the aforementioned surface pressure measurement points and data acquisition system.

4.3.1 LDV measurements for defining boundary conditions

By means of LDV testing along the AB and BC lines, the boundary conditions are acquired. The AB line is perpendicular to the upper plate surface at x/L=0.19 and covers different wall normal positions (from y/L=0 to y/L=0.033), while the BC line is inclined and extends from x/L=0.190, y/L=0.033 up to the end of the plate x/L=1, y/L=0.133. Totally 29 measuring points are adopted on the AB line with the first one at a distance of 50 μm from plate. In order to provide accurate freestream and turbulence characterization near the wall, a measuring point spacing of 50 μm is adopted up to 1 mm from the wall. In the streamwise direction, totally 13 equally spaced points are sampled on the BC line. The fixed acquisition period is taken as 120 s to ensure statistical convergence of the data for each measuring point. The data sampling rate is 5kHz away from the wall, but with the decrease of the wall distance, the sampling rate decreases sharply due to the reflection effect. Measurements are carried out in coincidence mode, thus allowing also the evaluation of the Reynolds shear stress on both these lines. The free-stream turbulence is measured at the point x/L=0.2 and y/L=0.033 by means of LDV instrumentation with an average acquisition frequency of about 10 kHz. It is estimated by computing the fluctuations over an acquisition period of 120 seconds which resulting in an overall number of samples equal to about 550000.

4.3.2 Field measurements by TR-PIV in the time varying boundary layer

By means of a Dantec TR-PIV system the boundary layer developing along the rear part of the plate is surveyed. The measuring domain ranges from x/L=0.27 to x/L=0.81 and with a height of about y/L=0.04. For each testing cases, eight independent sets of 2000 instantaneous velocity fields are acquired by a sampling rate of 2 kHz. Therefore, statistical quantities of the BL are computed processing from 16000 PIV snapshots. The instrumentation adopted is constituted by a dual-cavity Nd: YLF pulsed laser Litron LDY 300 (energy 30 mJ per pulse at 1000 Hz repetition rate, 527 nm wavelength). While the optical system forms a light sheet of 1 mm thickness. The light is scattered by Vaseline oil droplets with an average diameter of 1.5 μm and it is recorded on a highly sensitive Speed-Sense M340 digital camera with a cooled 2560×1600 pixels CMOS matrix. For the present experiment, the magnification factor is set to 0.16, thus providing a particle image diameter of the order of 3 pixels, with a seeding concentration of around 4-5 particles per investigation sub-area. With an interrogation area of 16 by 16 pixels and 50% overlap method, the adaptive cross-correlation algorithm is used, which results in a vector spacing of around 0.5 mm. A peak validation is also adopted to discriminate between valid and invalid vectors. The Gaussian fitting procedure guarantees a sub-pixel recognition accuracy of particle displacement of the order of 0.1 pixel by such kind of setting. Considering the spatial resolution of the present experiments and the strong parameter gradient near the plate surface, the mean particle displacement variation per interrogation region height is found to be

between 6 and 9%. Based on the PIV setting, the relative error for the evaluation of the instantaneous velocity in the freestream region is expected to be not more than 3.0%. However, it enlarges to 6.0% in the regions where time-mean velocity reduces to one half of its freestream value. Due to the spatial resolution of the experiments, the BL thickness is resolved at separation with 8 measuring points for the reference case, while the BL close to the bubble maximum displacement is resolved with 16 measuring points for the same condition. As the increasing of Re, the BL at separation is resolved with about 6 and 5 measuring points.

4.3.3 Main overall influence parameters

The influences of three types of flow integral parameters to the flow mechanism of LSB are considered systematically in experiments. The adverse pressure gradient environment is realized by adjusting the upper and lower end-wall of the test section. The quantized data is the angle between the straight end-wall section and the horizontal plane. During experiments, the opening angle ranges from 0° to 12°. The equal end-wall angle of both upper and lower corresponds to the state of 0 incidence of airflow, which means a flat plate like condition (zero pressure gradient) has also been tested. The Reynolds number reference point is the length of the plate, while reference velocity is that of freestream, and the assessment range is 70000~500000, corresponding to the typical low Reynolds number working environment of turbomachinery. The turbulence intensity of incoming flows ranges from 0.65% to 5%, representing different turbulence types of freestream. During the experiment, these three parameters are combined to obtain different states, but the value range of time-averaged flow field and instantaneous flow field is different, which would be specified in combination with the subsequent numerical simulation. The experiments provide several parameters, including the detailed results of plate pressure coefficient, boundary layer velocity and turbulence profiles. These quantities are also studied and validated by numerical simulations from the perspectives of time-averaged and unsteady state.

4.4 Phenomenological Analysis of Transition Mechanisms

According to the above experimental conditions, a systematic experimental research was carried out. Then the influences of the integral parameters on the time-averaged and dynamic flow field of laminar separation bubble are obtained, including the level of adverse pressure gradient, turbulence intensity, Reynolds number etc. In this section, time-averaged and instantaneous flow field results of plate laminar flow separation bubbles under specific working conditions are both briefly introduced as the basis for the comparison of subsequent numerical simulation results.

4.4.1 Time-averaged flow field

Fig. 4.4 shows the distribution of velocity component u/U_0 of flow field and velocity fluctuation u_{rms}/U_0 under typical condition. The result takes the end-wall opening angle $\alpha = 12°$, the Reynolds number $Re = 150000$, and the turbulence intensity $Tu = 1.5\%$ as the reference condition, which is equivalent to typical working environment when a separation occurs in low pressure turbine. Coordinate (x, y) in both directions that normal to the wall and stream-wise are normalized by the length of the plate L, while the component u is normalized by the testing domain inlet velocity U_0. The two sub-figures highlight the characteristics of boundary layer flow separation: at x/L=0.37, it starts to detach from the

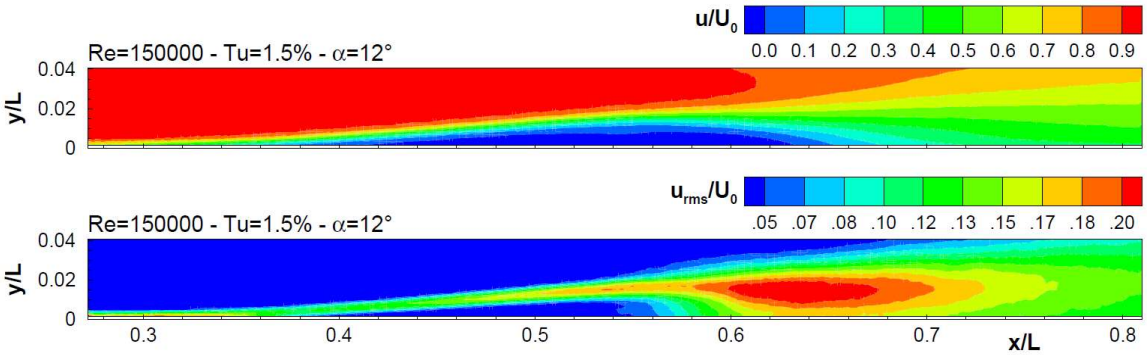

Fig. 4.4 – Velocity and velocity rms contour plots for the typical case.

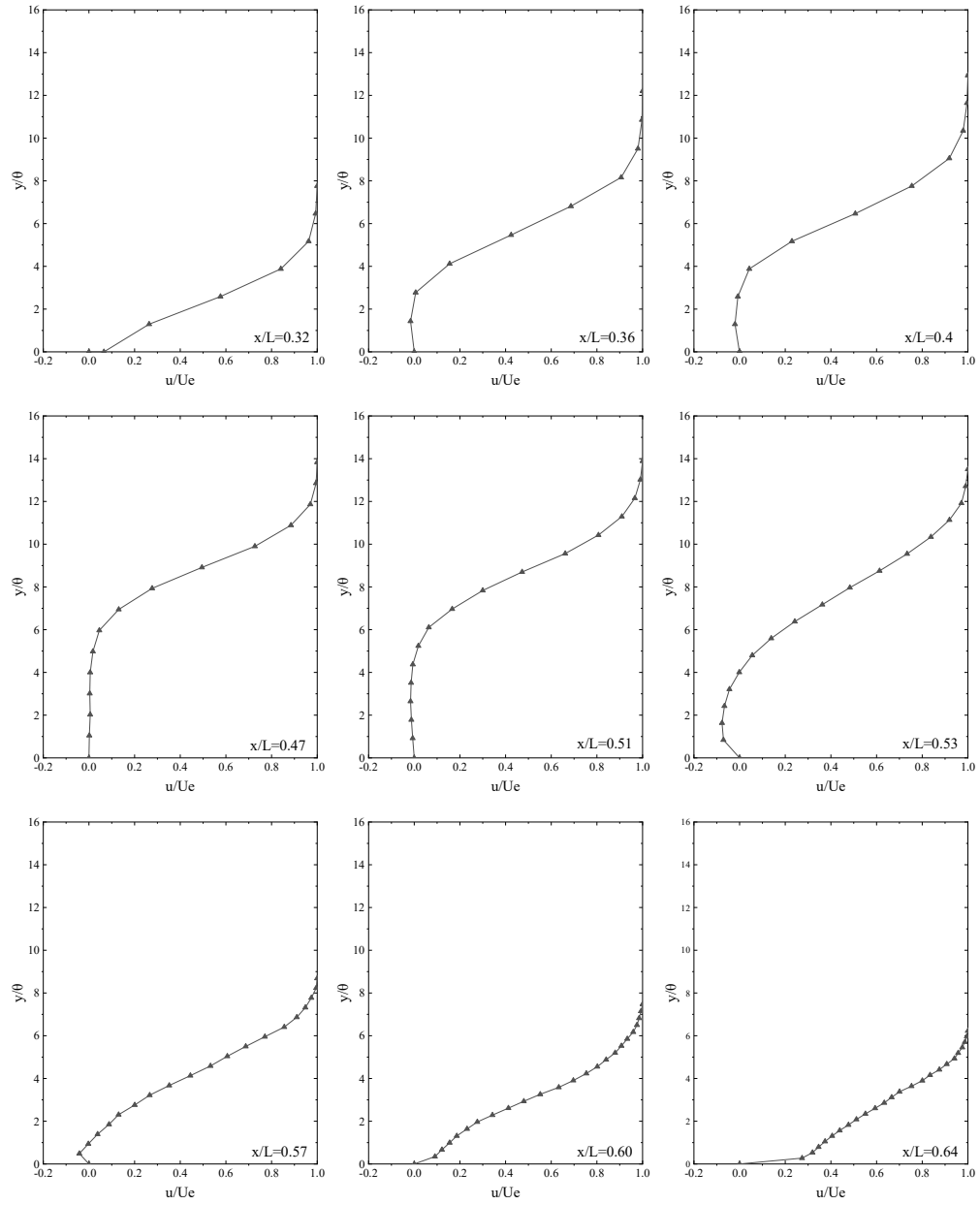

Fig. 4.5 – Velocity profiles in normal direction for the case Re=150000 Tu=1.5%

surface of the plate, and the reverse velocity starts to appear in the near surface area, that is, the beginning of separation. Subsequently, along with the forward flow, the region of the reverse velocity gradually increases, also the boundary layer thickness obviously amplifies. At the position where x/L=0.56, the boundary layer thickness reaches the maximum value. At the same time, with the transition progress, under the influence of disturbance, the reverse flow area gradually decreases, and the separated flow re-attaches to the wall surface again at the approximate position x/L=0.65. Therefore, an obvious laminar separation bubble is formed. According to [84] and [85], a convective inviscid instability process is expected to drive the amplification of disturbances along the separated shear layer, due to the reverse flow magnitude is smaller. It can be seen from the comparison that the larger value of u_{rms}/U_0 appears in the shear layer, which the front part is concentrated with the transition velocity profiles, while the downstream part of the separation is more concentrated with the higher values. This region lags behind the position of the maximum displacement thickness of the separation bubble. This behavior is consistent with previous literature results (see [86] for example). Moreover, a further peak can be observed in the wall region in the rear part of the separated shear layer (downstream of x/L=0.63), as also observed in [87].

$$Cp = \frac{P_{in}^* - P}{P_{in}^* - P_{out}} \tag{4.1}$$

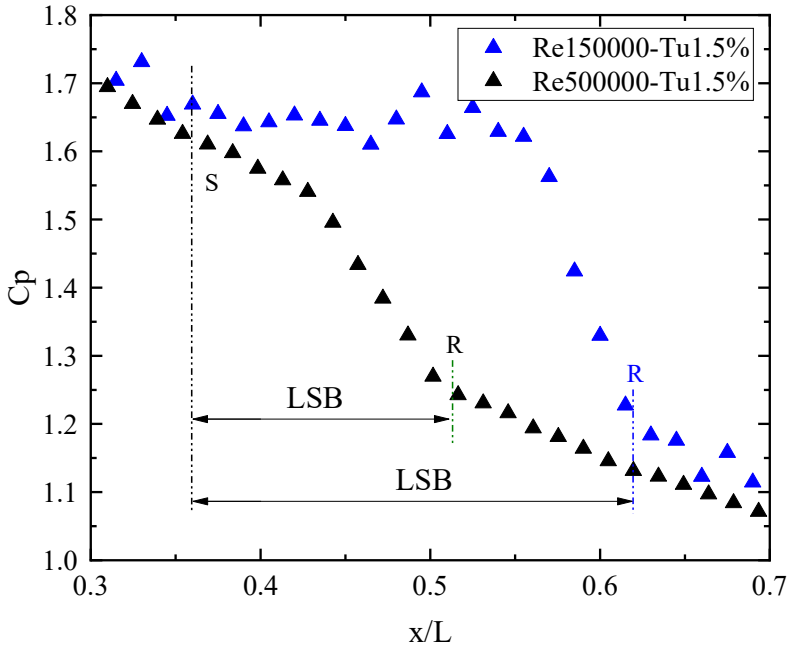

Fig. 4.6 – Pressure coefficient distribution for typical cases

Several typical sections that normal to the wall and along the plate are selected in the region of time-averaged flow field of LSB. Then the time-averaged velocity component u on each section can be normalized, hence the velocity profile distributions as shown in Fig. 4.5 are obtained. It should be noted that U_e is the local mainstream velocity of the outer boundary layer, while the distance along the vertical direction of the wall uses the momentum thickness θ for dimensionless treatment. These characteristic sections cover the main area of laminar separation bubbles, and the behavior of velocity profile varies with different sections. At the

upstream of the detachment position, the velocity profile maintains as a stable laminar flow state with no obvious change, and the value of the velocity profile gradually increases from 0 on the wall surface, showing the characteristics of the viscous sublayer. From the separation location (x/L=0.37), the value of velocity profile decreases from 0 to the negative direction. After reaching a certain value, it gradually increases to the positive range again, that is, the reverse flow velocity appears in the bottom area. With the progressive flow, the negative region of velocity profile increases gradually, which corresponds to the increase of LSB thickness. Consistent with the velocity distribution figure, the section of velocity profile with the widest range of negative value locates just at the position of the maximum displacement thickness (x/L=0.56), where after that, a shrinking trend occurs in the range of normal direction which has a reverse velocity vector. Moreover, the progress of reattachment is faster than that of detachment, accompany with higher velocity magnitude value in the reverse flow region, which indicates a rapid reattachment trend of LSB. After reattachment of LSB, a typical turbulent flow behavior is shown in the velocity profiles.

As a main parameter of time-averaged flow, surface pressure distribution can quickly give the characteristics of flow field and judge the whole behavior of LSB. Fig. 4.6 shows the experimental results of pressure coefficient (definition in equation 4.1) distribution on the surface of the plate under typical conditions. It is observed that when the flow separates, the surface pressure coefficient evolves from an approximate linear reduction process to a relatively stable or slow development one. Near the position of maximum displacement thickness, it starts to decrease suddenly and rapidly until the reattachment point is reached. Also, the slope of the curve returns to the state like before flow separates. Therefore, the behavior of LSB can be easily judged and analyzed according to the distribution of surface pressure coefficients.

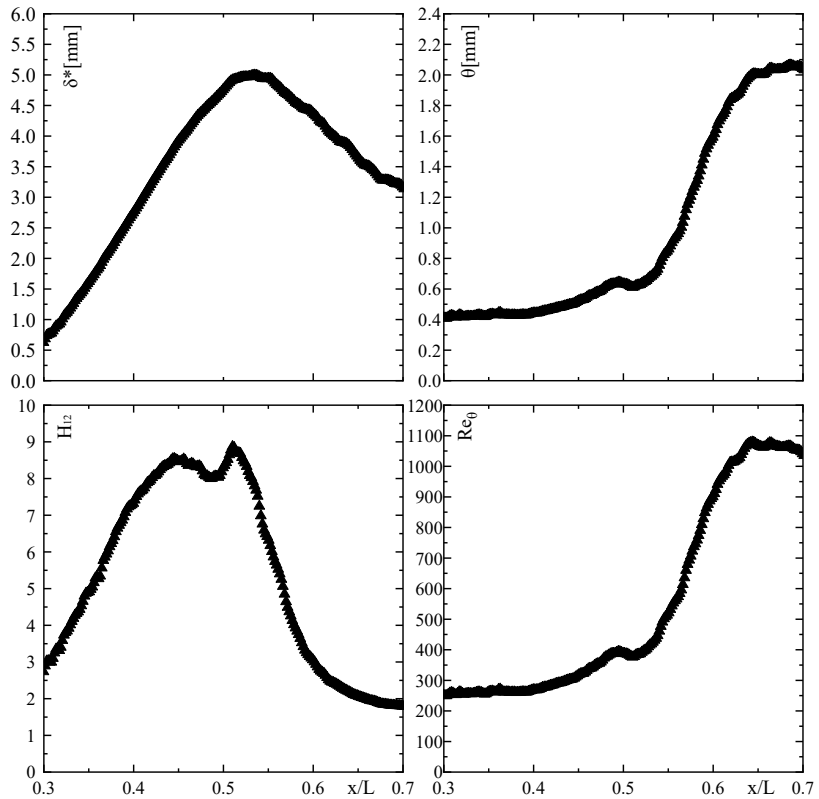

Fig. 4.7 – Experimental integral parameters in typical case (Re=150000, Tu=1.5%)

Fig. 4.7 illustrates the boundary layer integral parameters obtained in the typical condition tested (Re=150000, Tu=1.5%). All integral parameters are plotted with respect to the normalized stream-wise coordinate in order to detect the characteristic positions of the LSB. In the diagram of displacement thickness, the location of the bubble maximum thickness can be detected, while the peak in the H_{12} distribution is usually related to the transition onset. Moreover, the distribution of the momentum thickness allows the computation of the Reynolds number based on the momentum thickness at separation $Re_{\theta s}$, which usually appears in the experimental correlations available in literature for the characterization of the separated flows transition in turbomachinery applications [11]. The detailed comparison will be discussed in the next chapter together with the simulation results.

4.4.2 The dynamics performance of LSB

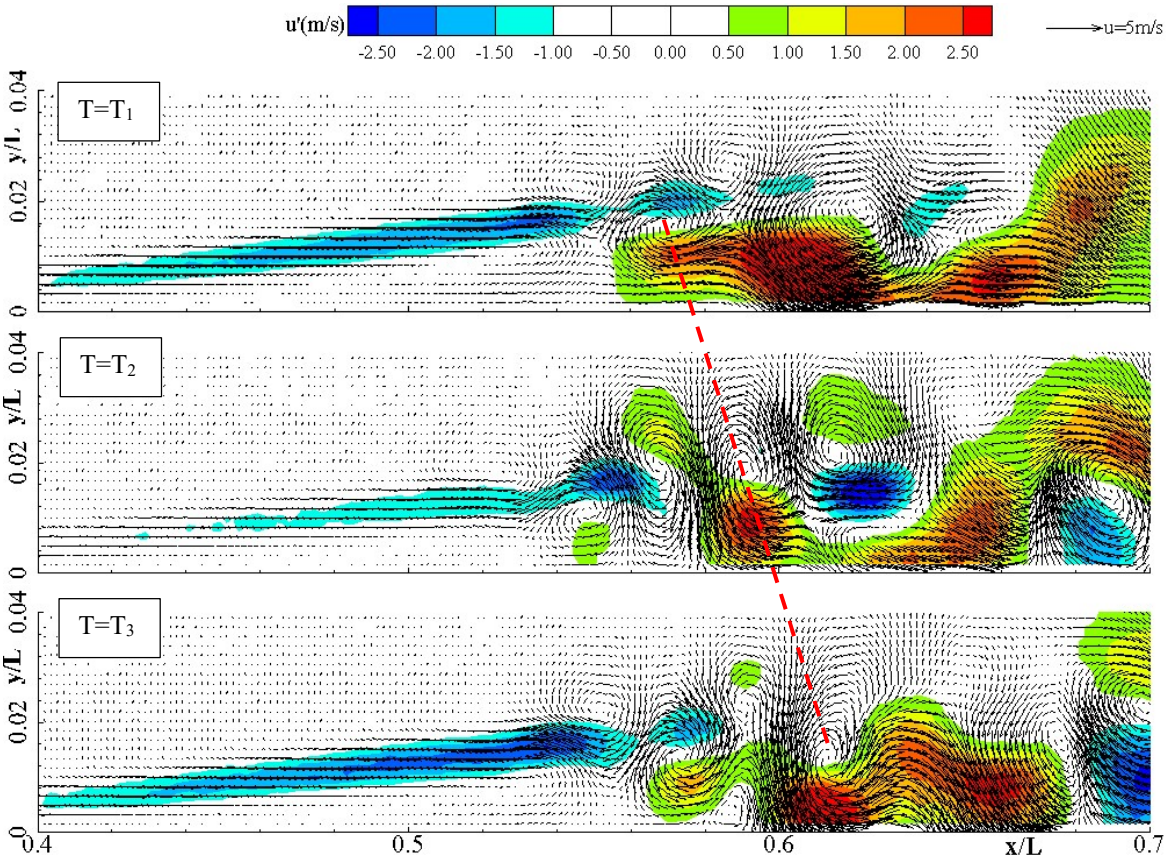

Fig. 4.8 – Instantaneous perturbation velocity vector fields (u', v') Re=150000 Tu=1.5%

Based on the time-averaged simulation, the further study of transient flow field is carried out, which enables people to understand the mechanism of laminar flow separation from the perspective of dynamics. With the combination of TR-PIV testing measurement and POD data processing, the study of transient flow field during laminar flow separation is realized. Fig. 4.8 shows the fluctuation vector distribution under typical condition. The opening angle of end-wall adapts D12-7, the Reynolds number is 150000, and the turbulence intensity takes 1.5% as reference condition. Each sub-figure corresponds to the perturbation vector distribution with vortex structure characteristics at different time within a single shedding period. Large scale vortical structures are shed near the time-mean bubble maximum

displacement position. In order to facilitate analysis, one of the typical vortex structure centers is wired over time to estimate their propagation speed. Hence the group velocity of the wave packet induces the formation of the K-H rolls. The experimental work investigated by Matteo et al. includes the influence of integral parameter variations on the vortex shedding process, such as the Reynolds number and turbulence intensity of the freestream, and how the vortex shedding is restricted. The velocity of the vortex is obtained by analyzing the wavelength and frequency of the shed vortex, then the dimensionless shedding wave number parameter, involved in the temporal formulation of the stability equations (see [72] and [88] for example), are computed. Finally, it is found that the shear layer thickness at the separation point is the main factor that has a decisive effect on shedding vortex. The superimposed color contour highlights the distribution range of the maximum and minimum values of the fluctuating velocity in the flow-stream direction. It is shown in the figure that the extreme value of the reverse velocity fluctuation is easy to appear at the intersection of the separated shear layer and the adjacent two vortex structures, while the extreme value of the forward velocity fluctuation is more likely to appear at the downstream of the reattachment position near the wall.

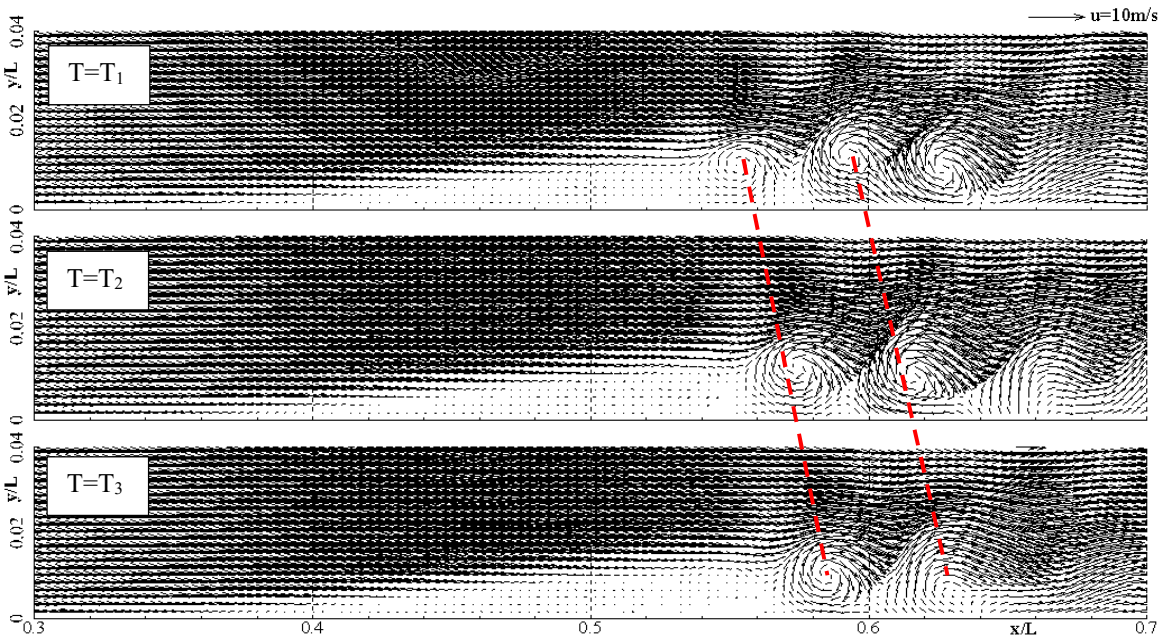

Fig. 4.9 – Instantaneous velocity vector fields (u, v) Re=150000 Tu=1.5%

The velocity vector distribution in Fig. 4.9 is the result of superimposing the statistical averaged value on the basis of the instantaneous fluctuating velocity, which highlights the generation and downstream propagation of the large structure of reverse flow. The structure of these shedding vortices is larger than that of the fluctuating velocity vector, and the position of producing shedding vortices is consistent with the initial position of disturbing velocity vector vortices. It is also found that the reverse velocity magnitude in the laminar separation bubble is much smaller than that in the outer main flow. At the same time, the initial position of the core of the shedding vortex in both two groups of velocity vector distribution is about x/L=0.56, which is the corresponding position of the maximum boundary layer thickness in the time-averaged flow field. The K-H instability is prior to this

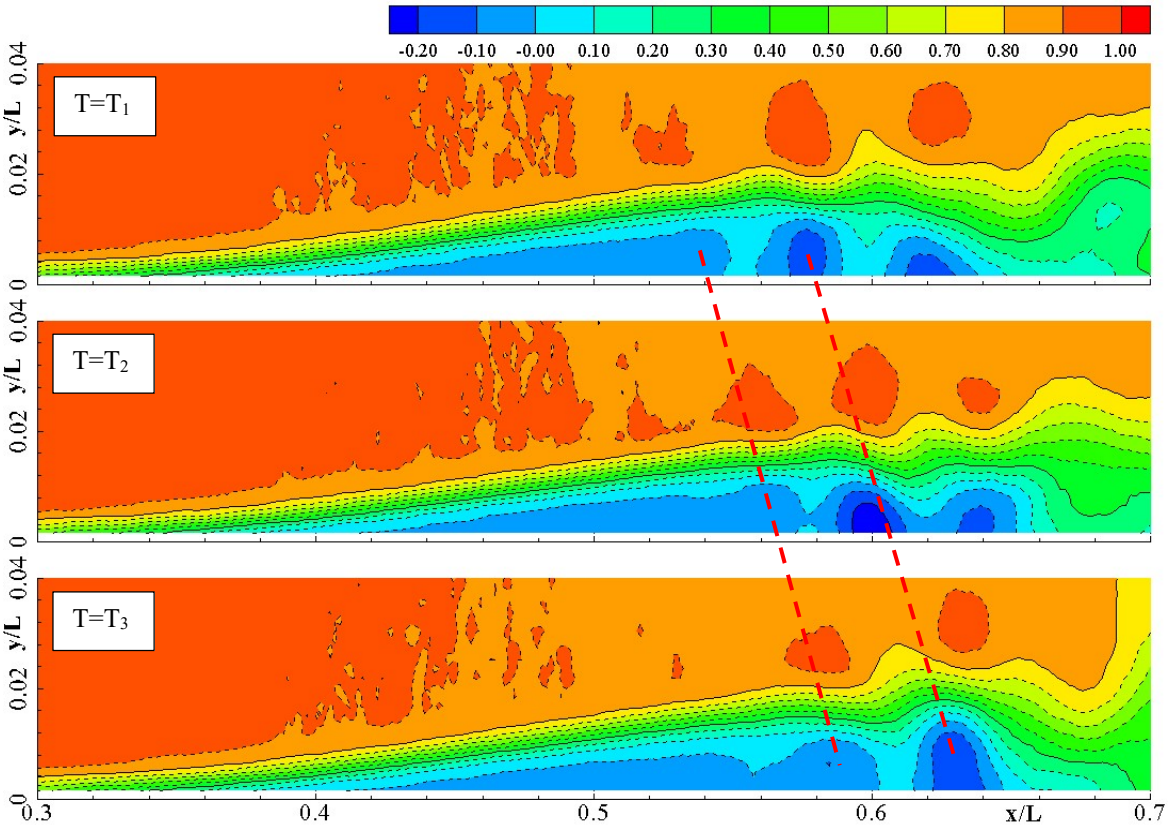

Fig. 4.10 – Instantaneous normalized velocity (u/U_0) distribution Re=150000 Tu=1.5%

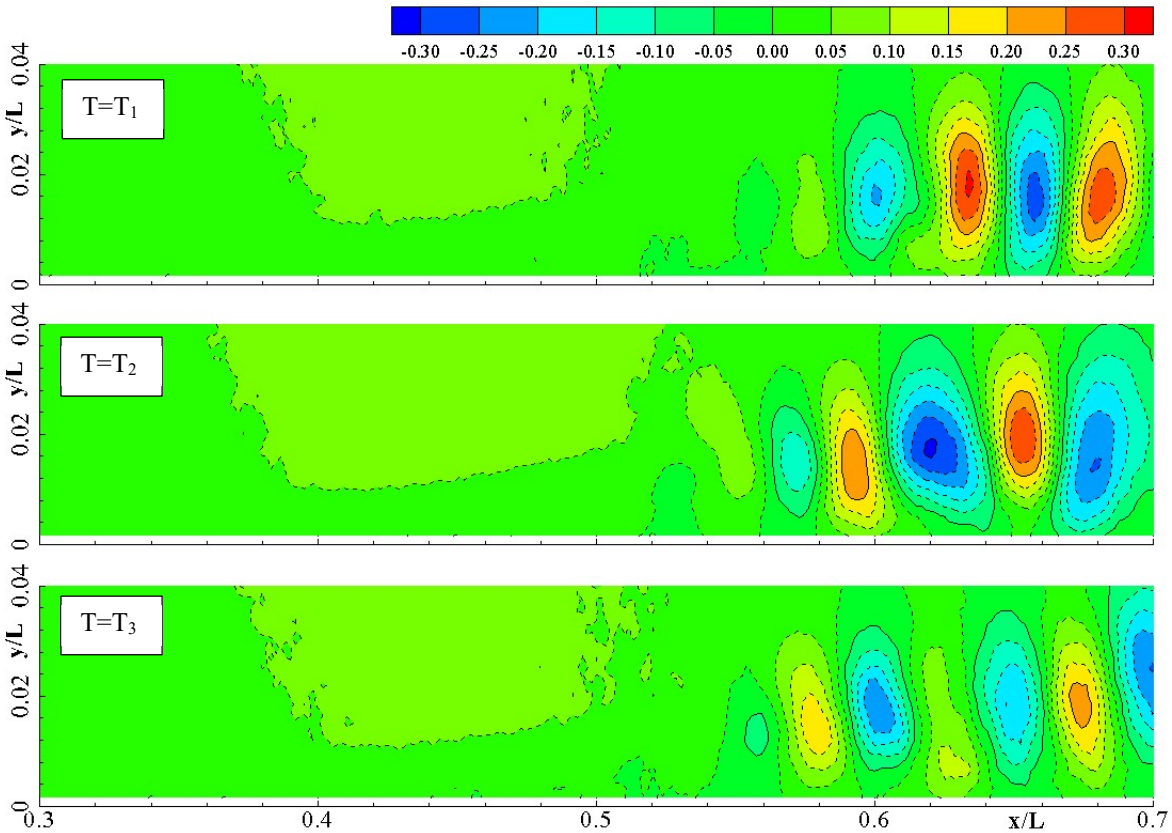

Fig. 4.11 – Instantaneous normalized velocity (v/U_0) distribution Re=150000 Tu=1.5%

location, which further shows that the initial transition of the laminar separation bubble is prior to the maximum thickness.

Fig. 4.10 and Fig. 4.11 respectively correspond to the progressive distribution of normalized instantaneous velocity components u/U_0 and v/U_0 with time. In the dimensionless velocity distribution Fig. 4.10 of the flow direction, it can be seen that the shear layer divides the flow into relatively closed low velocity region and high velocity main flow region. In the low velocity circumfluence area near the wall, the concentration area of the maximum reverse velocity begins to appear at the position a little upstream of the maximum thickness. This core area moves to the downstream periodically. With the help of the central line, the movement law can be easily obtained. Each low-speed core region corresponds to a positive velocity core concentration region, and moves synchronously to the downstream, which corresponds to the characteristics of the shedding vortex structure. To observe the dimensionless velocity distribution Fig. 4.11 in the y direction, the most obvious feature of which is the maximum and minimum concentration areas that appear from the beginning of the shedding vortex, they alternate and move to the downstream in order. As described in [72,73], the directional motion of the y-direction velocity nucleus is an obvious sign of K-H shedding vortex.

4.5 Summary

This chapter mainly introduces the contents of experimental research, including the overall layout of the experimental platform, the experimental data testing system, the accuracy and uncertainty of testing instruments, the experimental matrix and the parameter range. The overall behavior of the time-averaged flow field and the dynamic characteristics of the transient flow field under the typical conditions of the laminar separation bubble (D12-7, Re = 150000, Tu = 1.5%) are analyzed. These results are the references of the following numerical simulation.

Chapter 5

Numerical Investigation of LSB

5.1 Introduction

The numerical work consists on carrying out a systematic analysis, both with Reynolds Average Navier-Stokes (RANS) and Unsteady Reynolds Average Navier-Stokes (URANS) simulations. The results of the numerical simulations are critically investigated and compared with the experimental ones in order to understand the effect of the main physical parameters on the LSB behavior. For RANS simulations, different turbulence and transition models are compared at first to identify the adaptability to the flow phenomena; then, the influence of the three parameters (Reynolds number, freestream turbulence intensity and end-wall opening angle, which determines the adverse pressure gradient intensity) on the LSB behavior, is investigated with a simulation matrix. Boundary layer integral parameters are discussed for the different cases in order to understand the flow phenomena in terms of flow time-mean properties. For URANS simulations, the analysis focuses on the surveys of the instantaneous velocity vector maps which highlight the dynamics of the large-scale vortex structures shedding from the bubble maximum displacement position. By quantifying the frequency and period of shedding vortices, to analyze the dynamic influence factor to the K-H instability progress.

5.2 Computational Domain and Mesh Independency

The experimental test section is modelled in order to carry out several numerical simulations. In the test section of computational domain, two adjustable end-wall are provided both at the top and bottom of the plate, that induces two convergent dilation channels formed among them. By adjusting the angle of the end-wall to obtain different adverse pressure gradients needed, hence the air flow angle of attack controlling is available, which means different experimental conditions corresponding. In the modeling process, the flow domain is treated as a two-dimensional plane according to the test system settings, which also coincides with the experimental situation. The computational domain consists of proper extensions both upstream and downstream of the flat plate region, especially for the downstream of the flat plate. One of the computational domains with end-wall opening angle adopting 12 degree and 7 degree for the upper and bottom one respectively, is shown in Fig. 5.1. In the following text, an abbreviation form with “D12-7” will be taken for simplicity. The same expression will be used for “D7-2.5” for another typical adverse pressure gradient condition.

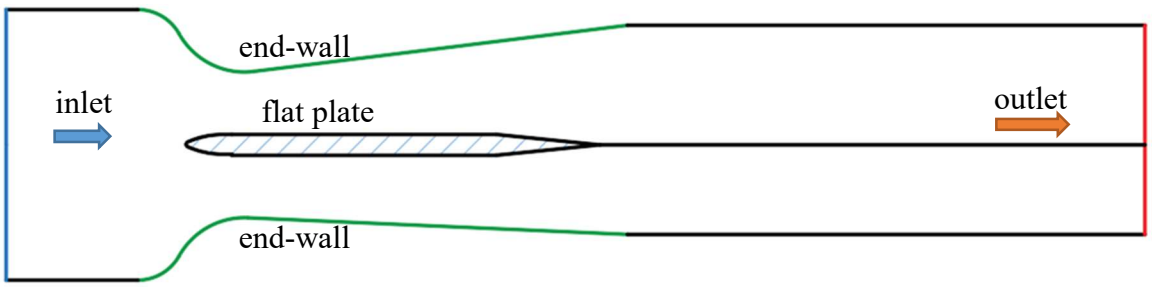

Fig. 5.1 – Computational domain for D12-7 case

For the mesh generation, Numeca IGG [89] is employed in order to construct a structured mesh. Considering that the computational domain structure has typical characteristics of external flow field case, a C-type topology is adopted. In additional point, as mentioned in section 2.2.3, the boundary layer flow, especially for the LSB, is a typical sublayer phenomenon near to the wall together with relative low Reynolds number. In such condition, not only a suitable turbulence model (discussed in Chapter 3) is necessary, but also a reasonable y^+ value, the non-dimensional wall coordinate, is needed to be well chosen. However, the latter is directly connected with the first layer in the near wall region or the first cell center during mesh generation. For the LSB problem, the height of the first cell near the solid walls should be chosen close to one (obviously for the higher simulated Reynolds number) and the viscous layer is generated with appropriate growth rate ensure to capture of boundary layer characteristics. In the viscous sublayer (where $y^+ < 5$), the fluid is dominated by the viscous effect, so it can be assumed that the Reynolds shear stress is negligible. The "linear velocity law" is given by:

$$u^+ = y^+ \tag{5.1}$$

Where the expressions of u^+ and y^+ are

$$u^+ = \frac{u}{\sqrt{\frac{\tau_w}{\rho}}} \tag{5.2}$$

$$y^+ = y\frac{1}{\nu}\sqrt{\frac{\tau_w}{\rho}} \tag{5.3}$$

Then we have

$$y = \frac{y^+\nu}{\frac{\tau_w}{\rho}} \tag{5.4}$$

For a quick estimation, by taken reference freestream velocity u_∞ and boundary layer length, together with a desired $y^+ \sim 1$, the first cell center value y is decided. A reasonable first cell near the wall and the growth rate example is given in Fig. 5.2.

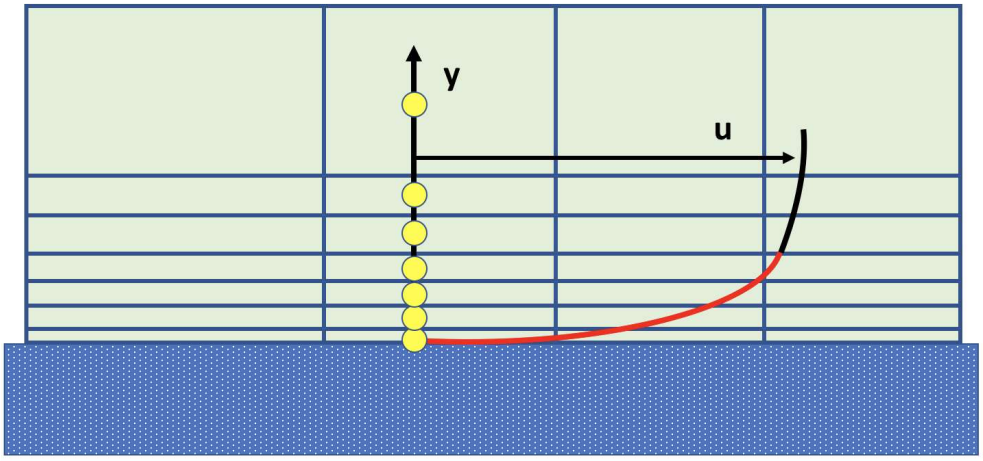

Fig. 5.2 – Viscous sublayer resolving approach to resolve boundary layer (in red)

Based on the above principles, three computational grids with different number of elements are generated in order to evaluate the solution's grid dependency. The value of mass flow rate is employed as the test variable parameter and the results are reported in Tab. 5.1. The comparison shows that no appreciable differences are reported for mesh 2 and mesh 3, hence the intermediate refined mesh is adopted. Fig. 5.3 shows the sketch of the employed mesh, with focus on the leading-edge zone.

Tab. 5.1 – Comparison of grid dependency

	mesh 1	mesh 2	mesh 3
Number of elements	240000	360000	540000
Mass flow rate (10^{-3} kg/s)	1.678	1.742	1.743

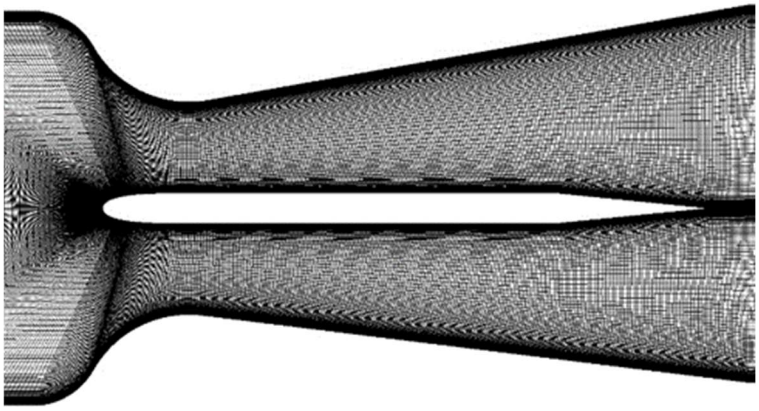

Fig. 5.3a – Mesh scheme 2 of computational domain

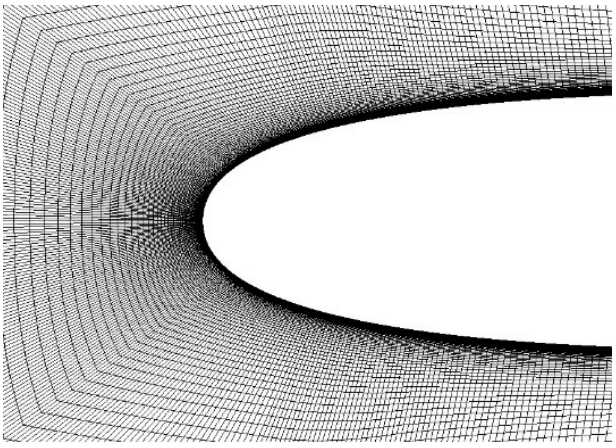

Fig. 5.3b – Mesh scheme 2 around the leading edge

5.3 Mathematical Scheme

The numerical simulations are carried out with the software Ansys Fluent [90]. The solution method is SIMPLEC scheme, while the least square cell based is adopted for the spatial discretization. The boundary conditions set for the tested cases are reported in Tab. 5.2. In inlet and outlet sections, total pressure and static pressure conditions are imposed, respectively. For turbulence and transition modelling, several models are tested in order to

identify the most proper one to describe the flow behavior within the domain and in particular along the flat plate solid wall, as reported in the following sections.

Tab. 5.2 – Boundary conditions

Name	inlet	outlet	flat plate	end-wall
Type	total pressure	static pressure	ordinary wall	Eulerian wall

5.4 Validation of Turbulence Models

In the process of Reynolds average calculation, the ability of turbulence model to solve flow problems is affected by the flow state, the degree of the assessment area near the wall, and the Reynolds number. The problem of Laminar Separation Bubble is characterized by low Reynolds number near the wall, and the formation of separation bubbles corresponds to the laminar-turbulent transition process. Therefore, the applicability of the general two-equation turbulence model is limited. For example, the $k-\varepsilon$ turbulence model is suitable for fully developed turbulent flows with high Reynolds number or free flows far from the wall. Although different $k-\varepsilon$ models have been developed in recent years, their high accuracy cannot be extended to near-wall flows with transition processes, which is directly related to the equations used. In order to improve the computational ability of boundary layer flow problems, relative turbulence models have been developed. As described in Chapter 3, SST $k-\omega$ model, and also turbulence model with transition criterion, such as Transition SST model and Transition $k-kl-\omega$ model are typical examples. In this section, the applicability of these turbulence models is calculated and compared to serve as the basis for the selection for subsequent investigations.

In addition to the turbulence models described in details above, the Standard and BSL in the $k-\omega$ model family, as well as three commonly used $k-\varepsilon$ models (Standard, RNG and Realizable) are also validated. The flow parameters and conditions are identical in the validating process. Firstly, for the problem of separation bubbles in the boundary layer of a flat plate, the results of the turbulence model of the $k-\varepsilon$ family have strongly instabilities. The convergence of the flow field under low Reynolds number is obviously weak. Even if the Reynolds number is properly increased, the convergence of the residual cannot meet the computational requirements. Observing the time-averaged flow field with strong fluctuation, but without typical transition process of laminar separation bubbles. The results show that the $k-\varepsilon$ model is not suitable for calculating laminar separation bubbles.

Tab. 5.3(a) – Turbulence model comparison

Turbulence Model	Transition		$k-\omega$		
	SST	$k-kl-\omega$	Standard	BSL	SST
convergence	√	√	√	√	√
LSB	√	√	×	×	√

The results of other turbulence models are sorted out and listed in Tab. 5.3(a). Qualitatively, the convergence situation of each model and the ability to capture laminar separation bubble are summarized as criteria for turbulence model selection. As the research works [91,92] descript, the applicability of these models to laminar separation bubbles is still different. In Tab. 5.3(a), although stable time-averaged flow field results can be obtained by various models, the capture ability of laminar separation bubbles is different, including Standard and BSL $k-\omega$ models, which fail to give typical laminar separation bubbles. This indicates that although the sensitivity of $k-\omega$ to freestream conditions is limited to the greatest extent, and can be applied to free shear flow, even logarithmic region, it is still insufficient to accurately predict flow separation caused by pressure gradient. According to the above situations, the results of three turbulence models are compared and analyzed next, they are SST $k-\omega$ model, Transition SST model and Transition $k-kl-\omega$ model, respectively.

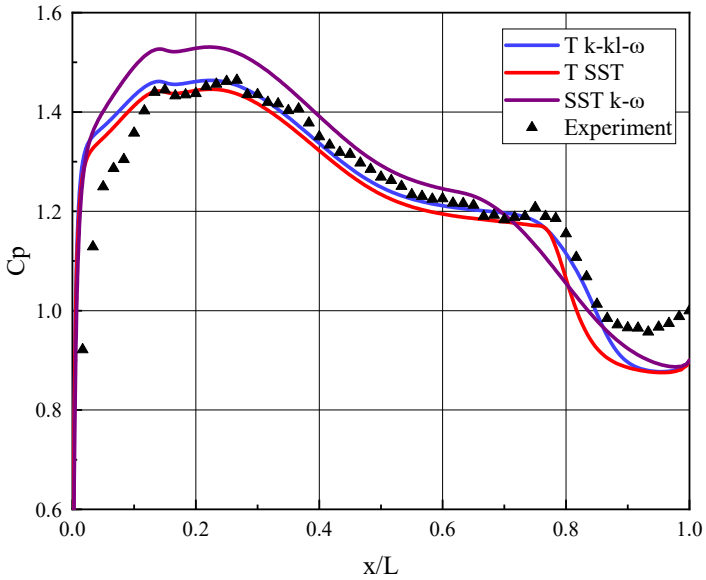

Fig. 5.4 – Turbulence models comparison in case D7-2.5 Re=150000 Tu=0.65%

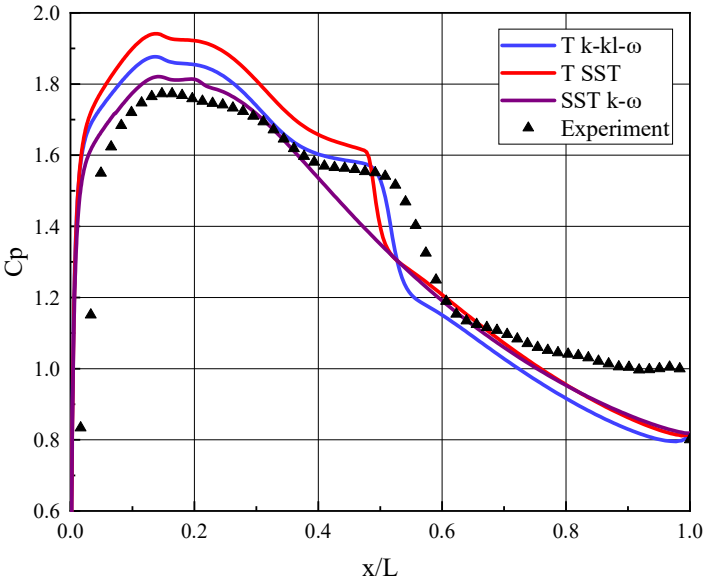

Fig. 5.5 – Turbulence models comparison in case D12-7 Re=300000 Tu=1.5%

Fig. 5.4 and Fig. 5.5 show the distribution of pressure coefficients obtained by three models under two conditions, characterized by different flow conditions (Reynolds number and turbulence intensity) and different opening angles of the diffusing test section.

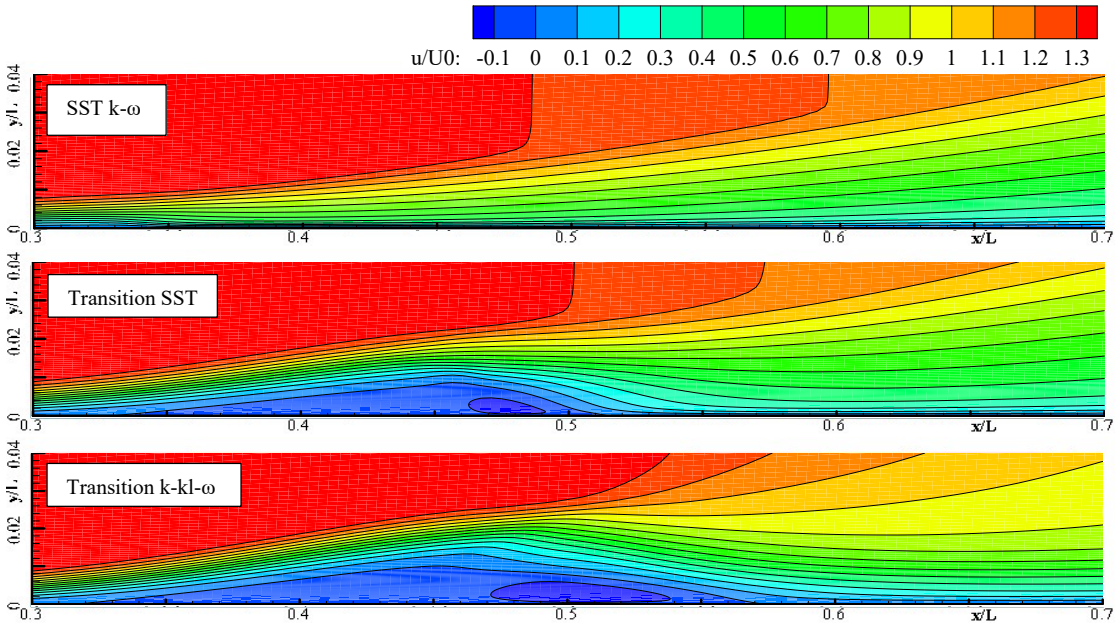

Fig. 5.6 – u/U_0 comparison with turbulence model (D12-7 Re=150000 Tu=1.5%)

Tab. 5.3(b) – The relative error (%) of turbulence model in feature position prediction

	Detachment	H_{12}	δ^*	Reattachment
Transition $k-kl-\omega$	2.8	0	3.6	1.5
Transition SST	5.6	2.0	8.9	13.8

The comparison shows that the three models have different reactivity to flat plate LSB phenomena. In these two figures, both the pressure distribution on the plate surface and the LSB region behavior reflected by the Transition $k-kl-\omega$ model have the highest consistency with the experimental results. Especially in Fig. 5.4, the Transition $k-kl-\omega$ curve begins to separate at x/L=0.52, then reaches the maximum value of separation thickness at x/L=0.79, finally reattaches at the position x/L=0.91. These feature points are close to the experimental ones, which means the bubble detachment and length are well predicted. In Fig. 5.5, the end-wall angle and Reynolds number increase. The detachment point and the growth trend of the separation zone obtained by the Transition $k-kl-\omega$ model are still the closest to the experimental results. However, the positions of the maximum thickness of LSB and the reattachment point are located forward with respect to experimental ones. Thus, the bubble length is shorter than in the experiment.

The pressure distribution curves obtained by Transition SST model are similar to those of Transition $k-kl-\omega$ model, but the deviation from the experiment is slightly bigger than that of the latter. Furthermore, in figure Fig. 5.5, the location of maximum separation thickness and the reattachment point are ahead of the latter, hence the shorter LSB's length. For SST $k-\omega$ model, as expected, the turbulence model (without transition model) is not able to correctly predict the flow behavior. In Fig. 5.4, the deviation and differences from

the experiment is the most obvious. From the appearance point of view, the thickness of the separation bubble changes most smoothly, while the position of the LSB's maximum thickness moves forward by 0.1x/L, forming a flat and longer LSB. In Fig. 5.5, the SST $k-\omega$ model cannot reflect the existence of LSB, with a flat pressure coefficient distribution curve. According to the above analysis, the Transition $k-kl-\omega$ model can fully reflect the behavior of LSB, which has the most similar appearance to the experiment. Therefore, the Transition $k-kl-\omega$ model is used in subsequent calculation and analysis.

In comparison, although the curves represented by different turbulence models have different reaction capacities to the separation bubble, the pressure distribution trends downstream of the reattachment point are highly consistent. In addition, downstream of the reattachment point, there is a certain discrepancy between the numerical simulation and the experimental results, which becoming more and more obvious with the advance of the flow. Based on the fact that numerical simulation accurately captures the displacement effect of the LSB, the discrepancy should be related to the behavior of the boundary layer developing on the inclined upper end-wall，which leads to the phenomenon of blockage downstream of the LSB not being correctly reproduced. In order to avoid flow separation appearing in the upper end-wall, tripping wire is added to the upper throat of the test section in the experimental process, while in the numerical simulation process the end-wall is set as slip type, hence, the response of the equivalent boundary layer thickness in the downstream of straight section is different. For the future study, reducing this discrepancy is important to more accurately simulate the equivalent APG environment.

Similar laws can also be observed by velocity distribution. Fig. 5.6 corresponds to the dimensionless distribution of velocity component u in three turbulence models under the same conditions. Observed results show that two turbulence models with transition criterion, Transition $k-kl-\omega$ and Transition SST, have obtained distinct laminar separation flow zones, while SST $k-\omega$ fails to capture the appearance of laminar separation bubble. Comparing the results of the last two models, the laminar separation bubble behavior are similar: the separation starting points are basically the same, the location and thickness of the maximum displacement thickness are not different, while the reattachment position of the Transition $k-kl-\omega$ separation bubble is more obvious downstream. Comparing with Fig. 5.5, it can be seen that the differences caused by different turbulence models are highly similar due to the same end-wall opening angle and turbulence intensity. The applicability differences of these models for laminar separation bubbles are further highlighted.

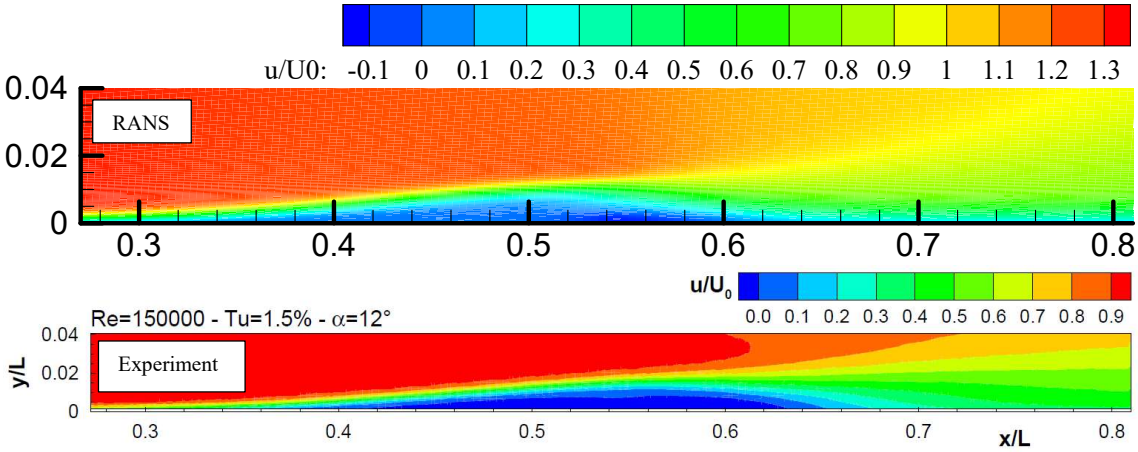

Fig. 5.7 – Colour contour of velocity component u

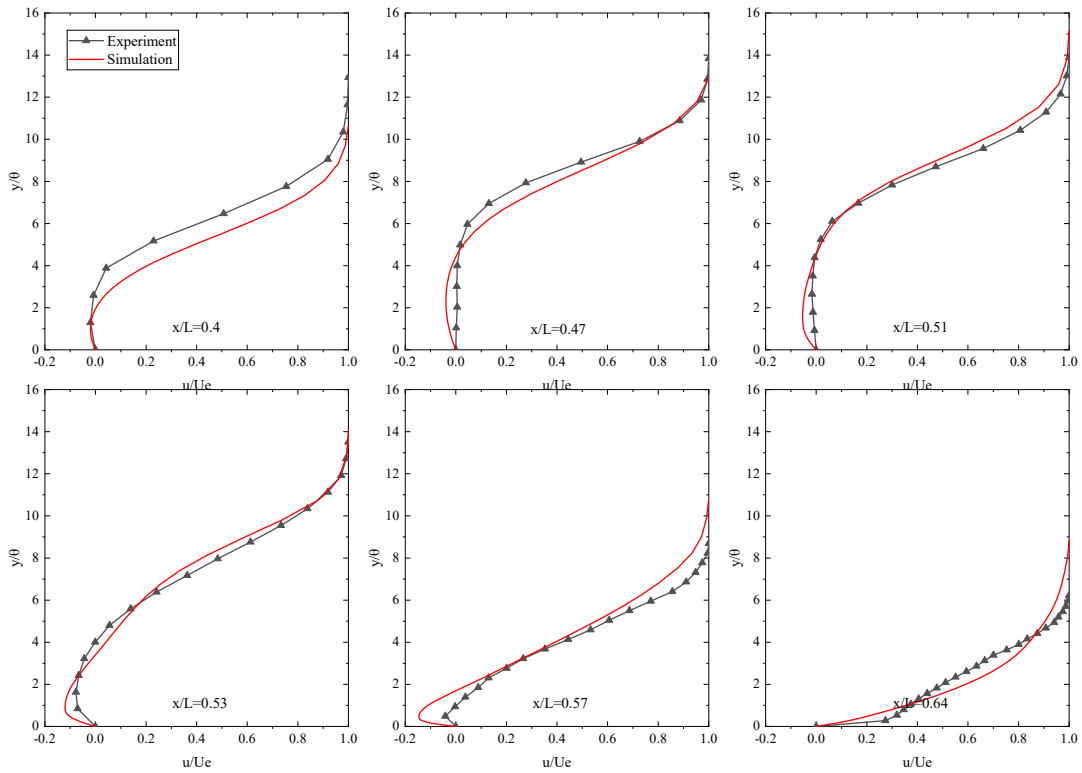

Fig. 5.8 – Velocity profiles comparison along the plate surface

Tab. 5.3(b) compares the predicted results relative error of the four LSB feature positions to the experimental values under the typical conditions by the two turbulence models with transition criteria. It can be seen that the relative error from the Transition k-kl-ω model is less than 5%, while the Transition SST model predictions are in good agreement with the experimental data in the front of LSB, but for the reattachment area is quite different (greater than 5%), which means the LSB length expands obviously shorter.

To validate the compatibility of the numerical scheme, a systematic comparison and analysis with the specific case between experiment and simulation was carried out. Fig. 5.7 and Fig. 5.8 show results for the case D12-7, with Reynolds number and turbulence intensity equal to 150000 and 1.5%, respectively. As mentioned before, the Transition $k-kl-\omega$ model is employed.

Fig. 5.7 shows that the general LSB's behavior of both experiment and simulation is similar with high level. There is no substantial difference between the two sets of LSB's feature points. Experimentally, the separation point locates at about x/L=0.36, while the simulation predicts this position at x/L=0.35. The bubble maximum thickness is captured at x/L=0.56 and x/L=0.52, for the experiment and simulation, respectively. After the position of the maximum thickness, the LSBs begin to reattach, at x/L=0.65 for the experiment, while the numerical simulation provides a value of x/L=0.62. Although the characteristic points do not coincide completely, the development trends of separation bubbles are the same even if the overall length and thickness of LSB corresponding to the experiment is slightly larger than the numerical simulation ones.

In Fig. 5.8, the velocity profiles comparison along the plate surface in specific positions between experiment and numerical simulation are plotted. The curves are normalized by the local velocity of the main flow. For the positions ahead of the maximum thickness (x/L=0.41, x/L=0.47), the experimental curves show a thicker separated flow area than those of

numerical simulation. In the three subfigures of the first row, the region with velocity component u less than 0 increases gradually in the direction perpendicular to the plate surface, and the magnitude values increase gradually, which reflects the growth of the reverse flow region and the enhancement of the internal reflux in the separation bubble. In the subfigures corresponding to x/L=0.53 and x/L=0.57, the LSB starts the reattachment process, and the comparison with the simulations becomes greater. The velocity profiles near the reattachment point are shown in position x/L=0.64, and the numerical simulation result reflects the time-averaged characteristic of turbulent boundary layer.
It can be seen from the content of this section that the selection of turbulence model is very important for the simulation of laminar separation bubbles with transition characteristics. It is reasonable and feasible to adopt a numerical simulation scheme based on Transition $k-kl-\omega$ model with transition criterion. The time-averaged characteristics of laminar separation bubbles obtained by this model are in agreement with the experimental results better than other turbulence models do.

5.5 Analysis of RANS Results

A systematic numerical simulation is made with three factors including Reynolds number, turbulence intensity and end-wall opening angle (APG level) variations, in order to obtain the response of the LSB to these parameters. Two different APG conditions are considered during the progress of RANS simulation, which they are D12-7 and D7-2.5, respectively. The Reynolds number and turbulence intensity of the freestream are basically the same under each APG condition. The results show that the influence of flow parameters on the behavior characteristics of LSB is the same under different APG conditions. Therefore, the results of D12-7 case are mainly compared and analysed in the following sections.

5.5.1 Analysis of APG D12-7

Under the APG condition of D12-7, the range of flow parameters adopted is shown in Tab. 5.4, forming a two-dimensional parameter matrix. Meanwhile, the values of these parameters are in agreement with the experimental ones. In order to facilitate analysis, some representative results including extremum parameters are counted.

Tab. 5.4 – Range of simulation conditions in case D12-7
(：partially showed only with Cp distribution)*

Re	70000, 150000, 300000, 500000
Tu	1.5%, 2.0%*, 2.8%*, 3.8%, 5.0%

Firstly, Fig. 5.9 gives a comprehensive comparison of dimensionless velocity component u-distribution with colour contours. As in Fig. 5.6 and Fig. 5.7, the local velocity component u is normalized by the mainstream velocity of the inlet section for each case, while the horizontal and vertical coordinates are normalized by the length of the plate. For all the 12 conditions, The Reynolds number and the turbulence intensity increase from top to bottom and from left to right, respectively. Therefore, the most extreme cases occur in the upper left and lower right positions accordingly. In each sub-figure, the obvious difference of velocity component u distribution can be observed: there is a closed dark blue part in the centre of the region near the wall, i.e. the reversed flow opposite to the mainstream velocity. Outside the region, both the direction and magnitude of velocity gradually returns to the mainstream

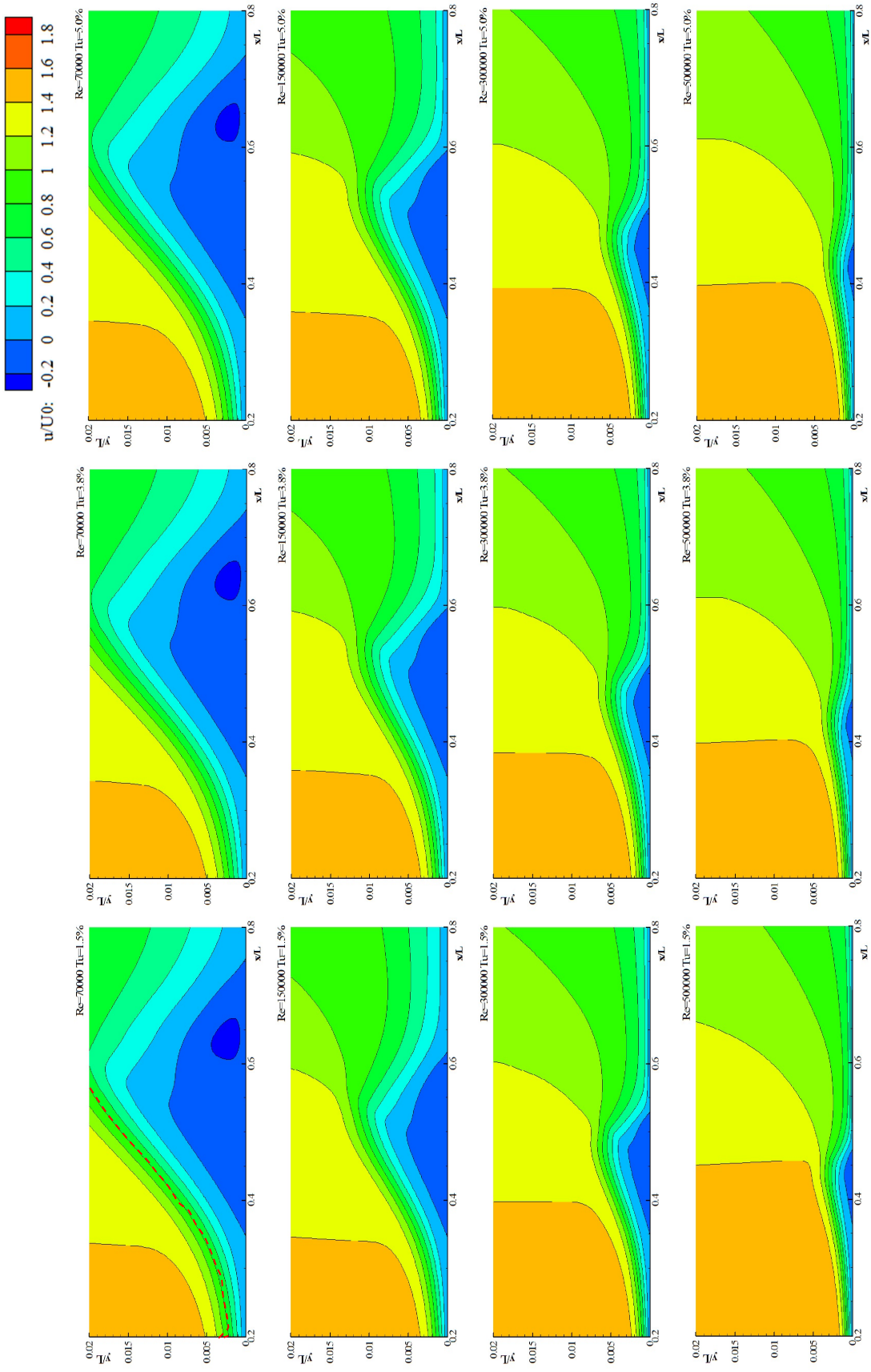

Fig. 5.9 – Comparison of normalized velocity component u/U_0

state. This closed reverse flow region, which is confined to a certain area near the wall, forms the laminar separation bubble defined earlier.

In the sub-figure of the upper left corner, the boundary of u/U_0=1 is marked with a red dotted line, which can help to understand the variation of velocity component u. It is found that with the increases of Reynolds number and turbulence intensity, the range of closed recirculation zone, the LSB, is significantly reduced, with the same trend according to references [83] and [93]. The preliminary results show that the increase of these two flows

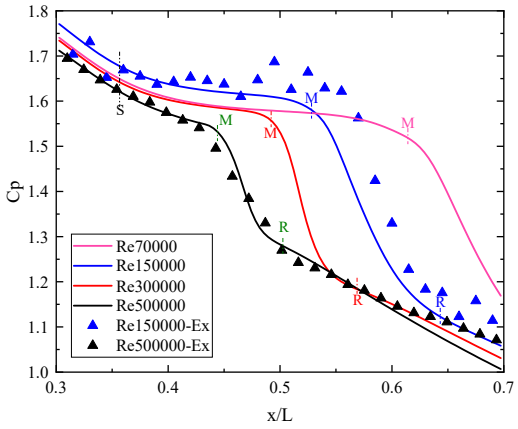

(a) – Tu=1.5%

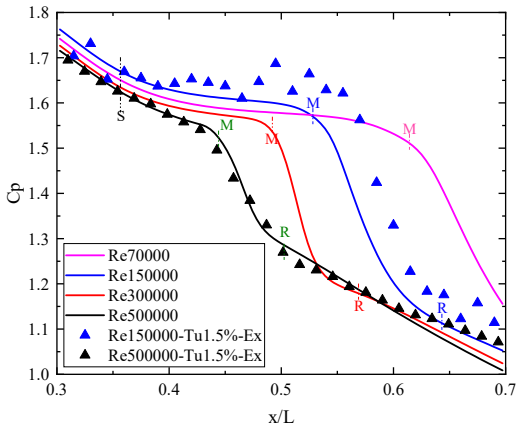

(b) – Tu=2.0%

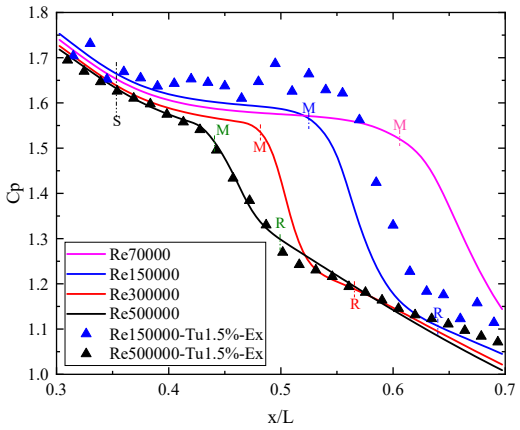

(c) – Tu=2.8%

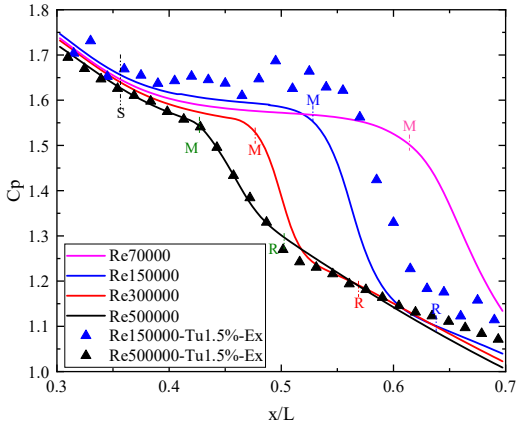

(d) – Tu=3.8%

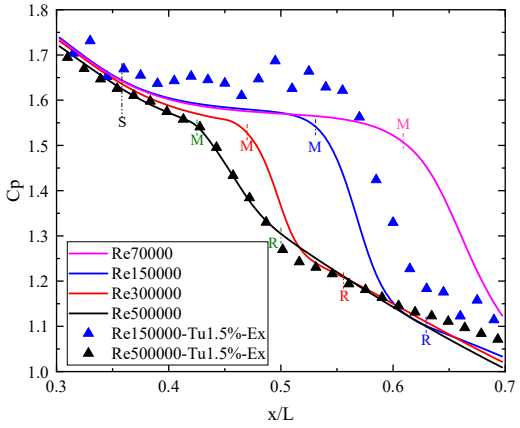

(e) – Tu=5.0%

Fig. 5.10 - Cp comparison with fixed turbulence intensity

parameters can inhibit the strength of laminar separation bubbles, but obviously, with a distinguished influence level: The trend of LSB decrease in all sub-figures of each column is larger than that in each row, that is, the influence of Reynolds number change in freestream is stronger than that of turbulence intensity. The comprehensive comparison also reveals another phenomenon: although the range and strength of laminar separation bubbles are affected by the increase of flow parameters, the initial position of laminar separation bubbles does not fluctuate in a wide range in each case, while the positions where separation ends and the maximum thickness onsets vary significantly, which affects the structural characteristics of LSB. These behavior are consistent with previous work, such as reference [94]. The above characteristics will be quantitatively analysed by parameters in the following parts.

A series of pressure coefficient (Cp) distributions due to the variations of Reynolds number and turbulence intensity are plotted in Fig. 5.10 and Fig. 5.11, with the fixed opening angle of D12-7. The experimental results under the conditions of Tu=1.5% and Reynolds number equals to 150000 and 500000 respectively are taken as references. In the figure also the peculiar positions highlighting the time-mean structure of the bubble are shown as below: "S" stands for the beginning of separation, "M" indicates LSB's maximum thickness, while "R" highlights the reattachment position.

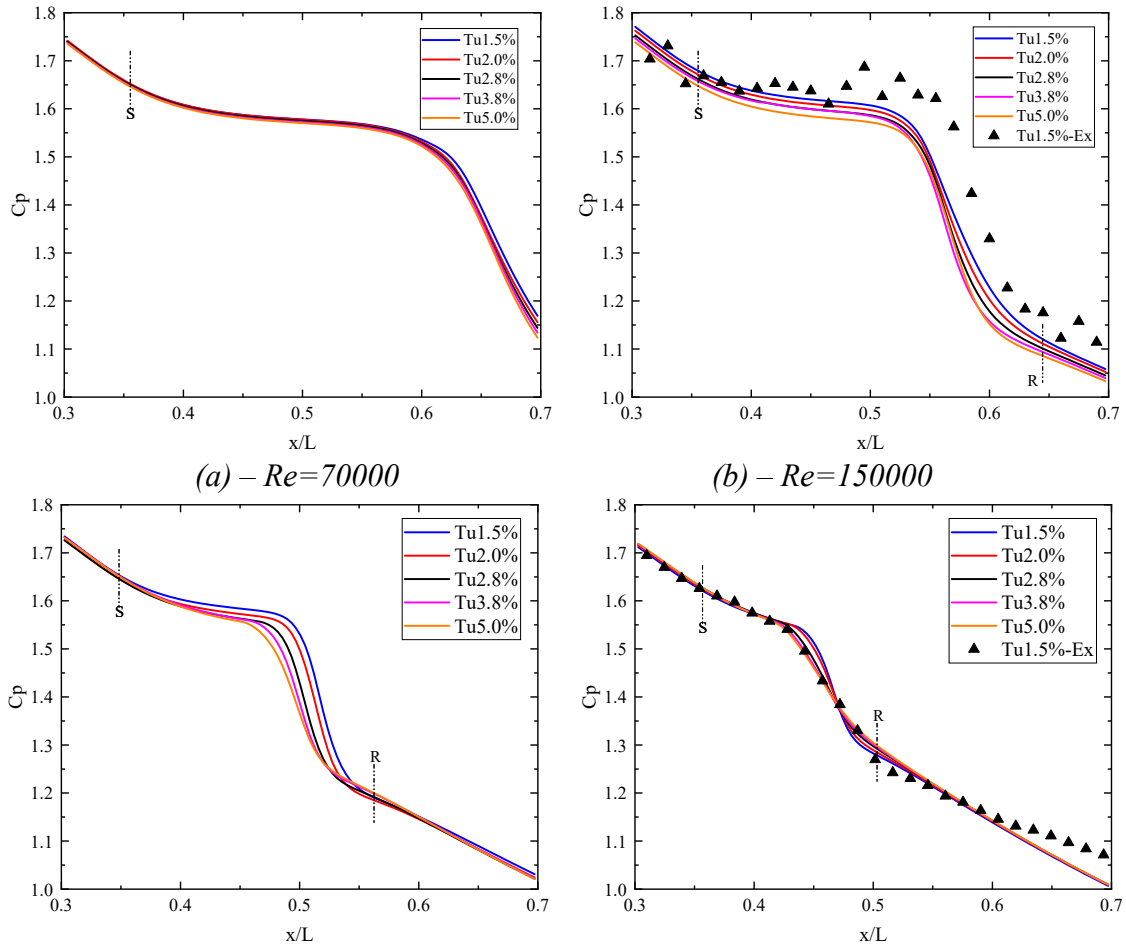

(a) – Re=70000 *(b) – Re=150000*

(c) – Re=300000 *(d) – Re=500000*

Fig. 5.11 – Cp comparison with fixed Reynolds number

Cp distributions are compared in Fig. 5.10 with five turbulence intensity levels, which including the minimum and maximum values adopted in the experiments. It can be found that the feature point "S" in each subfigure has the same abscissa, x/L=0.35, which means that the separation position barely shifts varying both Tu and Re. For the points "M" and "R", as the Reynolds number increase, they move forward to the upstream of plate, i.e., in the subfigure of Tu=1.5%, the maximum thickness abscissa moves from x/L=0.62 to x/L=0.45, while the reattachment one moves from x/L=0.75 (outside the abscissa of the figure) to x/L=0.5. These changes diminish the LSB's dimension in length, with an obvious shrinking trend. A shortening distance between points "M" and "R" is also due to the Reynolds number increment, hence, the fore part and rear part of LSB response simultaneously to the variation of Re. In the condition of Re=500000, the simulation curve is highly consistent to the experiment one.

The same Cp data is reorganized according to the fixed Reynolds number in Fig. 5.11, also including minimum and maximum Re values adopted in the experiments. By this way of classification, it can be seen that the variation of turbulence intensity has a weaker influence to the general behavior of LSB. The similar distributions of Cp curve are plotted in each fixed Re condition. Furthermore, all the main points, including the separation position, maximum thickness position and reattachment location have a marginal change, hence indicating the same length scale of LSB. Compare with these subfigures, when Reynolds number increases, the influence of turbulence intensity on separation bubbles decreases. However, the fore part of five Cp curves in the last subfigure coincide fairly well. In the condition of long LSB, such as Tu=1.5% and Re=150000, the simulation curve has the same developing trend with the experimental one, although the difference between them enlarges. The detachment and reattachment positions are listed in Tab. 5.5 and Tab. 5.6 respectively, with opening angle D12-7 and varied Re and Tu. While position "M" is plotted in Tab. 5.7 as maximum δ*. The data also reveal that the longest bubble onsets in all cases that Reynolds number equals to 70000, the same trend according to the investigations carried out by Simoni [95] et al. To highlight the typical case (Re=150000 and Tu=1.5%), the positions of LSB from experiment are listed (marked in blue) in Tab. 5.5 to Tab. 5.8 as references.

Tab. 5.5 – Detachment positions (x/L) in case D12-7

	Tu=1.5%	Tu=3.8%	Tu=5.0%
Re=70000	0.35	0.35	0.35
Re=150000	0.35 (0.36-Ex)	0.35	0.35
Re=300000	0.35	0.36	0.37
Re=500000	0.36	0.38	0.38

Tab. 5.6 – Reattachment positions (x/L) in case D12-7

	Tu=1.5%	Tu=3.8%	Tu=5.0%
Re=70000	0.75	0.74	0.73
Re=150000	0.64 (0.65-Ex)	0.62	0.62
Re=300000	0.57	0.55	0.55
Re=500000	0.50	0.49	0.49

Tab. 5.7 – Maximum δ positions (x/L) in case D12-7*

	Tu=1.5%	Tu=3.8%	Tu=5.0%
Re=70000	0.62	--	0.61
Re=150000	0.54 (0.56-Ex)	0.52	0.52
Re=300000	0.48	0.47	0.46
Re=500000	0.44	0.43	0.43

Tab. 5.8 – Maximum H_{12} positions (x/L) in case D12-7

	Tu=1.5%	Tu=3.8%	Tu=5.0%
Re=70000	0.58	--	0.56
Re=150000	0.51 (0.51-Ex)	0.51	0.51
Re=300000	0.47	0.46	0.45
Re=500000	0.43	0.42	0.42

In order to highlight the flow characteristics, the time-mean velocity profiles of LSB sections are analysed. These sections cover the regions before and after LSB, which are representative. The analysis results are summarized from Fig. 5.12 to Fig. 5.14. Fig. 5.12 synthetically analyse the dimensionless velocity profiles along the typical sections of streamline with different flow parameters. Fig. 5.13 and Fig. 5.14 highlight the comparisons of dimensionless velocity profiles when the LSB range is taken as the limit value.

Fig. 5.12 compares the velocity characteristics under fixed turbulence intensity conditions. It is observed that in the position of x/L=0.3, because the separation of flow has not yet occurred (referring to the distribution of the Cp curve), the velocity profiles all show the same laminar flow characteristics, and the curves corresponding to different Reynolds numbers can be highly coincident. When the relative height (ordinate) takes value as 8, the bottom velocity can reach the mainstream value of the outer layer. According to Tab. 5.5, it can be seen that the laminar separation has taken place under all conditions at the position of x/L=0.4. Therefore, the viscous sublayer near the wall has begun to appear reverse velocity flow, but with a relatively small value. At the same time, the relative height of the velocity *u* to the outer velocity *Ue* is increased to 10, and the difference caused by Reynolds number can also be observed. The velocity profiles at x/L=0.5 and x/L=0.6 have the most obvious differences. Since the maximum momentum thickness of high Reynolds numbers (Re=300000 and Re=500000) have appeared, the velocity profiles begin to fall back. For example, the Re500000 profiles have shown obvious turbulent characteristics, indicating the completion of separation, reattachment and transition, and the relative height required to reach the outer velocity falls back about to 8. The relative height of two curves with low Reynolds number (Re=70000 and Re=150000) to reach the outer velocity can reach more than 14, and there is still a distinct reflux velocity and scope. At downstream of x/L=0.6, the maximum momentum thickness under the condition of Re=150000 has also reached, hence the velocity profile begins to fall, while Re=70000 still has obvious reflux characteristics, and the relative height is close to 16. The other two high Reynolds number velocity profiles show more obvious turbulence characteristics. At position x/L=0.7, Re=70000 profile begins to fall, but the attachment is still not completed. Under the other three Reynolds number conditions, the difference between the profiles with obvious turbulence characteristics is getting smaller and smaller, that is to say, they have entered the stage of fully developed turbulence. Overall comparison still shows that the variation of Reynolds number has a

stronger effect on the velocity profile than that of turbulence intensity does. With the increase of both Reynolds number and turbulence intensity, a shorter LSB can be obtained, i.e. a faster separation-transition process.

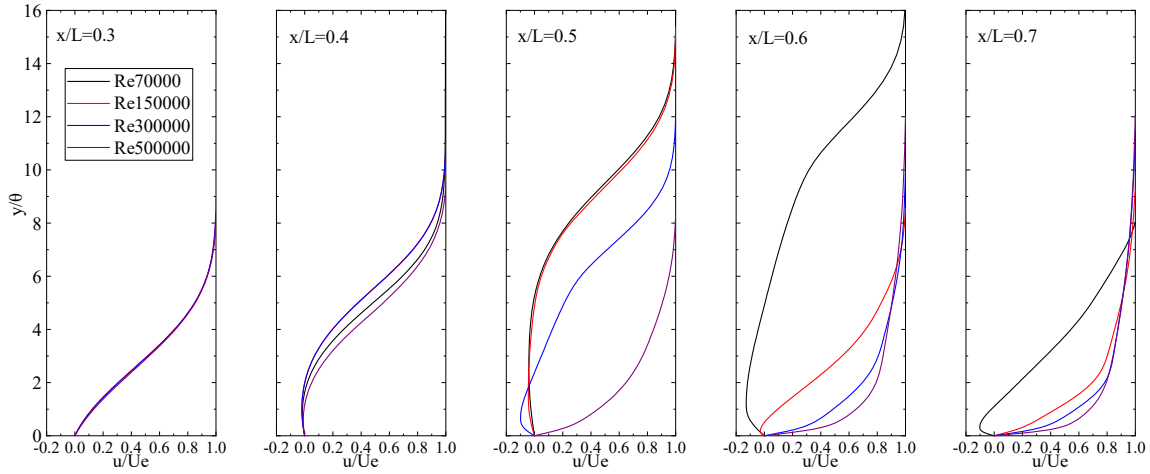

(a) – Tu=1.5%

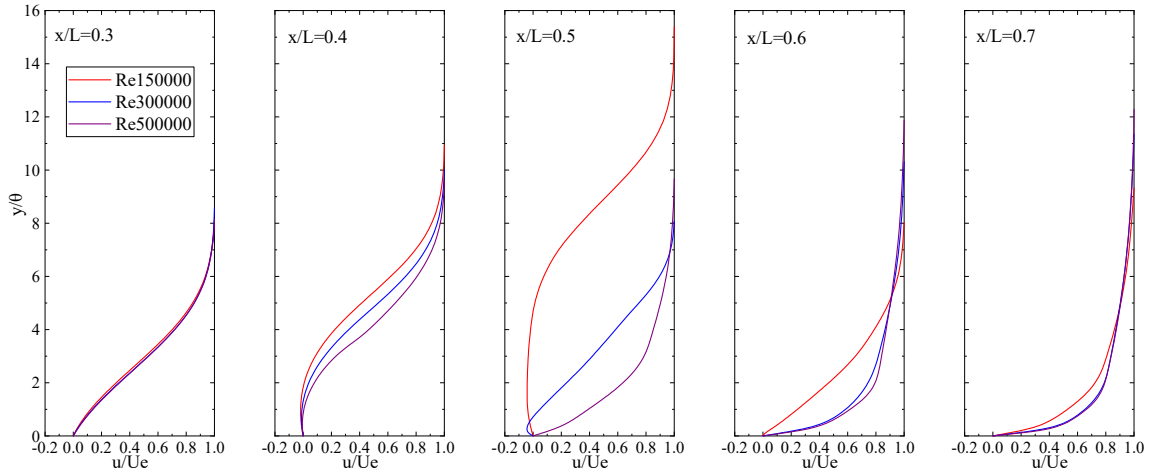

(b) – Tu=3.8%

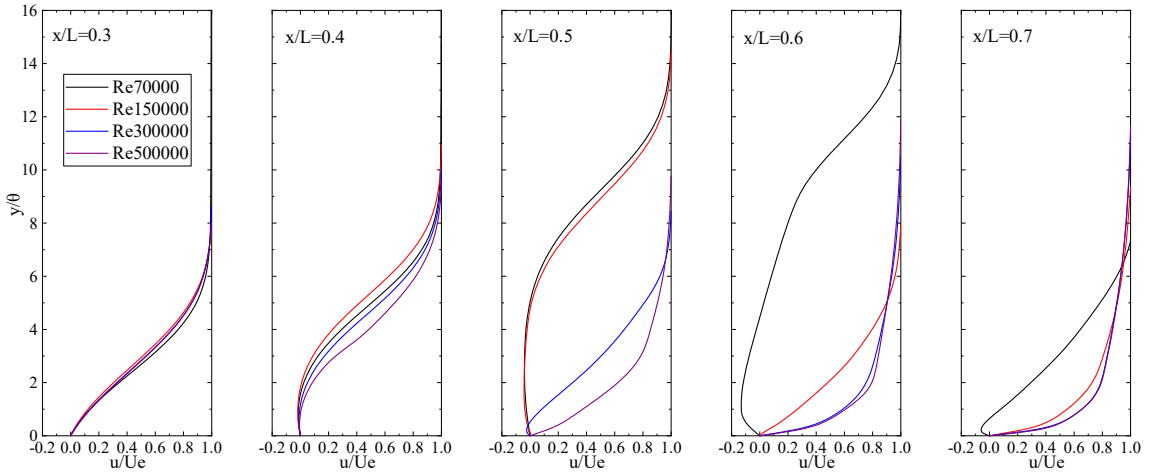

(c) – Tu=5.0%

Fig. 5.12 – Velocity profile comparison with fixed turbulence intensity

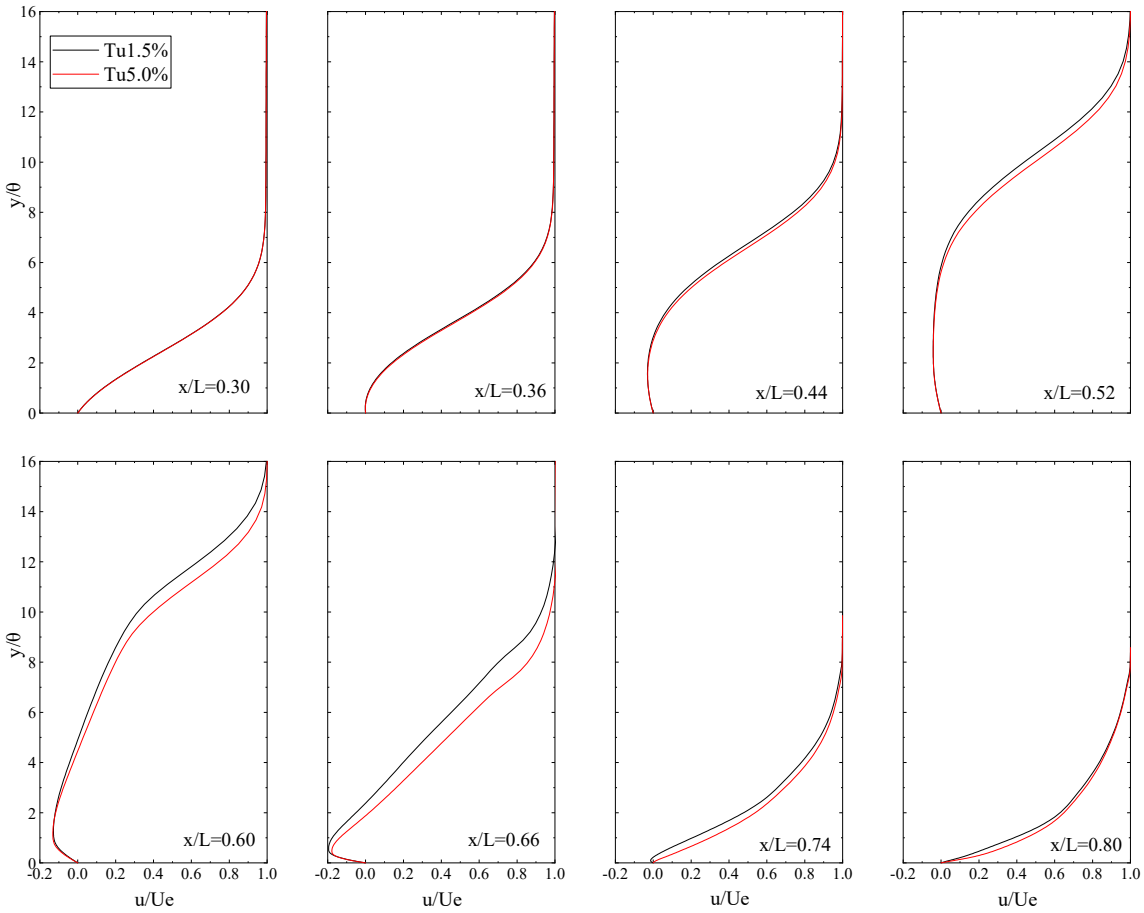

Fig. 5.13 – Velocity profile comparison with fixed Re=70000

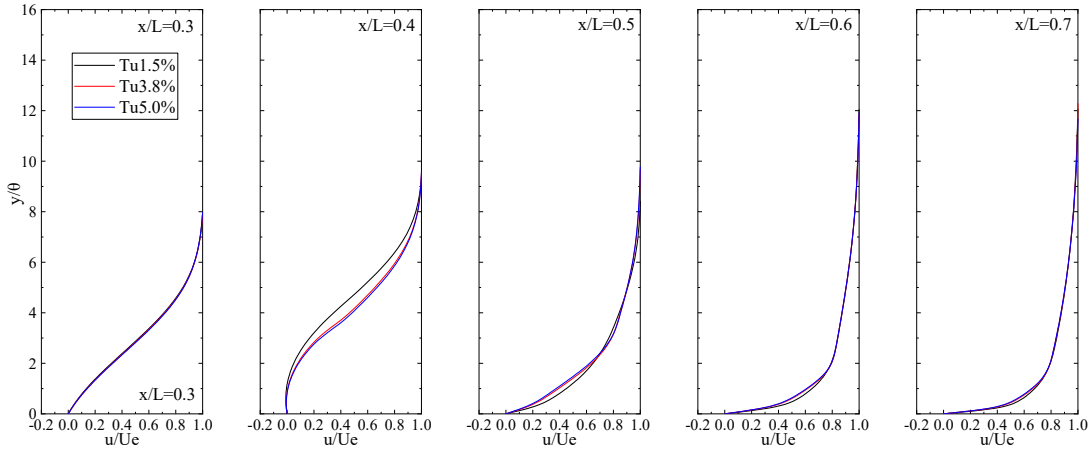

Fig. 5.14 – Velocity profile comparison with fixed Re=500000

Under the condition of Re=70000, the range and thickness of laminar separation bubbles is obviously larger than those of other cases. Therefore, eight representative cross sections are intercepted in the extended x/L range (0.3-0.8) for further velocity profile analysis, as shown in Fig. 5.13. It can be found that before x/L=0.6 position, the thickness of the reverse velocity area increases obviously, then falls back rapidly after reaching the maximum thickness. At the position of x/L=0.8, the reattachment is completed, which means the turbulent velocity distribution is obvious. In different positions, there are obvious differences between the two

groups of curves of x/L=0.6 and x/L=0.66, while the rest curves are basically identical, indicating that the turbulence intensity mainly affects the flow distribution near the maximum thickness region of LSB.

The velocity profile distributions in Fig. 5.14 correspond to the shortest LSB with the Reynolds number equals to 500000. In the figure, only the position x/L=0.4 has the velocity distribution of reverse flow, and the difference between the corresponding profiles of different turbulence level is obviously greater than those of other locations. Combining Tab. 5.5 and Tab. 5.6, it can be seen that in the range from x/L=0.3 to x/L=0.5, both flow separation and reattachment are completed, the range of laminar separation bubbles is obviously smaller than the corresponding values of other conditions. At the downstream of the reattachment position, the turbulent flow profile gradually stabilizes, and the velocity distributions of the last two sub-figures are basically the same.

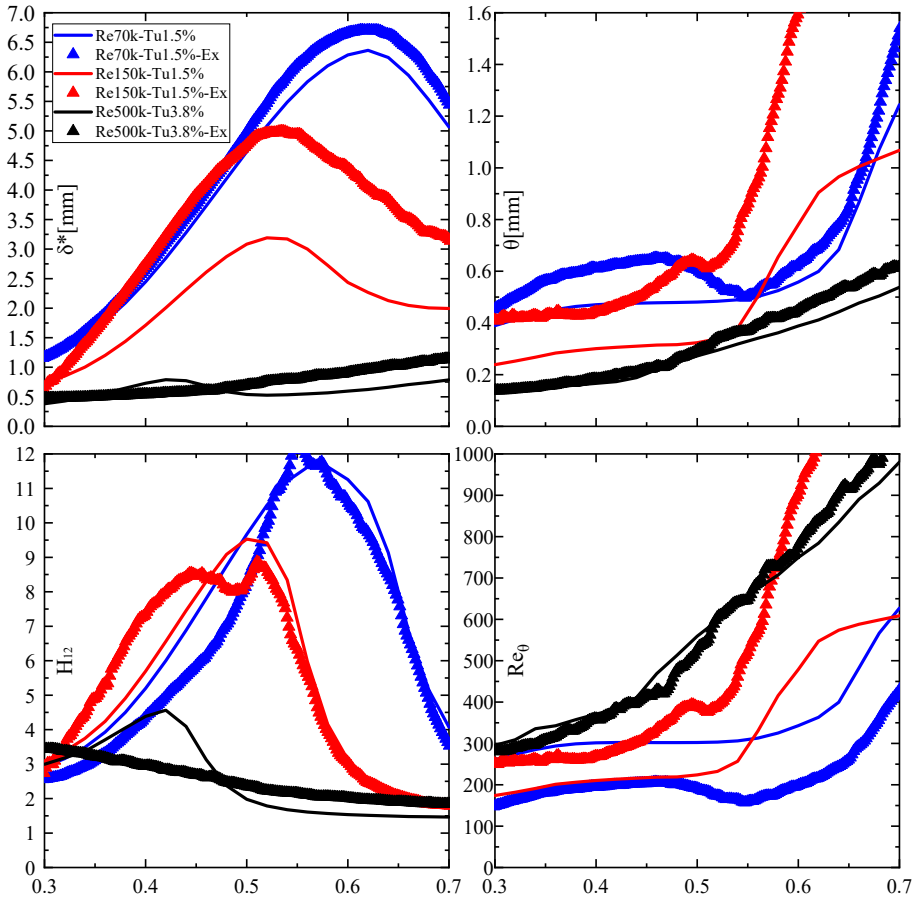

Fig. 5.15 – Integral parameters comparison with experimental results in typical cases

To synthesize turbulence intensity and Reynolds number effects on the time-averaged properties of LSB, the boundary layer integral parameters, such as displacement thickness δ*, shape factor H_{12}, momentum thickness θ and corresponding Reynolds number Re_θ have been calculated and plotted in following figures, which are normalized in stream-wise coordinates in order to detect the characteristic positions of the laminar separation bubbles occurring in different conditions. Three typical cases according to the experiment conditions are illustrated in Fig. 5.15, which including all the four integral parameters aforementioned. It can be seen that the numerical simulation results for laminar separation phenomena have the same trends and characteristic positions according to the experimental ones, especially

for the cases under low Reynolds number and low turbulence conditions are highly consistent, but the laminar displacement thickness under high Reynolds number and high turbulence intensity is different from the experiment. There is a bulge in front of the experimental displacement thickness curve distribution, which leads to the difference of the shape factor. The experimental curve shows that in the condition of Re500000-Tu3.8%, the curve is smooth and without laminar separation zone. This shows that the bypass transition is still predicted as flow separation mechanism by numerical simulation under high Reynolds number and turbulent disturbance. In addition, at low Reynolds number, the distribution of Re_θ curve further enlarges the difference, but the overall trend is consistent.

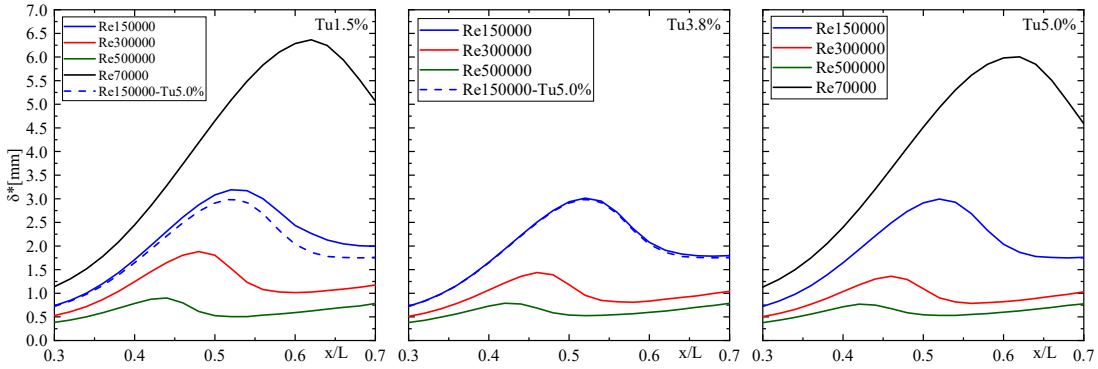

Fig. 5.16 – Displacement thickness distribution comparison by fixed Tu

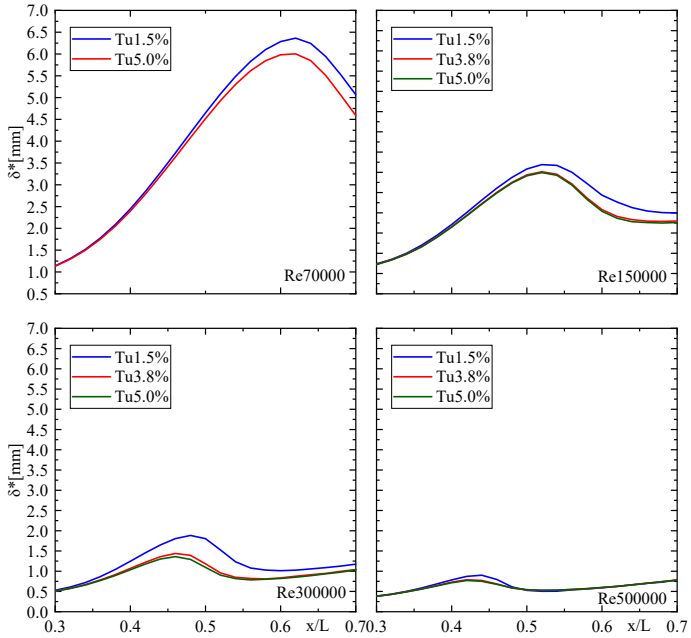

Fig. 5.17 – Displacement thickness distribution comparison by fixed Re

The distribution of displacement thickness δ* is able to quantify the maximum thickness position of LSB, while the peak value in the distribution of shape factor H_{12} reveals the transition onset [62,95-98]. In Fig. 5.16, the simulation results show the effect of Reynolds number on displacement thickness δ* under the condition of D12-7 and Tu=1.5%, with the reference case of Tu=5.0% Re=150000. The displacement thickness curves corresponding

to different Reynolds numbers have the same trend. The trend of δ* indicates the separation bubble growth, then reduction to reattachment and re-increase, respectively. Among them, the growth rate of the first stage is greater than that of the third stage, and the thickness corresponding to the location of the reattachment position is also greater than the initial value. With a fixed turbulence intensity, the displacement thickness shrinks evidently and the maximum position moves upstream by increased Reynolds number. This confirms what deduced by the Cp curve. The dashed curve in the diagram indicates that turbulence intensity has a weaker influence to LSB's displacement thickness than that of Reynolds number. Another evidence is the reorganized sortation with the same set of data in Fig. 5.17.

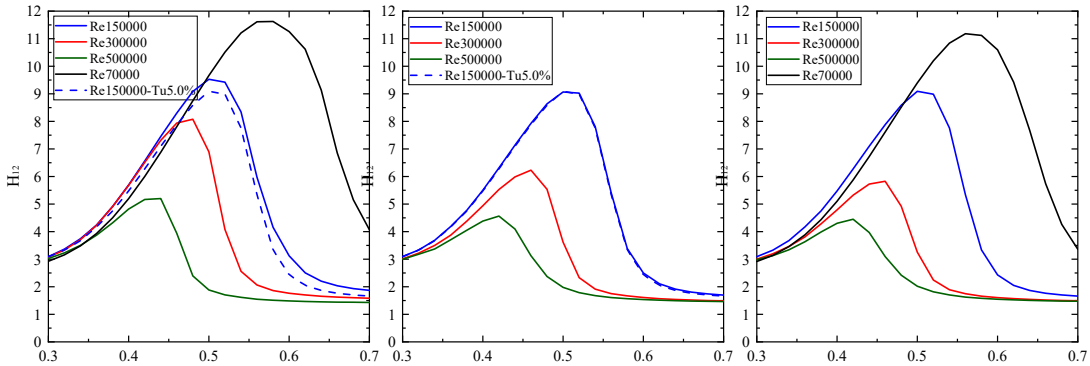

Fig. 5.18 – Shape factor distribution comparison by fixed Tu

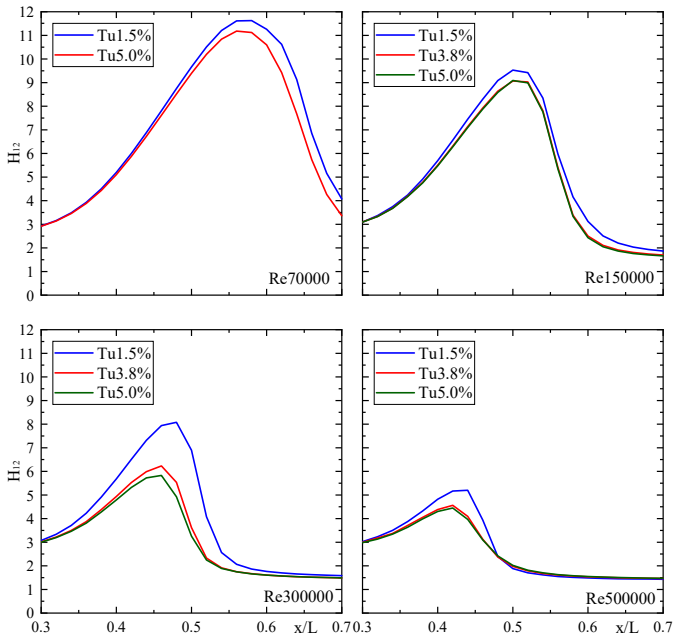

Fig. 5.19 – Shape factor distribution comparison by fixed Re

In Fig. 5.18, the LSB's shape factor obtained from simulations are plotted for the same conditions in Fig. 5.16, with the reference case Tu=5% Re=150000 shown by dashed line also. From an overall perspective, with fixed turbulence intensity condition, the shape factor distribution reduces raising the Reynolds number, showing the same trend of the displacement thickness curves. Moreover, the peak value position of shape factor moves

raising the Re number, indicating that the transition point moves forward. The initial shape factor values equal to 3 in all the cases, then the curves begin to grow linearly as the separation begins. The position of maximum shape factor indicates the transition onset position. The peak values exceed 4 for every condition, clearly indicating a separated state of the boundary layer. Conversely, at the end of the plate the curves reduce significantly, showing an asymptotic to a constant value. The shape factor values at the end of the investigated area varies from 1.5 to 1.9, indicating a fully developed turbulent boundary layer (except case Re70000). Comparing the two curves in the cases Re=500000 and Re=150000, it is possible to see that the peak value of the former is about half that of the latter. By the comparisons from Fig. 5.16 to Fig. 5.18, it can be seen that the maximum displacement thickness position occurs downstream than the transition onset position. The reference case also reveals that the shape factor is more influenced by Reynolds number than the turbulence intensity, which is further highlighted by the plot in Fig.5.19. To summarize, the maximum displacement thickness and shape factor positions are quantified in Tab. 5.7 and Tab. 5.8. Slight changes are produced when turbulence intensity is changing, similar to Tab. 5.5 and Tab. 5.6.

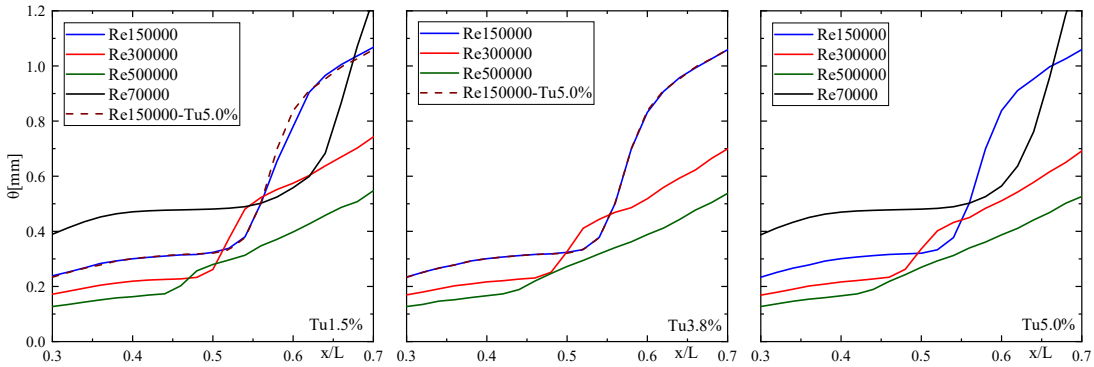

Fig. 5.20 – Momentum thickness distribution comparison by fixed Tu

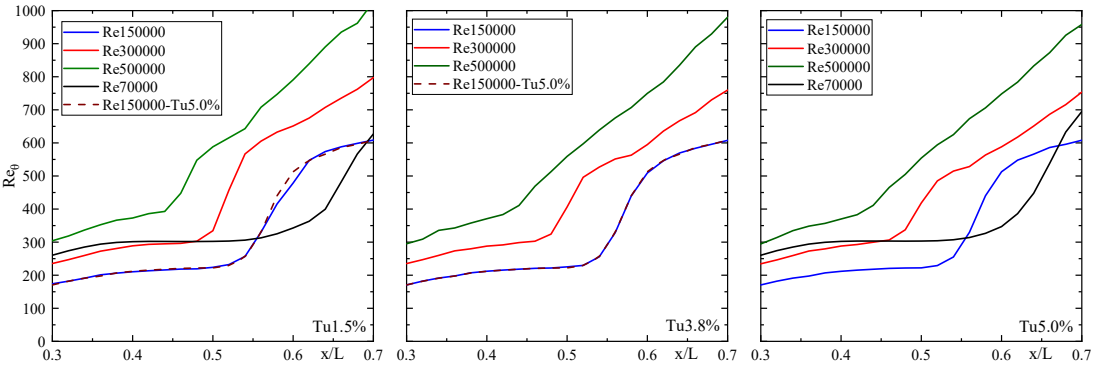

Fig. 5.21 – Re_θ distribution comparison by fixed Tu

The momentum thickness θ is a more commonly used parameter in boundary layer flow analysis. It not only relates to shape factor, but also can be used to calculate corresponding Reynolds number. For example, $Re_{\theta s}$, the Reynolds number of momentum thickness at the separation point, which usually appears in the experimental correlations available in literature for the characterization of the separated flows transition in turbomachinery applications [11]. Fig. 5.20 and Fig. 5.21 show the distribution comparisons of momentum thickness and Reynolds number of momentum thickness under the condition of fixed

turbulence level, respectively. The curves in each case show a gradual divergence trend, which indicates that the variation of flow separation is consistent with the research of Lardeau [99] and Simoni [95] et al. By comparing with the reference curve Re150000-Tu5.0%, the rule that Reynolds number has greater influence than turbulence level still can be obtained. Reynolds number of momentum thickness plays an important role in describing the experimental correlation of flow separation and transition in turbomachinery applications.

5.5.2 Effect of APG on LSB Characteristics

In the previous analysis, the variation of Reynolds number and turbulence intensity do not have a significant impact on the separation position. In fact, it is affected most by the opening angle of the end-wall. Different end-wall opening angles are adopted during both experiments and numerical simulations, hereby in Fig. 5.22, the cases corresponding to the shortest and longest LSB are considered. Here the maximum and minimum Reynolds number and turbulence intensity are shown for the opening angle equals to D12-7 and D7-2.5. Data in the figure clearly show that regardless of the end-wall opening angle, the effect of Reynolds number on the separation zone is greater than that of turbulence intensity, in agreement with the previous analysis. Interestingly, reducing the opening angle from D12-7 to D7-2.5, the LSB separating position shifts downstream of the plate, from x/L=0.36 to x/L=0.47. Also, the reattachment position shifts backwards, and the bubble becomes longer. Indeed, with fixed turbulence intensity and Reynolds number, the distance between detachment and reattachment positions in the case of D7-2.5 is enlarged than case D12-7, which means the LSB's length is stretched by reducing the opening angle. The velocity fluctuation penetrations into the boundary layer is not affected by APG, so it is believed that the main cause of the transition delaying is the change of shear layer thickness at the separation point. In fact, when APG (end-wall opening angle) decreases, the thickness of LSB at separation point enhances. Therefore, the typical dimensions of K-H vortices originating in the separation shear layer and driving the subsequent transition layer are different, as Simoni [100] et al. described and discussed in their work. One way to further reduce and avoid separation is by continuing to reduce the end-wall angle, i.e. the APG. For this low turbulence condition, the transition is not completed in the concerning area, such as the entire length of flat plate.

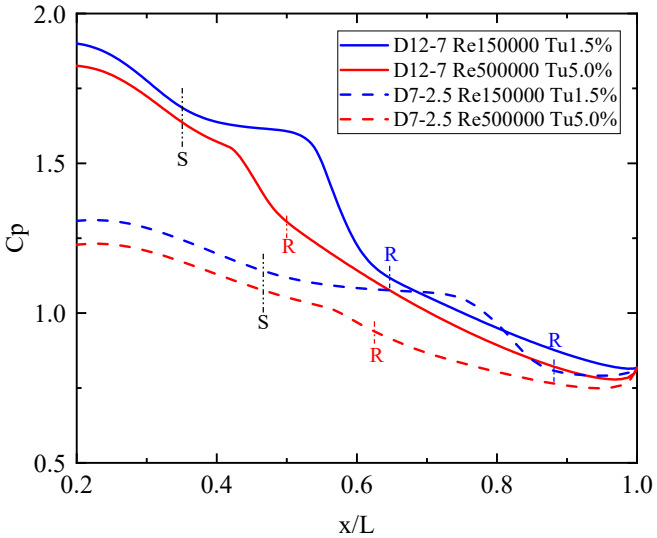

Fig. 5.22 – Cp comparison with different opening angle

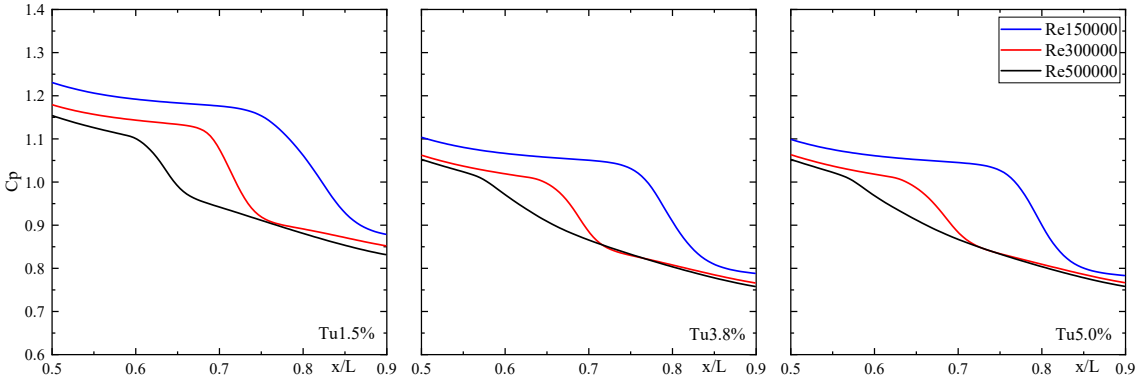

Fig. 5.23 – Cp comparison with fixed turbulence intensity in case D7-2.5

As mentioned in the forepart of section 5.5, for different APG conditions, the LSB's behavior keeps the similar trend according to the variations of Reynolds number and turbulence intensity. Therefore, Fig. 5.23 illustrates Cp distribution comparisons in D7-2.5 case with 3 fixed Tu and 3 varied Re. All the sub-figures reveal a stronger influence reflected by Re than it is done by Tu. In addition, a delayed and enlarged LSB is obtained in each diagram with lower Re, comparing with the same conditions in case D12-7.

5.5.3 Effect of incidence angle on LSB characteristics

Fig. 5.24 compares the effect of different incidence angle of airflow on the characteristics of LSB. Based on case D12-7, the horizontal angle of the lower end-wall is adjusted to 12 degrees, that is, the upper and lower passages of the flat plate form a symmetrical flow field. Therefore, the incidence angle of the plate leading edge airflow is reduced to 0 degrees (case D12-12). The overall comparison shows that the pressure distribution on the plate surface is basically consistent with that of D12-7 in the symmetrical flow field, especially for the short LSB. While at low Reynolds number and low turbulence intensity conditions, the pressure distribution curves of LSB are basically the same. The main difference is that the pressure distribution curve of D12-12 is steeper, and downstream of the maximum thickness of LSB, the velocity of reattachment is slightly faster than that of D12-7, and the position of reattachment moves forward to the vicinity of x/L=0.6. The initial separation position and maximum thickness position remain unchanged, which means that surface flow separation cannot be delayed or suppressed by this method.

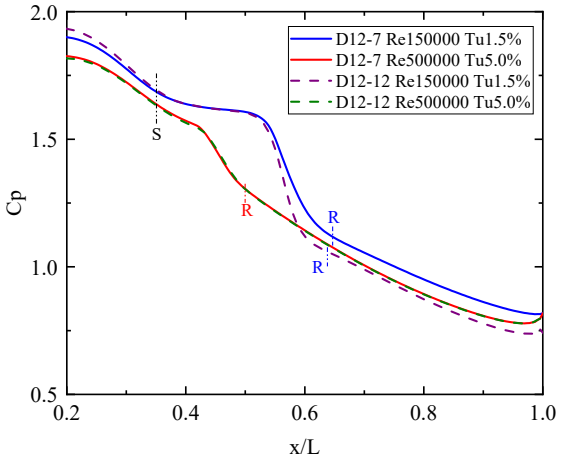

Fig. 5.24 – Cp comparison with different incidence angle

5.6 Analysis of URANS Results

Compared with LES and DNS, which spend highly in time, the URANS method with many effective turbulence models has greater advantages in computing time costs. In terms of computational accuracy, the large-scale vortex structures obtained are often the eddy scale range that interested in engineering applications. In the past, Rumsey [101] et al. and Dejoan [102] et al. used URANS to study the boundary layer flow under zero or lower pressure gradient conditions, and gave the applicability of URANS to these problems. Therefore, the unsteady simulation in the present work is to expand the predictive ability of URANS for laminar separation characteristics in low pressure turbine environment.

The URANS theoretical part is introduced in section 3.4, and process is based on the previous steady-state calculation results, hence the Transition $k-kl-\omega$ model with the highest experimental coincidence for the time-averaged LSB is still adopted. The spatial derivatives are discretized using a second order upwind scheme while the time integration employs a fully implicit second-order backward stencil. After preliminary trial calculation, the SIMPLEC algorithm is used for pressure–velocity coupling, which it's convergence and stability of the calculation can be guaranteed at the same time. According to the small perturbation theory and based on the stable LSB time-averaged result, a small perturbation is imposed in the flow field to trigger the unsteadiness and an appropriate time step sized accurate simulation is carried out. While the time step size is based on the estimation of the vortex shedding phenomenon correlated to experiment. Then sufficient time steps in each period of simulation are necessary. In addition, the present URANS investigation is carried out with a fixed opening angle, i.e. APG condition takes D12-7.

5.6.1 The choice of time step size

In the calculation of URANS, the time interval between two adjacent transient states is one of the key factors to obtain unsteady flow field, that is, the choice of time step size. This parameter depends on the physical process studied. Therefore, the numerical simulation refers to the corresponding experimental data. Tab. 5.9 gives the experimental frequency, f_{ex}, of the shedding vortices from the transition aera observed under three typical Reynolds number conditions when the turbulence intensity fixed on 1.5%. The periodicity of shedding vortices in statistical time can be determined by this frequency. Just like the strategy adopted by PIV system, when observing a periodic motion, enough acquisition points need to be given in a single motion cycle to ensure the authenticity of sampling. On the contrary, too dense sampling frequency will impose a burden on data processing. Therefore, the number of sampling point n in a single motion cycle is the key to the selection of time step size, that is Δt. Tab. 5.9 also shows the effect of Δt selection on the calculation results under different Reynolds numbers. According to the definition, we have that

$$\Delta t = 1/(n \times f_{ex}) \tag{5.5}$$

Tab. 5.9 – Time step size in condition Tu=1.5%

Re	f_{ex}	n_1 \ Δt_1 (10^{-4}s)	n_2 \ Δt_2 (10^{-4}s)	n_3 \ Δt_3 (10^{-4}s)
70000	75	20 \ 6.7	30 \ 4.4	60 \ 2.2
150000	280	10 \ 3.57	20 \ 1.9	30 \ 1.19
220000	550	10 \ 1.8	20 \ 0.9	30 \ 0.6

In Tab. 5.9, the time step size corresponding to the blue font are the cases which the unsteady flow field can be obtained. While, in other states, it is impossible to capture the phenomenon of unsteady processes or numerical divergence. Hence, it can be seen that there is an upper limit of time step size for URANS calculation, i.e. the maximum time interval, and the corresponding limits are not the same in different cases. Taking Δt more less than this time interval limit, an extended calculation progress should be given. Therefore, it is necessary to select time step size around the time interval limitation.

5.6.2 Dynamic analysis of URANS results

After determining the numerical simulation strategy of URANS and verifying its rationality, several numerical simulations with representative states are completed, which mainly refer to the corresponding experimental conditions. Fig. 5.25 shows the distribution of the transient velocity vector map under the condition of Re150000-Tu 1.5%, the typical case according to RANS simulation. For the velocity vector field, it is necessary to carry out statistical average in the whole flow field within the prescribed statistical time interval, then obtain the transient fluctuating velocity distribution. According to the velocity map, the obvious vortexes from the vicinity of the transition point can be observed, they gradually move along the flow direction, forming a periodic vortex shedding phenomenon. In order to make a clearer comparison, the positions of maximum shape factor, the maximum displacement thickness and the reattachment corresponding to the time-averaged flow field are marked. Especially, the position of the disturbance is highly coincided with the maximum position of the shape factor, which is located at x/L=0.51 and will be introduced as following.

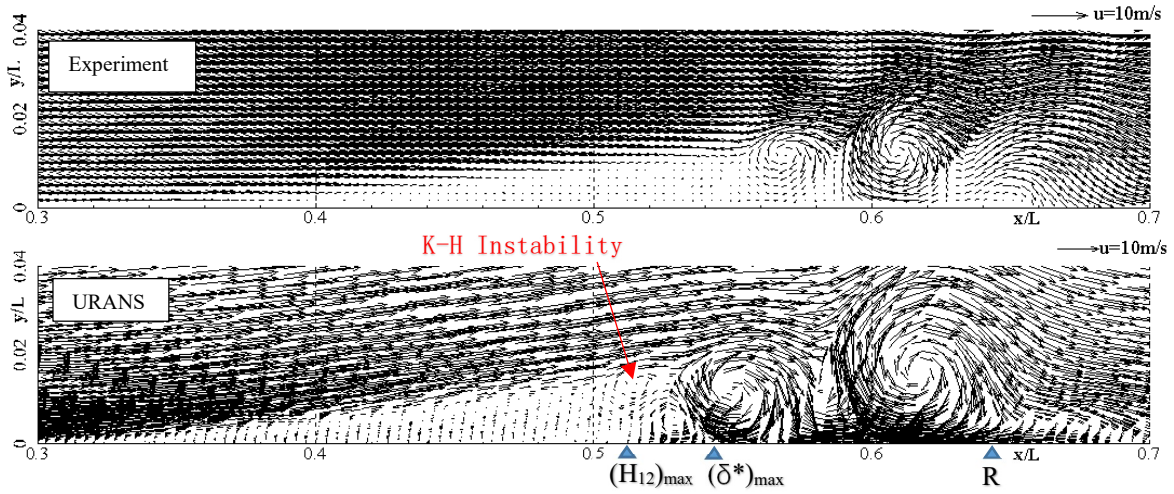

Fig. 5.25 – Instantaneous velocity vector (u, v) distribution Re=150000 Tu=1.5%

In Fig. 5.25, a marked bending oscillation, K-H instability, can also be observed in the upstream of separated shear layer. It can be used as a reference for the wavelength of the subsequent shedding vortices, and the specific location needs to be quantitatively determined by the fluctuating velocity map. This K-H instability gradually moves downstream and enlarges, which leads to visible large-scale vortex structures. Then the vortex structure becomes a prelude to shear layer roll-up and causes subsequent continuous vortex shedding process, i.e. K-H roll-up. Combining with Fig. 5.26, it can be found that the concentration areas of positive and negative partial velocity in Y direction alternate, which indicates that since the first vortex structure, the directions of adjacent two vortices are different, and the

vortexes rotating clockwise and counter-clockwise are separated from each other. In fact, the structure of counter-clockwise rotating vortexes is the result of the viscous interaction between two clockwise vortexes, and the appearance of clockwise rotating vortexes is caused by the periodic roll-up of the shear layer. Compared with the experimental results of Simoni [98], it is found that the large structure vortexes downstream of the numerical simulation flow field can propagate relatively steadily, rather than gradually decay into small-scale structure vortex, which is related to the fact that the turbulence model cannot capture the characteristics of smaller-scale vortex.

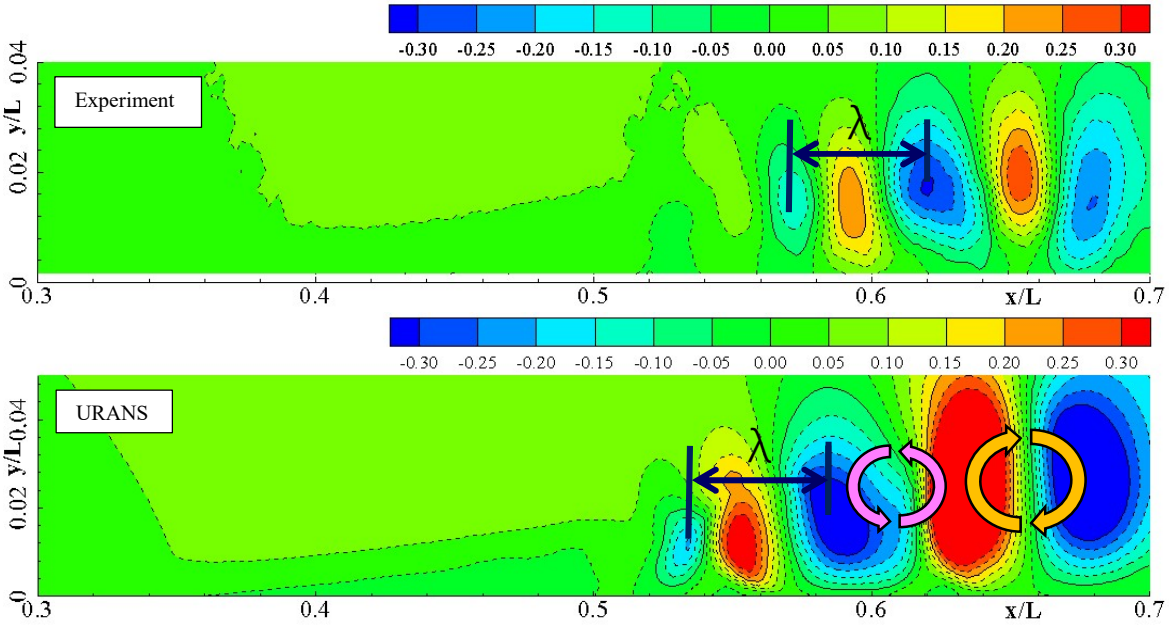

Fig. 5.26 – Instantaneous normalized velocity (v/U_0) distribution Re=150000 Tu=1.5%

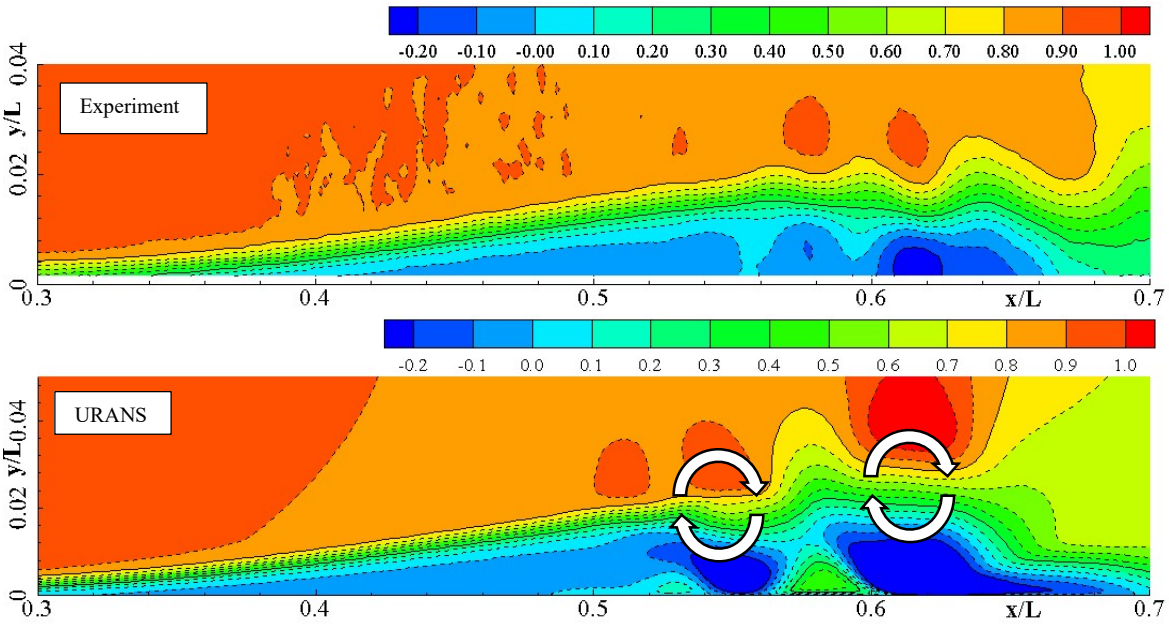

Fig. 5.27 – Instantaneous normalized velocity (u/U_0) distribution Re=150000 Tu=1.5%

Fig. 5.27 gives the instantaneous velocity maps of component u, which should be compared with time-averaged results, both RANS and experiment (Fig. 5.7). Several cores with reverse velocity component u are illustrated in these contour maps, not only in the detachment section but also in the reattachment section. Look at the dark blue reverse core that locates from x/L=0.6 to x/L=0.63 in the URANS sub-figure, it is induced by the K-H roll-up, and travels downstream along the plate. Above each reverse velocity u kernel, a higher velocity area is accompanied with it, moving downstream together. However, the significant differences compare with time-mean flow reveals the unsteady progress of LSB in a point view of dynamics.

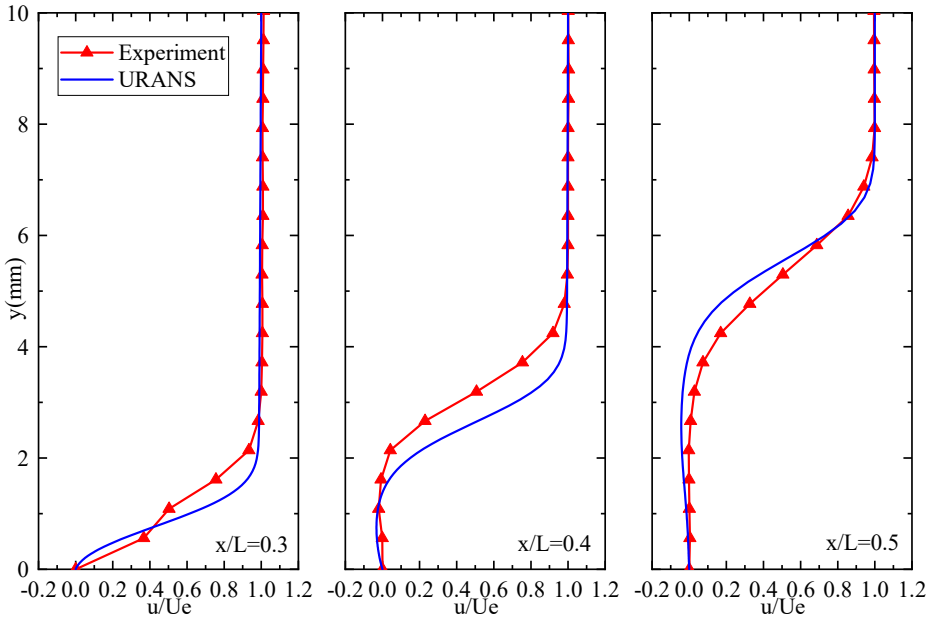

(a) $\bar{u}/U_e$ distribution comparison

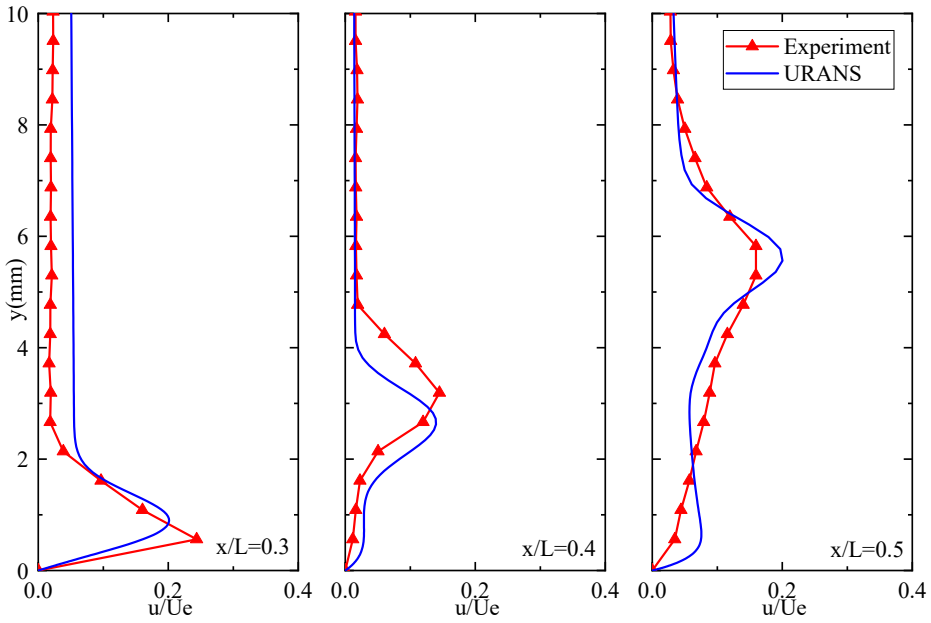

(b) u'_{rms}/U_e distribution comparison

Fig. 5.28 – Velocity profile in the forepart of LSB (Re=150000 Tu=1.5%)

According to the comparisons from Fig. 5.25 to Fig. 5.27, it can be found that the LSB dynamic behavior obtained by URANS is highly coincidence with the experimental one. In the developing period, both the same detachment and maximum thickness positions of LSB can be observed comparing with time-mean results, also accompany with the similar growth rate of the separation bubble thickness, which means the identical behavior of the separated shear layer. In order to verify this point, in the growth part (the front part of LSB), a number of characteristic sections perpendicular to the plate wall are selected (the selection of position is combined with the reference to the RANS results), both time-mean value $\bar{u}$ and root mean square of fluctuation component u'_{rm} on these sections are compared. Among them, the statistical data of URANS comes from 10 continuous pulsation periods with relatively stable periodicity after the convergence of calculation, which avoids the possible impact of the undesired data fluctuation. The calculated results of typical case are plotted as Fig. 5.28, which respectively give the comparisons of the average value distribution and the root mean square fluctuation distribution of the stream-wise velocity u in the statistical range. The freestream velocity Ue, out of boundary layer at each section, is taken as reference during the normalized processing. In general, the velocity profiles of each position do have a high degree of consistency and show a good similarity. In particular, the calculated root mean square distribution of the fluctuating velocity, both in the magnitude of the value and the position of the peak value in the vertical direction, is in good agreement with the experiment. As described by Simoni et al. [72], the root mean square peak value of the fluctuation velocity u at each section, stands for the position of the velocity profile inflection point. With the moving forward of flow, the vertical coordinate of the inflection point gradually grows up, corresponding to the increase of LSB thickness. However, the high agreement between the simulation curves and the experimental ones indicates that the URANS calculation strategy adopted in the present thesis is reasonable and feasible for the prediction of the upstream boundary of LSB. At the same time, it must be noted that the structure of large-scale vortices obtained by URANS is stronger than that of experimental ones. It is not only reflected in the geometric range of vortex, but also has stronger downstream propagation ability, which is one of the characteristics of URANS different from LES and DNS. Considering the insensitivity of URANS to small-scale vortices and the strong randomness of vortex structure shedding process, the dynamic characteristics of LSB reattachment and downstream need to be quantitatively analyzed by other methods, such as the vorticity distribution and frequency analysis adopted in the following sections.

5.6.3 Vortex shedding procedure

In continuum mechanics, the vorticity is a pseudo-vector field that describes the local spinning motion of a continuum near some point, as would be seen by an observer located at that point and traveling along with the flow. For URANS simulation, it can highlight the vortex structure and shedding phenomenon during the post-processing of LSB. Fig. 5.29 illustrates the snapshots of vorticity distribution on three consecutive time steps in a single fluctuation cycle under typical conditions (Re=150000, Tu=1.5%), forming a similar animation. The core position of the vortex structure is tracked by a red dotted line to reflect its dynamic process. At the beginning of the continuous process represented by the first picture under case Re150000-Tu1.5% in Fig.5.29, the end of the free shear layer (the relatively high value area of vorticity) begins to appear a cat-eye-like concentrated area, which becomes the starting point of the subsequent roll-up. At the following moment, the range of the concentrated area gradually increases and separates from the shear layer until an independent circular area is formed. Dashed lines are faired manually between each center

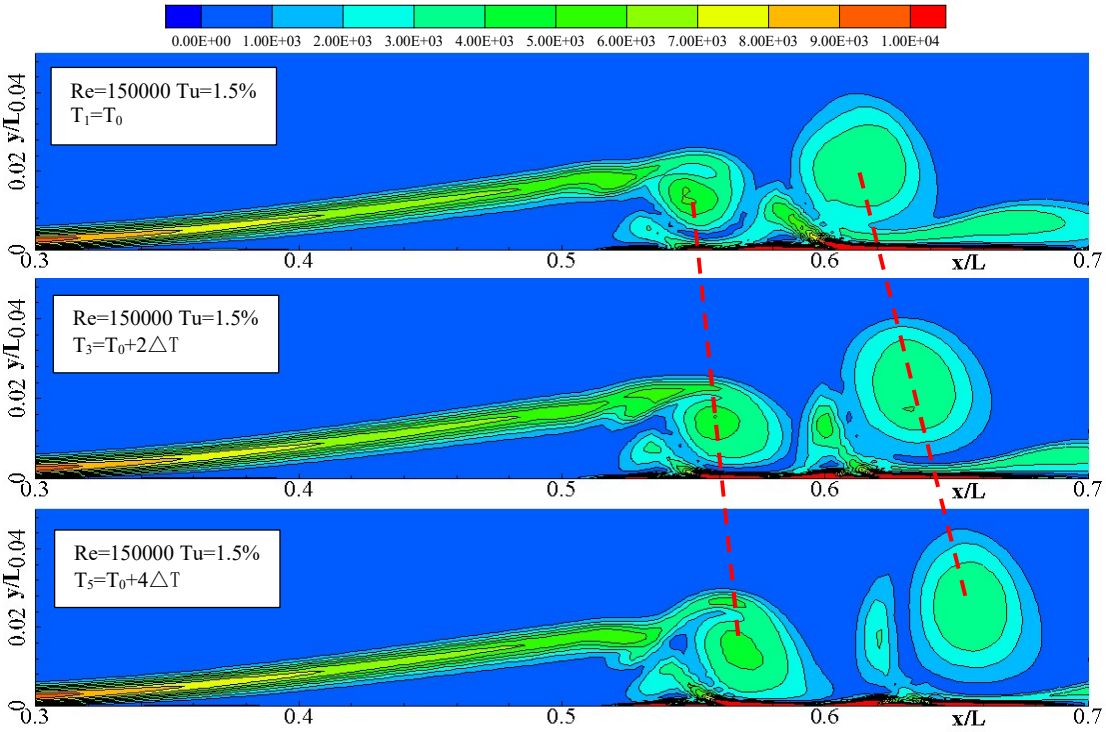

Fig. 5.29 – Time-dependent instantaneous vorticity fields comparison

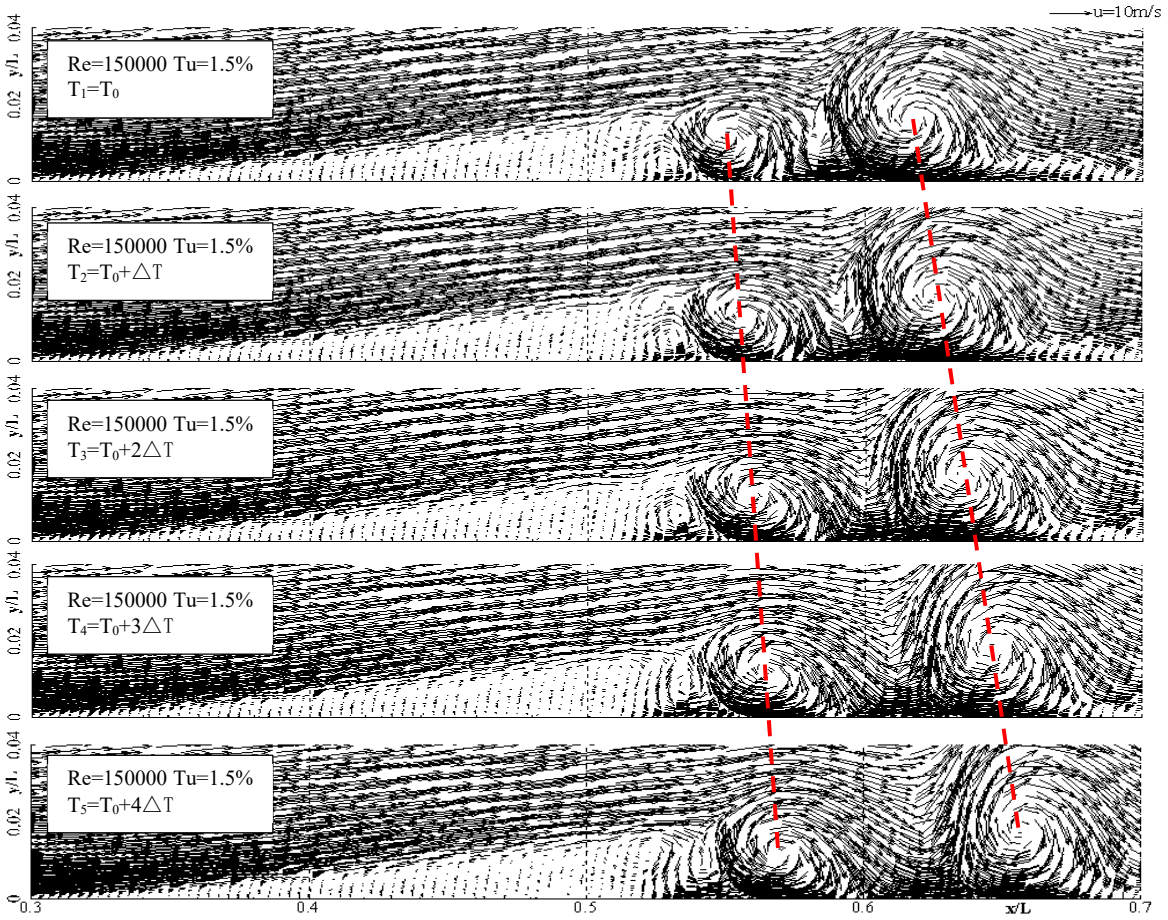

Fig. 5.30 – Time-dependent instantaneous velocity vector (u, v) distribution

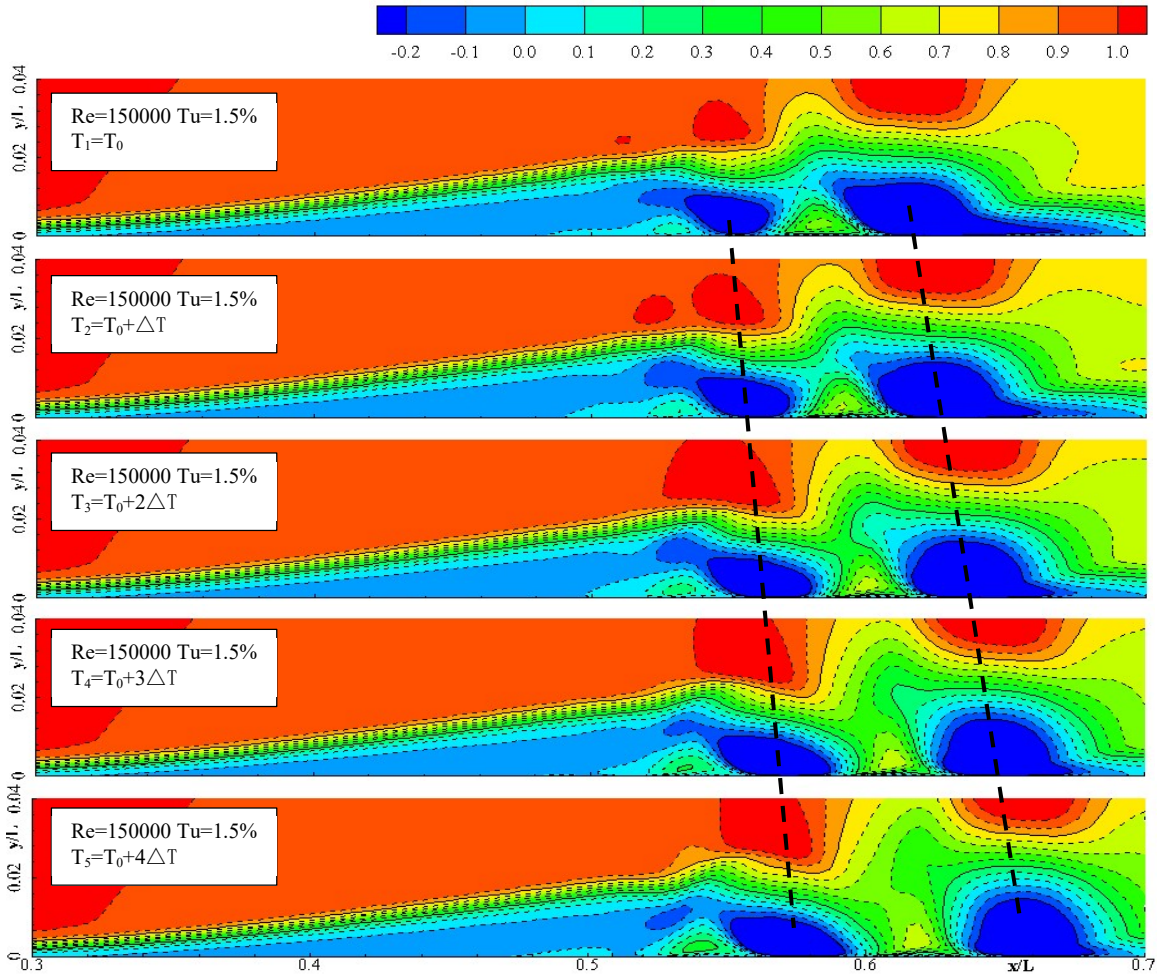

Fig. 5.31 – Time-dependent normalized velocity (u/U_0) distribution

of the eye pattern area in the subsequent frames as a means of following their stream-wise development. Connecting the development and change of two adjacent vorticity structures, we can find that vorticity has undergone a process of gradual enhancement and attenuation in their respective transition regions.

Fig. 5.30 to Fig. 5.32 illustrate the instantaneous velocity vector, normalized velocity distribution at five different time steps within one vortex shedding cycle, respectively, to explain further details on the time stepping procedure. In the velocity vector field shows in Fig. 5.30, the vortex center structure moving along the plate can also be observed after the maximum displacement thickness position, with the same development regulation comparing to the vorticity distribution. Around the x/L=0.52 position, it can be observed that K-H instability gradually increases and finally forms a shedding vortex. From the results of multiple stable calculation periods, this process appears repeatedly, which shows that the shedding vortex has typical periodic characteristics.

In the flow process described in Fig. 5.31, at the cross-section (x/L=0.54) where the shedding vortex occurs, the positive and negative extremum regions of horizontal velocity onset in pairs, developing parallel along the plate with the same speed, indicating that they correspond to the same shedding vortex, with gradually increasing area. In the process of Fig. 5.32, at the position of x/L=0.52, the longitudinal velocity extremum region begins to appear alternately, and propagates stably to the downstream, highlighting the interval characteristics of clockwise and counter-clockwise vortex.

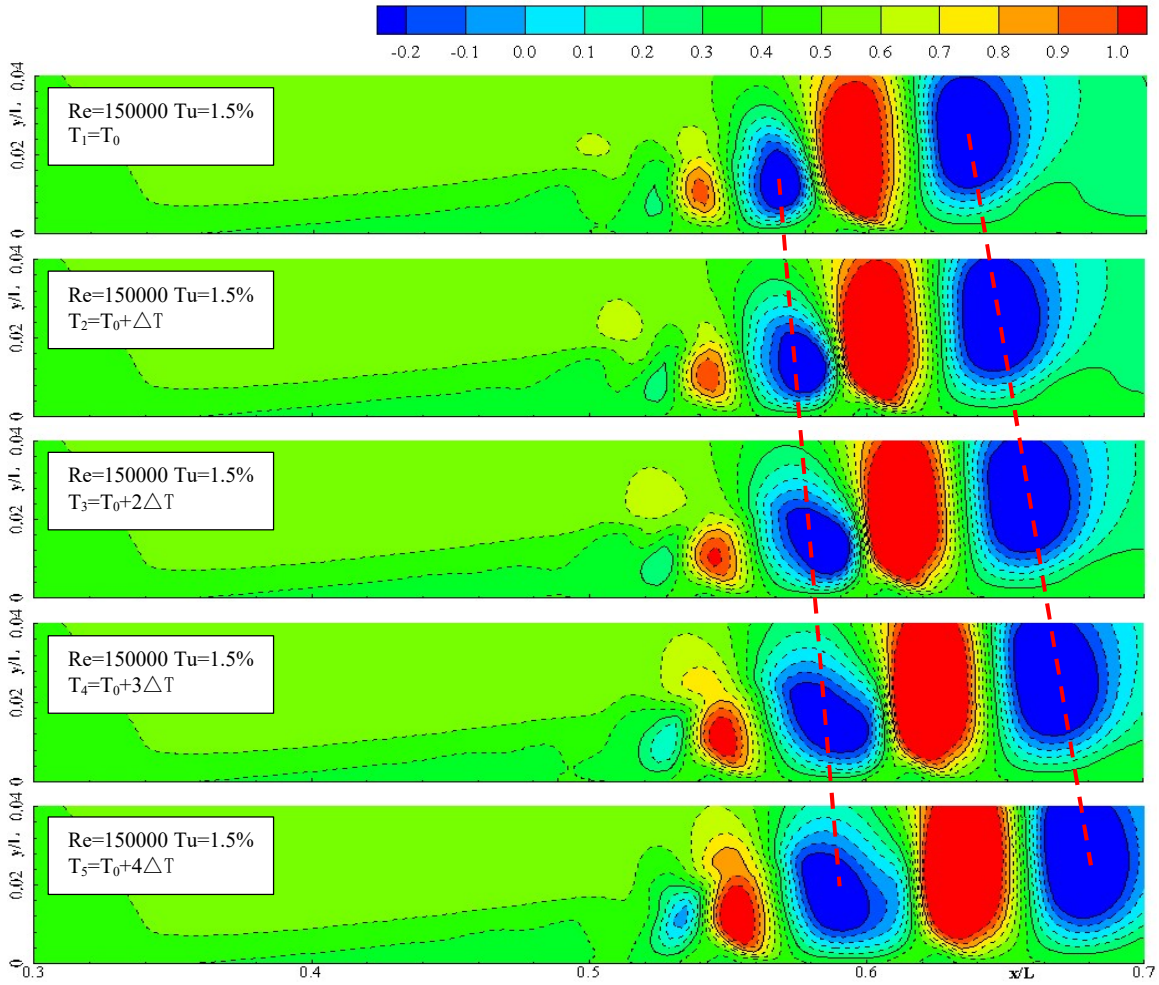

Fig. 5.32 – Time-dependent normalized velocity (v/U_0) distribution

5.6.4 The influence of flow parameters

In order to systematically analyze the influence of flow parameters on the dynamic characteristics of the flat plate LSB, the time-dependent numerical simulation is investigated under nine typical cases combined with three turbulence intensity and three Reynolds number conditions respectively, as shown in Tab. 5.10, while the fixed D12-7 condition was adopted as APG. Four previous typical flow parameters are compared in details from Fig. 5.33 to Fig. 5.36. It can be seen that with the increase of Reynolds number and turbulence intensity, the influence area of LSB shrinks obviously, including the distribution range both of upstream shear stress layer and downstream shedding vortex. The largest influence area of time-dependent LSB is at the condition of Re = 1500000 and Tu = 1.5%, while the smallest one is at the condition of Re=220000 and Tu = 2.8%. With the fixed APG, the detachment position of LSB shifts marginally, while the initial position of the shedding vortex (corresponding to the maximum displacement thickness of the time-averaged result) gradually moves upstream. These characteristics are consistent with the time-averaged results. Comparatively speaking, the effect of the increase of Reynolds number on the separation zone is obviously greater than that of the free-stream turbulence intensity.

The comparison of vorticity distribution under different cases is to observe the effect of flow parameters on the dynamic characteristics of the shedding vortex. Firstly, the vorticity distributions under the same Reynolds number (every single row in Fig. 5.33) show that they

have similar shear layers, including the similar distribution scope and value range. When the Reynolds number is increased, the shear layer shifts closer to the wall. At the same time, the initial position of vortex structure moves forward from x/L=0.54 at Re=70000 condition. When Re takes value of 150000, the range and position of the shear layer are both in the middle level, and the initial position of the vortex structure is about x/L=0.52, which shows that when the high Reynolds number reduces the area of laminar separation bubble in the mean flow field, the K-H instability also moves upstream. When Reynolds number takes 220000, the initial point of vortex structure reaches at x/L =0.48. These changes indicate that the high Reynolds number makes the K-H instability move upstream while reducing the LSB region of the time-averaged flow field. However, the influence of turbulence intensity is weaker than that of Reynolds number. These results show that the transition caused by laminar separation is mainly affected by the Reynolds number of flows in a fixed APG condition. As the increment of Re, the vortex shedding is further confined to the area near the wall, and the vorticity intensity decreases downstream. This phenomenon is similar to the results of literature [103-106].

Tab. 5.10 – Range of URANS simulation conditions in APG D12-7

Re	70000, 150000, 220000
Tu	1.5%, 2.0%, 2.8%

It can also be seen from the comparison of Fig. 5.33 to Fig. 5.36 that the variation of flow parameters can also affect the size and falling rhythm of the shedding vortex structure. In general, the increase of Reynolds number and turbulence intensity can reduce the geometric scale of vortex structure and enlarge the shedding frequency at the same time. Similarly, these changes are more affected by Reynolds number than turbulence intensity does. In Tab. 5.11, the spatial wavelengths of the vortex shedding under the above conditions are calculated (the horizontal interval between two adjacent vortices of the same rotation in Fig. 5.35). It can be seen that the effect of Reynolds number is greater than that of turbulence intensity does, and the wavelength decreases with the increase of flow parameters. At a fixed Reynolds number, the spatial wavelength has no significant change with the increase of turbulence intensity.

Tab. 5.11 – Spatial wavelength (m) comparison of URANS Results (D12-7)

	Tu=1.5%	Tu=2.0%	Tu=2.8%
Re=70000	0.024	0.024	0.026
Re=150000	0.015	0.016	0.018
Re=220000	0.010	0.012	0.012

Five combined cases are selected in order to analyse the influence of flow parameters to shedding vortex frequency, as shown in Tab. 5.12. Simoni et al. [95] proposed that v-based kernel can highlight the dynamic characteristics of K-H rolling up of shedding vortex in the study of LSB dynamic characteristics by POD method. Hereby, in URANS calculation, the v-component velocity of reference point is selected to record continuously for the sake of forming time domain signal, and then FFT is used to analyse its spectrum. The monitoring point is set up at just downstream of first shedding vortex (with exact coordinates in Tab. 5.12). The acquisition of time-domain signal is also started after obtaining stable periodic

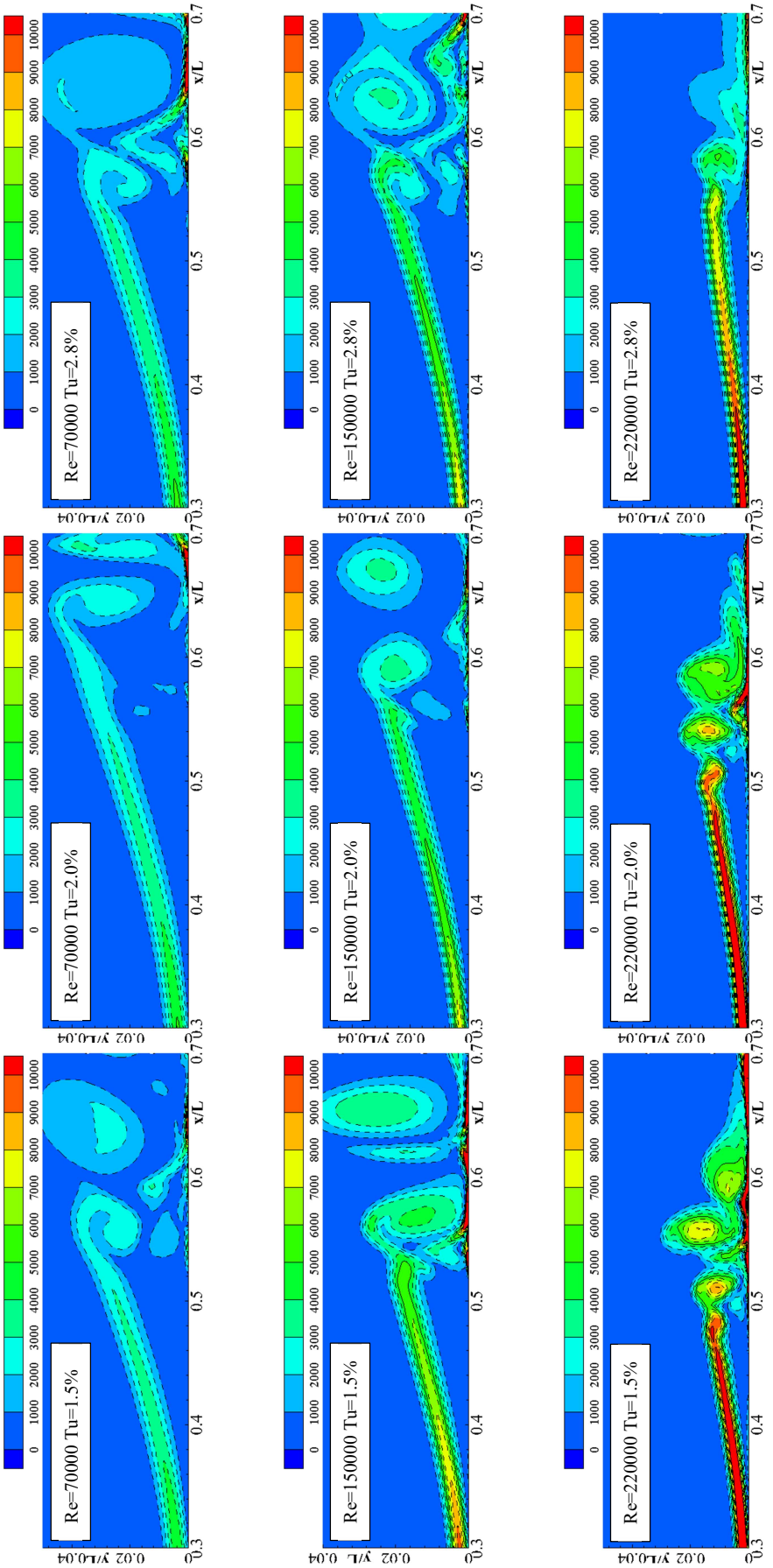

Fig. 5.33 – Comparison of vorticity(1/s) (URANS)

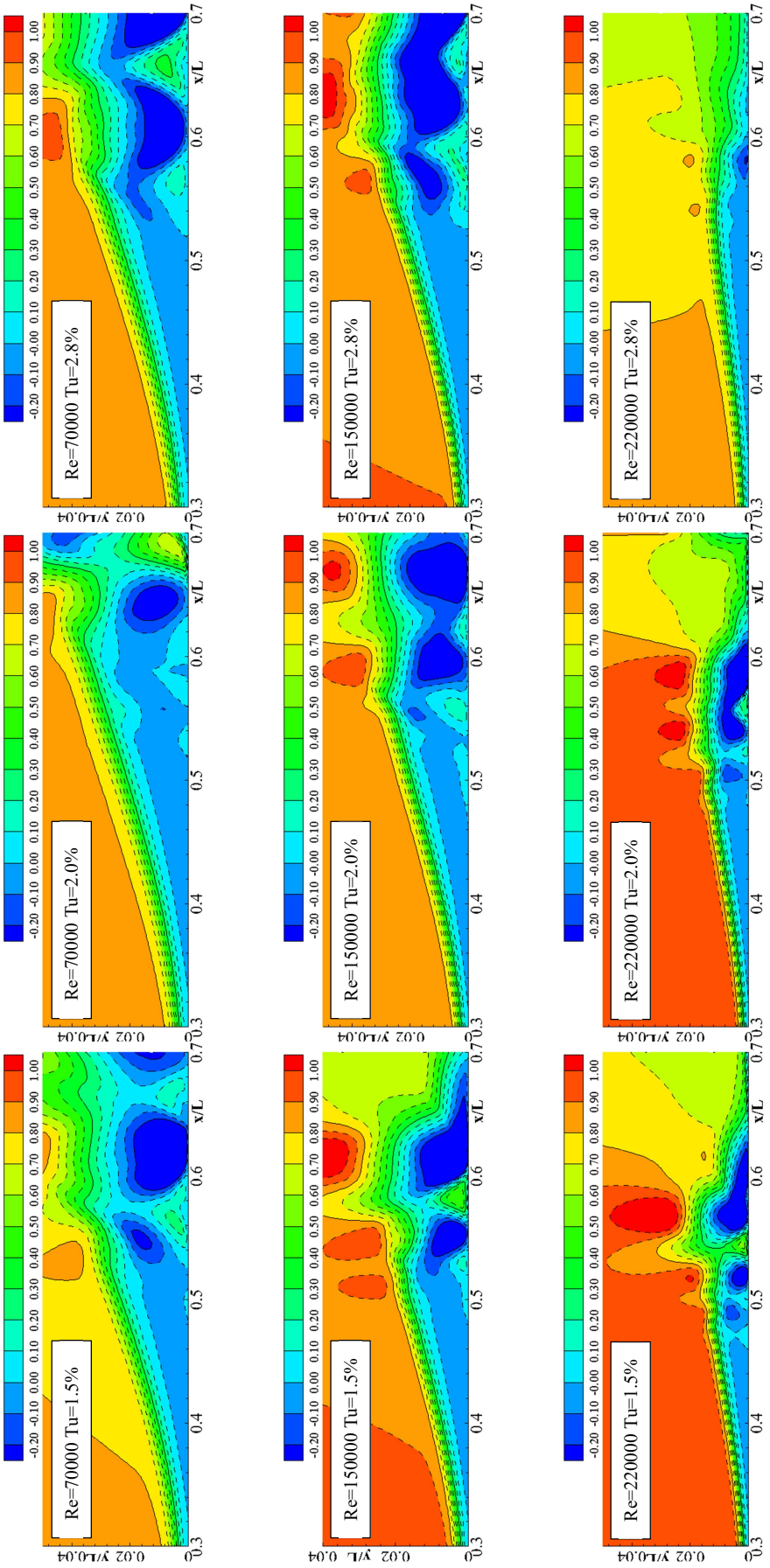

Fig. 5.34 – Comparison of normalized velocity component u/U_0

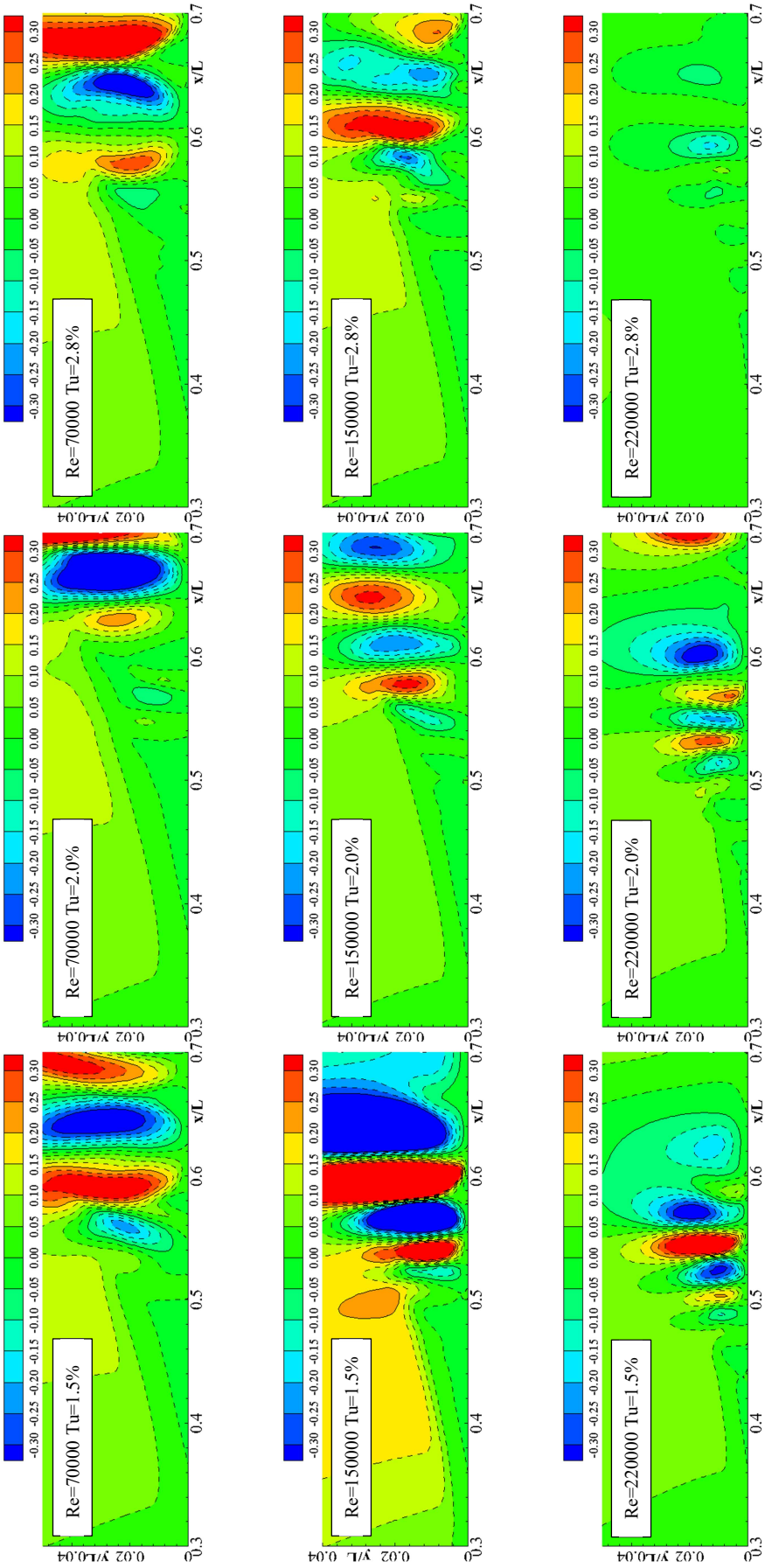

Fig. 5.35 – Comparison of normalized velocity component v/U_0

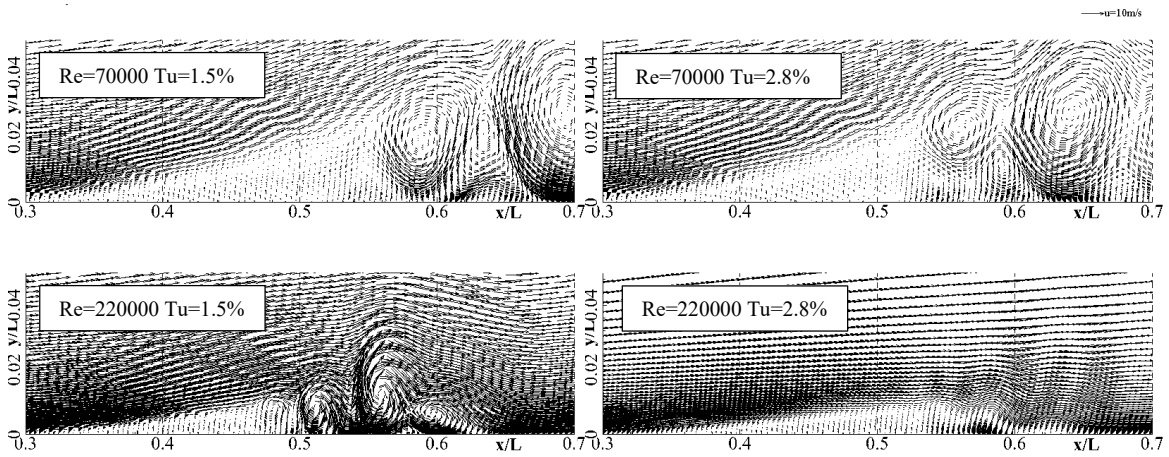

Fig. 5.36 – Velocity vector comparison

solution under each simulation condition. All of the calculation process includes 100-250 oscillation periods, corresponding to 5000 sampling points. The obtained frequency-domain signals are compared with Power Spectral Density, and the results are arranged as Fig. 5.37, while the dominant frequency obtained through analysis is compared with the experimental data under various working conditions, which is arranged as Tab. 5.12.

In Fig. 5.37, each curve has a prominent peak value in the process of gradually increasing frequency, that is, the dominant frequency of vortex shedding process. This peak frequency is obviously affected by the variation of Reynolds number. When the Reynolds number increases gradually, it raises from 71 Hz to 578 Hz, which means that more and smaller shedding vortices develop to the downstream per unit-time, while the dominant frequency range belongs to the typical K-H vortices [98, 107]. In each curve, the value of power density corresponding to the low-frequency component which less than the dominant frequency is also slightly higher than that of the high-frequency component. Beyond the peak frequency, the higher frequency component takes the smaller power density value. For example, when the frequency range exceeds 1000, its power density differs the peak value by more than four orders of magnitude. Compared in the low-frequency region (f<100 Hz), the ordinate value of the curve with Re70000 is larger than that of Re150000 and Re220000, which also shows that the oscillation phenomenon of low-frequency component accounts for the main proportion at low Reynolds number. In addition, there are relatively small peaks near the dominant frequency of each curve, i.e. sub and higher-order harmonic described in reference [72, 77, 108]. Higher-order harmonics are typically due to the saturation process, which implies nonlinearities that excite higher frequencies within the flow. While subharmonics are due to a vortex pairing phenomenon. The data in Tab. 5.12 shows that the dominant frequency obtained by URANS is in good agreement with the experimental results, which verifies the adaptability of the calculation strategy to capture the dynamic process of the vortex shedding downstream of the separation bubble. It should also be noted that in the curve Re=220000, there are two power density values close to the dominant frequency, however, they are still in the same order of magnitude as the experimental results.

Fig. 5.38 compares the frequency of shedding vortex with varied turbulence intensity when the Reynolds number equals to 150000. The acquisition points are also listed in Tab 5.12. It is found that there is no significant discrepancy in the frequency characteristics under the three conditions, neither essential difference in the frequency range distribution nor dominant frequency exists.

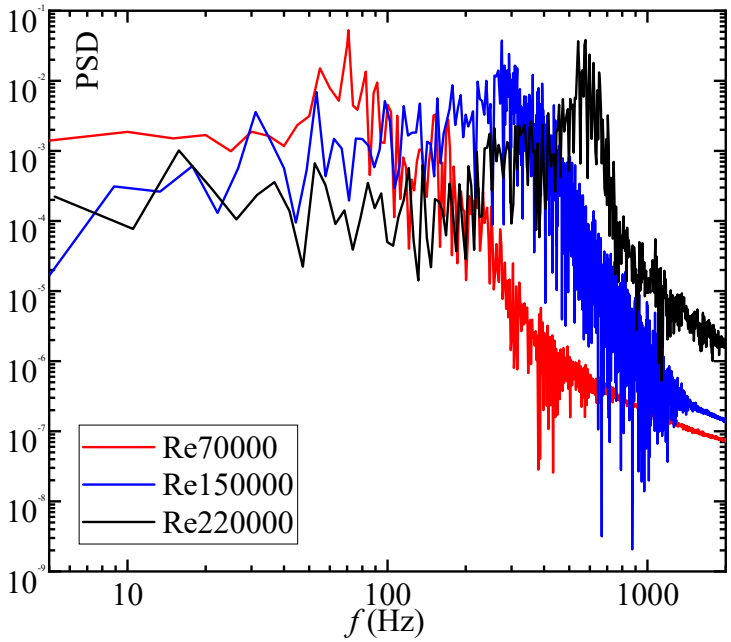

Fig. 5.37 – FFT of velocity v at reference point (Tu=1.5%)

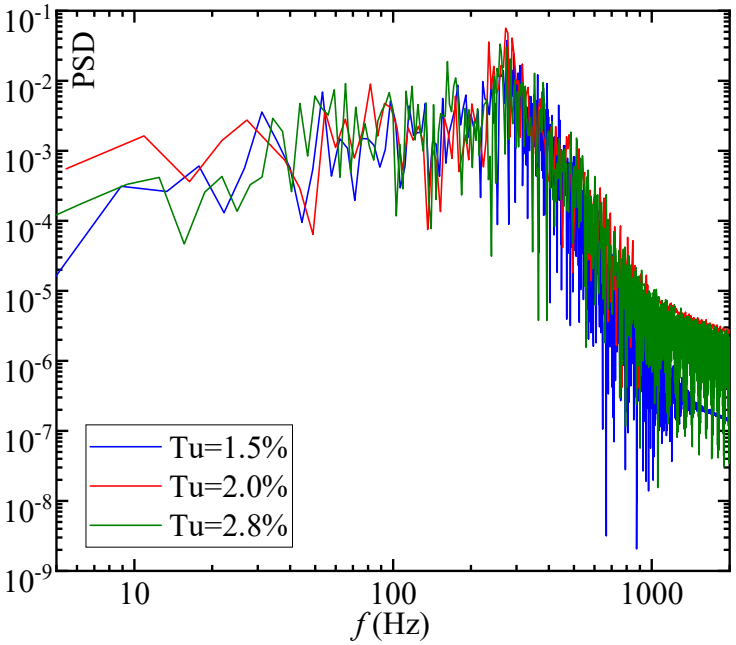

Fig. 5.38 – FFT of velocity v at reference point (Re=150000)

Tab. 5.12 – Dominant frequency (Hz) comparison in condition Tu=1.5%

case		frequency		coordinate of reference point	
Re	Tu	experiment	URANS	x/L	y/L
70000	1.5%	75	71	0.65	0.029
150000	1.5%	280	276	0.59	0.017
150000	2.0%	258	278	0.61	0.023
150000	2.8%	266	258	0.62	0.027
220000	1.5%	550	541/578	0.51	0.010

Tab. 5.13 – Vortex shedding parameters comparison of URANS Results (D12-7)

Re	Tu (%)	λ_0 (m)	f_0 (Hz)	C_0 (m/s)	U_e (m/s)	C_0/U_e
70000	1.5	0.024	71	1.70	3.74	0.46
150000	1.5	0.015	276	4.14	7.96	0.52
150000	1.5	0.013 (EX)	280 (EX)	3.64 (EX)	7.14 (EX)	0.51 (EX)
220000	1.5	0.010	541	5.41	11.64	0.46
150000	2.0	0.016	278	4.45	7.92	0.56
150000	2.8	0.018	258	4.64	8.02	0.58

In order to further compare the influence of flow parameters on the dynamic characteristics of LSB, the spatial wavelength, dominant frequency, propagation velocity and dimensionless velocity of vortex shedding under the above five conditions are compared in Tab. 5.13, also the typical experiment data is listed as reference case. The results show that the spatial wavelength and dominant frequency of vortex shedding are mainly affected by the flow Reynolds number: the higher Reynolds number leads to the reduction of spatial wavelength and the increment of vortex shedding frequency; turbulence intensity affects the spatial wavelength and frequency marginally; according to the production of wavelength and frequency, the dimensionless velocity of vortex shedding propagation has the same magnitude when the APG is fixed, and its value ranges within 0.5 ± 0.1. This situation is consistent with the law given by Simoni [95].

5.6.5 The difference between RANS and URANS simulation

Conceptually speaking, although RANS is a static averaging method, it is not based on spatial averaging, but on an appropriate temporal one. The key point is that the solution variables in the instantaneous (exact) Navier-Stokes equations are decomposed into the mean value (ensemble-averaged or time-averaged) and fluctuating components. For time-dependent or quasi-periodic flows, an URANS simulation must be carried out in one cycle to compare with time-averaged data. Although the URANS has time-dependence and large eddy structure, it is not a simulation of turbulence, but a simulation of its statistical characteristics. In the calculation procedure, the choice of time interval determines the difference between the two processes. As described in section 5.6.1, this is because the calculation in each unstable time step is the instantaneous response to the flow small disturbance. It is also found that within the same time interval, the increase of the iteration number stabilizes the response to small disturbance, which makes the unsteady process tend to become a statistical averaging one.

The process of LSB flow in a flat plate has both time-averaged and time-dependent characteristics, which correspond to the RANS and URANS results, respectively. The results of time-averaged statistics show that the LSB has an obvious closed outline, and the velocity profile has typical turbulent distribution characteristics after the reattachment; for the time-dependent results, when the shear stress layer develops to a specific plate position, an obvious K-H instability appears, then shedding vortex propagates to the downstream of the separation zone. This is explained by comparing the plate pressure coefficient distributions. As shown in Fig. 5.39, the steady and unsteady dimensionless pressure coefficient distributions with fixed turbulence intensity and two Reynolds numbers conditions are compared. Generally speaking, the pressure distribution can be roughly divided into two parts, which is based on the maximum value of shape factor under their respective conditions.

Before the maximum positions, the pressure distribution trends are consistent, which means the development of shear stress layer has no obvious difference downstream of the same separation point; near the maximum position of the shape factor, the pressure distribution of the unsteady results begins to fluctuate, corresponding to the appearance of K-H instability. With the development of the flow, the pressure fluctuation becomes more obvious and transfers along the plate downstream. The maximum positions of shape factor and displacement thickness of time-averaged flow field result in case Re150000 Tu1.5% are illustrated as reference.

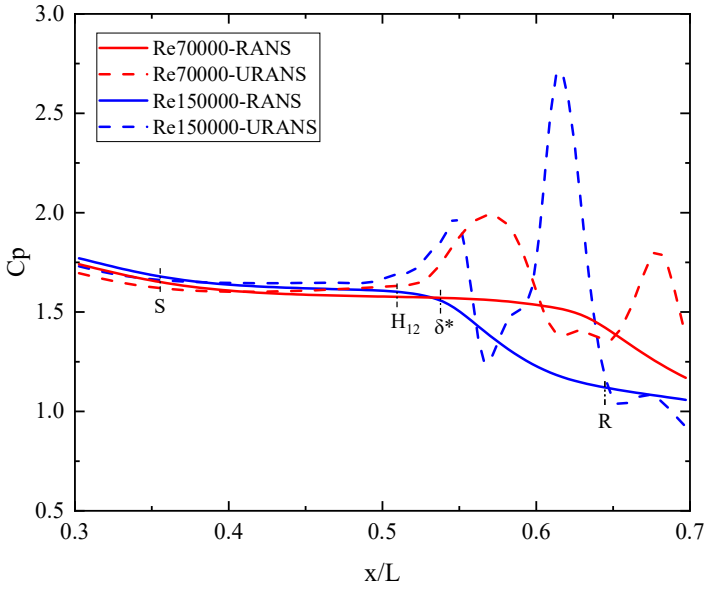

Fig. 5.39 - Cp comparison of RANS and URANS cases (D12-7 Tu1.5%)

By the previous comparison, it can be seen that both of the two calculation strategies make reasonable prediction for the development of shear stress layer of LSB, but the transition position obtained by URANS is prior to that obtained by RANS. In addition, each characteristic position can be quantified in the time-averaged results, such as the maximum displacement thickness and reattachment point, they are meaningful in the LSB prediction of overall characteristics; on the other hand, the time-dependent results highlight the dynamic process and relevant information of shedding vortex, finally, the dynamic characteristics, such as PSD analysis et al. are available. The combination of the two calculation strategies has an effectively ability to predict the overall and dynamic behavior of LSB on flat plate with APG condition.

5.7 Summary

In this chapter, LSB is systematically studied with numerical method and compared with typical experimental results. The time-averaged flow field and transient flow field of LSB are simulated by RANS and URANS respectively, then the kinematic and dynamic characteristics of LSB are analyzed. Therefore, the influence of flow parameters on the overall behavior characteristics of LSB and the transition caused by flow separation are obtained. The applicability and limitation of the turbulence model with transition criterion for LSB problems are verified by the research, and the rationality of the numerical simulation strategy for calculating LSB problems is verified. The results show that the turbulence model based on the transition criterion is suitable for predicting LSB behavior under the adverse

pressure gradient environment, and can effectively give the dynamic characteristics of large-scale vortex shedding with detailed information of time-stepping. Among all the flow parameters, Reynolds number has the most significant effect on the LSB. Increasing the flow parameters (whether Reynolds number or turbulence intensity) has a positive effect on shortening the laminar separation process. With a fixed APG condition, the shorter wavelength and higher dominant frequency of shedding vortex will be induced due to the increment of flow parameters, while the normalized group velocity remains within a stable value range. By the combined Reynolds averaged simulation (time-averaged and time-dependent), the statistical and dynamic characteristics of LSB on flat plate with APG condition could be systematically predicted.

Chapter 6

Conclusions

Based on the time-averaged experiments and steady numerical simulations, a combined investigation about laminar separation bubble on flat plate with adverse pressure gradient is carried out, hence the effects of Reynolds number, turbulence intensity and adverse pressure gradient on the overall behavior of laminar separation bubble in time-averaged flow field are obtained. In summary, the variations of Reynolds number and turbulence intensity have marginal effect on the detachment position of LSB, but obviously have influence on the shape and characteristic parameters of LSB, such as bubble extension and maximum thickness. Increasing the opening angle of the end-wall, the detachment position moves upstream, and the length of LSB decreases, which indicates a shorten process of transition from laminar to turbulent. For the condition of fixed APG, Reynolds number and turbulence intensity mainly influence the shape of LSB, Reynolds number provides the greatest influence than turbulence intensity in modifying the LSB. The integral parameters, such as displacement thickness, momentum thickness, shape factor and Reynolds number of momentum thickness distributions reveal that they are mainly affected by Reynolds number, while the turbulence intensity only induces minor effects. For all conditions the peak value of shape factor appears earlier than the displacement thickness maximum does, indicating that the transition of LSB begins before the maximum thickness is reached.

The experimental and numerical results are in good agreement with each other, which shows that the simulation scheme with transition criterion Transition k-kl-ω model has an acceptable adaptability for predicting the behavior of LSB. Comparatively speaking, the response of the other two turbulence models, Transition SST and SST k-ω, to the flat plate LSB is weaker than that of the Transition k-kl-ω model. However, the RANS simulation scheme adopted in the thesis has an efficient capability in obtaining the time-averaged flow field characteristics of LSB, especially the influence of flow parameters. Thus, this method is of engineering significance for preliminary rapid prediction of the overall behavior of LSB in time-averaged flow.

In the aspect of unsteady calculation, firstly, according to the frequency of shedding vortex obtained from the experiment, the maximum time step size which can capture the periodic oscillation signal is determined, as an important factor in the formulation of URANS calculation scheme, then the LSB dynamic process under typical conditions is investigated numerically. It shows that the presented URANS scheme possesses the ability to capture the dynamic characteristics of LSB effectively. In the instantaneous velocity vector and components distributions, the fluctuation of separated shear layer caused by K-H instability and the subsequent K-H roll-up phenomenon can be clearly observed. The formation and shedding process of these large-scale vortex structures are consistent with the experimental observations, yet the formation position of the vortex structures is corresponding to the time-averaged flow field. The high amplitude concentrated region formed by Y-direction velocity component has obvious orientation alternating and periodicity. Compared with the stream-wise velocity contour map in time-averaged flow field, it can be found that the reversed-flow region formed in LSB will move downstream along the wall with time, departing and forming the periodic shedding vortex. Similarly, changing of flow parameters will affect the dynamic behavior of LSB. With the increase of Reynolds number and turbulence intensity,

large separation bubbles are transformed into shorter and smaller ones, which means that K-H shedding vortices caused by transition mechanism appear earlier. While the URANS FFT results of Y-direction velocity at downstream point of separated shear layer indicate that the dominant frequency of vortex shedding phenomenon also increases with the increment of Reynolds number, which is in good agreement with experimental ones. At the same time, the higher flow parameters make the shedding vortex confined to the area near the wall to a greater extent, and corresponding to a smaller range of vortex structure. In addition, the increment of Reynolds number and turbulence intensity shortens the shedding vortex wavelength and speeds up the dominant shedding frequency, but remains the group velocity stable in the fixed APG condition. By comparing the results of URANS calculation, it also can be seen that the influence of Reynolds number on the unsteady process of LSB is still greater than that free-stream turbulence intensity does.

Ultimately, the numerical results of RANS and URANS have the capability to capture the plate LSB time-averaged and time-dependent experimental characteristics respectively, however, this indicates that numerical simulation with Reynolds averaged method can be used in engineering to rapidly predict the statistical and dynamic processes of LSB and hence the transition induced.

References

[1] O'Meara M. M., Mueller T. J., 1987, Laminar Separation Bubble Characteristics on an Airfoil at Low Reynolds Numbers, AIAA JOURNAL, VOL.25, No.8, pp.1033-1041.

[2] Jan W., Ulrich S., Rolf R., 2006, Validation of the RANS-simulation of laminar separation bubbles on airfoils, Aerospace Science and Technology, Vol.10, pp.484-494.

[3] Jones L., Sandberg R., Sandham N., 2008, Direct numerical simulations of forced and unforced separation bubbles on an airfoil at incidence, Journal of Fluid Mechanics, Vol.602, pp.175-207.

[4] Gault D. E., 1957, A correlation of low-speed airfoil section stalling characteristics with Reynolds number and airfoil geometry, NACA T.N. 3963.

[5] McCullough G. B., Gault D. E., 1951, Examples of three representative types of airfoil-section stall at low speed, NACA T.N. 2502.

[6] Gaster M., 1969, The Structure and Behavior of Laminar Separation Bubbles, ARC R&M 3595.

[7] Hatman A., Wang T., 1998, Separated Flow Transition. Part 1. Experimental Methodology and Mode Classification, ASME Turbo Expo, June 2-5, Stockholm, Sweden, ASME Paper 1998-GT-461.

[8] Hatman A., Wang T., 1998, Separated Flow Transition. Part2. Experimental Results. ASME Turbo Expo 1998, June 2-5, Stockholm, Sweden, ASME Paper 1998-GT-462.

[9] A. Hatman and T. Wang. Separated Flow Transition. Part3. Primary Modes and Vortex Dynamics. ASME Turbo Expo 1998, June 2-5, Stockholm, Sweden, ASME paper 1998-GT-463, 1998.

[10] Hatman A., Wang T., 1999, A prediction model for separated-flow transition, Journal of Turbomachinery, Vol. 121(3), pp. 594-602.

[11] Mayle R. E., 1991, The role of laminar-turbulent transition in gas turbine engines, ASME J. of Turbomachine, Vol.113, pp. 509-537.

[12] Horton H. P., 1969, A semi-empirical theory for the growth and bursting of laminar separation bubbles, Aeronautical Research Council, C.P. No. 1073.

[13] Thwaites B., 1949, Approximate calculation of the laminar boundary layer, Aero. Q., Vol.14, pp. 61-85.

[14] Stratford B. S., 1959, The prediction of separation of the turbulent boundary layer, Journal of Fluid Mechanics, Vol.5, pp. 1-16.

[15] Carmichael B., 1982, Low Reynolds number airfoil survey, NASA, Report No. NASA-CR-165803.

[16] Lissaman P. B. S., 1983, Low-Reynolds-number airfoils, Annu. Rev. Fluid Mech. Vol.15, pp. 223-240.

[17] Kozlov V. V., 1985, Interrelation of the flow separation and stability, IUTAM symposium, pp. 349-358.

[18] Dovgal A. V., Kozlov V. V., Simonov O. A., 1987, Experiments on hydrodynamic instability of boundary layers with separation, IUTAM symposium, pp.109-130.

[19] Ripley M. D., Pauley L. L., 1993, The unsteady structure of two dimensional steady laminar separation. Phys. Fluids A, Vol.5(12), pp. 3099-3016.

[20] Tatineni M., Zhong X., 1999, A numerical study of low Reynolds number separation bubbles. AIAA paper 99-0523.

[21] Masad J. A., Malik M. R., 1994, On the link between flow separation and transition onset. AIAA paper 94-2370.

[22] Reshotko. E., 1988, Stability and transition of boundary layers, Annual review of fluid mechanics, Vol.8(1), pp.311-349.

[23] Pauley L. L., Moin L. L., Reynolds W. C., 1990, The structure of two-dimensional separation. Journal of Fluid Mechanics, Vol.220, pp. 397-412.

[24] Ripley M. D., Pauley L. L., 2015, Mechanisms of surface pressure distribution within a laminar separation bubble at different Reynolds numbers, Physics of Fluids, Vol.27, 023602

[25] Wilson P. G., Pauley L. L., 1998, Two and three-dimensional large-eddy simulations of a transitional separation bubble. Phys. Fluids, Vol.10(11), 2695.

[26] Alam M., Sandham N. D., 2000, Direct numerical simulation of 'short' laminar separation bubbles with turbulent reattachment. Journal of Fluid Mechanics, Vol.403, pp.223-250.

[27] Spalart P. R., Strelets M. K., 2000, Mechanism of transition and heat transfer in a separation bubble, Journal of Fluid Mechanics, Vol.403, pp.329-349.

[28] Curtis E., Hodson H., Banieghbal M., Denton J., Howell R., Harvey N., 1997, Development of blade profiles for low-pressure turbine applications, Journal of Turbomachinery, Vol.119(3), pp.531-538.

[29] John D. A., 2005, Ludiwig Prandtl's boundary layer, Physics today, Dec., pp. 42-48.

[30] Schlichting H., Gersten K., 2017, Boundary Layer Theory (9^{th} edition), Springer, Germany.

[31] Anderson Jr J. D., 2010, Fundamentals of aerodynamics. Tata McGraw-Hill Education.

[32] Narasimha R., Devasia K., Gururani G., Narayanan M. B., 1984, Transitional intermittency in boundary layers subjected to pressure gradient, Experiments in Fluids, Vol. 2(4), pp. 171-176.

[33] Dick E., Kubacki S., 2017, Transition models for turbomachinery boundary layer flows: A review, International Journal of Turbomachinery, Propulsion and Power, Vol.2(2):4.

[34] Walters D. K., Cokljat D., 2008, A Three-Equation Eddy-Viscosity Model for Reynolds-Averaged Navier–Stokes Simulations of Transitional Flow, Journal of Fluids Engineering, Vol.130, 121401, pp.1-14.

[35] Savill A. M., 1993, Some Recent Progress in the Turbulence Modeling of By-Pass Transition, Near-Wall Turbulent Flows, R. M. C. So, C. G. Speziale, B. E. Launder, eds., Elsevier, Amsterdam, pp. 829-848.

[36] Savill A. M., 2002, By-Pass Transition Using Conventional Closures, Closure Strategies for Turbulent and Transitional Flows, Cambridge University Press, Cambridge, pp. 464-492.

[37] Wilcox D. C., 1994, Simulation of Transition With a Two Equation Turbulence Model, AIAA J., Vol.32, pp.247-255.

[38] Hadzic I., Hanjalic K., 1999, Separation-Induced Transition to Turbulence: Second Moment Closure Modelling, Flow, Turbul. Combust., Vol.63, pp.153-173.

[39] Rumsey C. L., 2006, Apparent Transition Behavior of Widely-Used Turbulence Models, Proceedings of the 36th AIAA Fluid Dynamics Conference, San Francisco, CA, June 5-8, 4, pp.2625-2643.

[40] Van Driest E. R., Blumer C. B., 1963, Boundary Layer Transition, Freestream Turbulence, and Pressure Gradient Effects, AIAA J., Vol.1, pp.1303-1306.

[41] Abu-Ghannam B. J., Shaw R., 1980, Natural Transition of Boundary Layers-The Effects of Turbulence, Pressure Gradient, and Flow History, J. Mech. Eng. Sci., Vol.22, pp.213-228.

[42] Fasihfar A., Johnson M. W., 1992, An Improved Boundary Layer Transition Correlation, ASME Paper No. 92-GT-245.

[43] Praisner T. J., Clark J. P., 2007, Predicting Transition in Turbomachinery-Part I: A Review and New Model Development, ASME J. Turbomach., Vol.129, pp.1-13.

[44] Dhawan S., Narasimha R., 1958, Some Properties of Boundary Layer During the Transition From Laminar to Turbulent Flow Motion, J. Fluid Mech., Vol.3, pp. 418-436.

[45] Greene F. A., Hamilton H. H., 2006, Development of a Boundary Layer Properties Interpolation Tool in Support of Orbiter Return to Flight, Proceedings of the Ninth AIAA/ASME Joint Thermophysics and Heat Transfer Conference, San Francisco, CA, June 5-8, Vol.1, pp.144-160.

[46] Kozulovic D., Lapworth L., 2007, An Approach for Inclusion of a Non-Local Transition Model in a Parallel Unstructured CFD Code, Proceedings of the Fifth Joint ASME/JSME Fluids Engineering Conference, San Diego, CA, July 30-Aug. 2, ASME Paper No. FEDSM2007-37162.

[47] Edwards J. R., Roy C. J., Blottner F. G., Hassan H. G., 2001, Development of a One-Equation Transition/Turbulence Model, AIAA J., Vol.39, pp.1691-1698.

[48] Wang C., Perot B., 2002, Prediction of Turbulent Transition in Boundary Layers Using the Turbulent Potential Model, J. Turbul., Vol.3, N22.

[49] Walters D. K., Leylek J. H., 2004, A New Model for Boundary Layer Transition Using a Single-Point RANS Approach, ASME J. Turbomach., Vol.126, pp.193-202.

[50] Suzen Y. B., Huang P. G., 2000, Modeling of Flow Transition Using an Intermittency Transport Equation, ASME J. Fluids Eng., Vol.122, pp.273-284.

[51] Steelant J., Dick E., 2001, Modeling of Laminar-Turbulent Transition for High Freestream Turbulence, ASME J. Fluids Eng., Vol.123, pp.22-30.

[52] Menter F. R., Langtry R. B., Likki S. R., Suzen Y. B., Huang P. G., Volker S., 2006, A Correlation-Based Transition Model Using Local Variables-Part I: Model Formulation, ASME J. Turbomach., Vol.128, pp.413-422.

[53] Launder B. E., Spalding D. B., 1972, Lectures in Mathematical Models of Turbulence, Academic Press, London, England.

[54] Wilcox D. C., 1993, Turbulence Modeling for CFD, DCW Industries, La Canada, CA.

[55] Menter F. R., 1994, Two-Equation Eddy-Viscosity Turbulence Models for Engineering Applications, AIAA JOURNAL, Vol.32, No.8, pp.1598-1605.

[56] Savill A. M., 1993, Some Recent Progress in the Turbulence Modelling of By-pass Transition, Near-Wall Turbulent Flows, R. M. C. So, C. G. Speziale, and B. E. Launder, eds. Elsevier, New York, pp.583-592.

[57] Savill A. M., 1996, One-Point Closures Applied to Transition, Turbulence and Transition Modelling, IUTAM Summerschool, Stockholm, Sweden, pp.233-268.

[58] Suzen Y. B., Huang P. G., Hultgren L. S., Ashpis D. E., 2003, Predictions of Separated and Transitional Boundary Layers Under Low-Pressure Turbine Airfoil Conditions Using an Intermittency Transport Equation, ASME J. Turbomach., Vol.125(3), pp.455-464.

[59] Menter F. R., Esch T., Kubacki S., 2002, Transition Modelling Based on Local Variables, 5th International Symposium on Turbulence Modeling and Measurements, Mallorca, Spain.

[60] Matsubara M., Alfredsson P. H., 2001, Disturbance Growth in Boundary Layers Subjected to Free-Stream Turbulence, J. Fluid Mech., Vol.430, pp.149-168.

[61] Klebanoff P. S., 1971, Effects of Free-Stream Turbulence on a Laminar Boundary Layer, Bull. Am. Phys. Soc., 16, p.1323.

[62] Jacobs R. G., Durbin P. A., 2001, Simulations of Bypass Transition, J. Fluid Mech., Vol.428, pp.185-212.

[63] Lardeau S., Li N., Leschziner M. A., 2007, Large Eddy Simulation of Transitional Boundary Layers at High Freestream Turbulence Intensity and Implications for RANS Modeling, ASME J. Turbomach., Vol.129, pp.311-317.

[64] Mayle R. E., Schulz A., 1997, The Path to Predicting Bypass Transition, ASME J. Turbomach., Vol.119, pp.405-411.

[65] Volino R. J., 1998, A New Model for Free-Stream Turbulence Effects on Boundary Layers, ASME J. Turbomach., Vol.120, pp.613-620.

[66] Lardeau S., Leschziner M. A., Li, N., 2004, Modeling Bypass Transition With Low-Reynolds-Number Nonlinear Eddy-Viscosity Closure, Flow, Turbul. Combust., Vol.73, pp.49-76.

[67] Walters D. K., Leylek, J. H., 2005, A CFD Study of Wake-Induced Transition on a Compressor-Like Flat Plate, ASME J. Turbomach., Vol.127, pp.52-63.

[68] Rudiger S., Frank O., 2006, Performance and limitations of the unsteady RANS approach, PAMM. Proc. Appl. Math. Mech. Vol.6, pp. 543-544.

[69] Iaccarino G., Ooi A., Durbin P. A., Behnia M., 2003, Reynolds averaged simulation of unsteady separated flow, International Journal of Heat and Fluid Flow 24, pp. 147-156.

[70] Moukalled F., Mangani L., Darwish M., 2016, The Finite Volume Method in Computational Fluid Dynamics, Springer Cham Heidelberg New York Dordrecht London, Switzerland.

[71] Matteo Dellacasagrande, 2019, Experimental study of the boundary layer separation and transition processes under turbine-like conditions by means of advanced post-processing techniques. Ph.D. thesis, Genova University, Italy.

[72] Simoni D., Ubaldi M., Zunino P., 2014, Experimental investigation of flow instabilities in a laminar separation bubble, Journal of Thermal Science, Vol.23(3), pp.203-214.

[73] Marxen O., Henningson D., 2011, The effect of small amplitude convective disturbances on the size and bursting of a laminar separation bubble, Journal of Fluid Mechanics, Vol.671, pp.1-33.

[74] Marxen O., Lang M., Rist U., Wagner S., 2003, A combined experimental/numerical study of unsteady phenomena in a laminar separation bubble, Flow Turbul. and Combust., Vol.71, pp.133-146.

[75] Häggmark C. P., Hildings C., Henningson D. S., 2001, A numerical and experimental study of a transitional separation bubble, Aerospace science and technology, Vol.5(5), pp.317-328.

[76] Yarusevych S., Kawall J. G., Sullivan P. E., 2008, Separated shear-layer development on an airfoil at low Reynolds numbers, AIAA journal Vol.46(12), pp. 3060-3069.

[77] Dovgal A., Kozlov V., Michalke A., 1994, Laminar boundary layer separation: Instability and associated phenomena, Prog. Aerospace Sci., Vol.30, pp.61-94.

[78] Diwan S. S., Ramesh O., 2009, On the origin of the inflectional instability of a laminar separation bubble. Journal of Fluid Mechanics, Vol.629, pp.263-298.

[79] Maucher U., Rist U., Wagner S., 2000, Refined interaction method for direct numerical simulation of transition in separation bubbles, AIAA journal, Vol.38(8), pp.1385-1393.

[80] Lang M., Rist U., Wagner S., 2004, Investigations on controlled transition development in a laminar separation bubble by means of LDA and PIV, Exp. Fluids Vol.36, pp.43-52.

[81] Lang M., Marxen O., Rist U., Wagner S., 2004. A combined numerical and experimental investigation of transition in a laminar separation bubble, Recent Results in Laminar-Turbulent Transition, Springer, pp.149-164.

[82] Volino R. J., 2002, Separated flow transition under simulated low-pressure turbine airfoil conditions: Part 1 mean flow and turbulence statistics, In: ASME Turbo Expo 2002: Power for Land, Sea, and Air, American Society of Mechanical Engineers, pp.691-702.

[83] Yaras M., 2002, Measurements of the effects of freestream turbulence on separation-bubble transition, In: ASME Turbo Expo 2002: Power for Land, Sea, and Air, American Society of Mechanical Engineers, pp.647-660.

[84] Alam, M. and Sandham, N. 2000. Direct numerical simulation of ‘short’ laminar separation bubbles with turbulent reattachment, J. Fluid Mech., Vol.410, pp.1-28.

[85] Michelassi V., Wissink J. G., Rodi W., 2002, Analysis of DNS and LES of flow in a low-pressure turbine cascade with incoming wakes and comparison with experiments, Flow Turbul. and Combust., Vol.69, pp.295-329.

[86] Yang Z., Voke P. R., 2001, Large-eddy simulation of boundary-layer separation and transition at a change of surface curvature, J. Fluid Mech., Vol.439, pp.305-333.

[87] Watmuff J. H., 1999, Evolution of a wave packet into vortex loops in a laminar separation bubble, J. Fluid Mech., Vol.397, pp.119-169.

[88] Häggmark C. P., Hildings C., Henningson D. S., 2001, A numerical and experimental study of a transitional separation bubble, Aerospace science and technology, Vol.5(5):317-328.

[89] NUMECA, User manuals, Academic R&D license, 2019.

[90] Ansys Fluent, Academic R&D license, 2019.

[91] Catalano P., Tognaccini R., 2011, RANS analysis of the low-Reynolds number flow around the SD7003 airfoil, Aerospace Science and Technology, Vol.15, pp.615-626.

[92] Rumsey C.L., Spalart P.R., 2009, Turbulence model behavior in low Reynolds number regions of aerodynamic flow fields, AIAA Journal, Vol.47(4), pp.982-993.

[93] Volino R. J., 2002a, Separated flow transition under simulated low-pressure turbine airfoil conditions: Part 1-mean flow and turbulence statistics, In ASME Turbo Expo 2002: Power for Land, Sea, and Air, pp.691-702.

[94] Ol M. V., McAuliffe B. R., Hanff E. S., Scholz U., Kähler C., 2005, Comparison of laminar separation bubble measurements on a low reynolds number airfoil in three facilities. AIAA paper, 5149(1).

[95] Simoni D., Lengani D., Ubaldi M., Zunino P., Dellacasagrande M., 2017, Inspection of the dynamic properties of laminar separation bubbles: free-stream turbulence intensity effects for different reynolds numbers, Experiments in Fluids, pp.58-66.

[96] Lengani D., Simoni D., Ubaldi M., Zunino P., Bertini F., 2017, Experimental study of free-stream turbulence induced transition in an adverse pressure gradient, Experimental Thermal and Fluid Science, Vol.84, pp.18-27.

[97] Simoni D., Ubaldi M., Zunino P., Ampellio E., 2016, Free-stream turbulence effects on the boundary layer of a high-lift low-pressure-turbine blade, Journal of Thermal Science, Vol.25(3), pp.195-206.

[98] Simoni D., Ubaldi M., Zunino P., Lengani D., Bertini F., 2012, An experimental investigation of the separated-flow transition under high-lift turbine blade pressure gradients, Flow Turbul. and Combust., Vol.88, pp.45-62.

[99] Lardeau S., Leschziner M., Zaki T., 2012, Large eddy simulation of transitional separated flow over a flat plate and a compressor blade, Flow Turbul. and Combust., Vol.88 pp.919-944.

[100] Simoni D., Ubaldi M., Zunino P., 2016, A simplified model predicting the Kelvin-Helmholtz instability frequency for laminar separated flows, Journal of Turbomachinery, Vol.138(4):044501.

[101] Rumsey C. L., Swanson R.C., 2009, Turbulence Modeling for Active Flow Control Applications, International Journal of Computational Fluid Dynamics, vol.23, pp. 317-326.

[102] Dejoan A., Jang Y. J., Leschziner M.A., 2005, Comparative LES and Unsteady RANS Computations for a Periodically Perturbed Separated Flow over a Backward-Facing Step, Journal of Fluids Engineering, Vol.127, pp.872-878.

[103] Counsil J. N. N., Boulama K. G., 2012, Validating the URANS shear stress transport γ-Re™ mode for low-Reynolds-number external aerodynamics, INTERNATIONAL JOURNAL FOR NUMERICAL METHODS IN FLUIDS, Meth. Fluids, Vol.69, pp.1411-1432.

[104] Burgmann S, Brücker C, Schröder W., 2006, Scanning PIV measurements of a laminar separation bubble, Experiments in Fluids, Vol.41, pp.319-326.

[105] Zhang W, Hain R, Kähler C J., 2008, Scanning PIV investigation of the laminar separation bubble on a SD7003 airfoil. Experiments in Fluids, Vol.45, pp.725-743.

[106] Zaki T., 2013, From streaks to spots and on to turbulence: Exploring the dynamics of boundary layer transition. Flow Turbul. and Combust., Vol.91, pp.451-473.

[107] Simoni D., Ubaldi M., Zunino P., 2013, Experimental investigation of the interaction between incoming wakes and instability mechanisms in a laminar separation bubble, Exp. Therm. Fluid Sci., Vol.50, pp.54-60.

[108] Yarusevych, S., Sullivan, P.E., Kawall, J. G., 2009, On vortex shedding from an airfoil in low-Reynolds number flows, J. Fluid Mech., Vol.632, pp.245–271.

[109] Langtry R. B., Menter F. R,. 2009, Correlation-Based Transition Modeling for Unstructured Parallelized Computational Fluid Dynamics Codes, AIAA Journal, Vol.47(12), pp.2894-2906.

Nomenclature

Roman Symbols

C_p	Coefficient of pressure
C_f	Skin friction coefficient
Ex	Experiment data
f	Frequency
H_{12}	Shape factor
k	Kinetic energy
L	Length of plate
M	Maximum thickness of boundary layer
P_{in}^*	Total pressure of domain inlet
P_{out}	Static pressure of the plate end
R	Reattachment position
S	Separation position
U	Mean stream-wise velocity
u	Instantaneous stream-wise velocity
V	Mean normal to the wall velocity
v	Instantaneous normal to the wall velocity
x	Stream-wise coordinate
y	Direction normal to the wall coordinate
y+	Dimensionless wall distance

Greek Symbols

α	Opening angle of the adjustable end-wall
γ	Intermittency function
δ	Boundary layer thickness
δ^*	Displacement thickness
Δt	Time step size
ε	Kinetic energy dissipation rate
μ	Dynamic viscosity
ν	Kinematic viscosity
τ_w	Wall shear stress
θ	Momentum thickness
ϕ	Scalar quantity
ω	Inverse turbulent time scale

Superscripts

’	Fluctuating component
*	Displacement quantity
$\bar{}$	Time-averaged value

Subscripts

∞	Free-stream quantity
e	Local outer layer quantity
T	Turbulent quantity
L	Laminar quantity
0	Testing domain inlet quantity

Acronyms / Abbreviations

APG	Adverse Pressure Gradient
BL	Boundary Layer
CFD	Computational Fluid Dynamics
DNS	Direct Numerical Simulation
FFT	Fast Fourier Transport
HW	Hot Wire
K-H	Kelvin-Helmholtz
LES	Large Eddy Simulation
LDV	Laser Doppler Velocimetry
LSB	Laminar Separation Bubble
N-S	Navier-Stokes
PIV	Particle Image Velocimetry
PSD	Power Spectral Density
RANS	Reynolds Averaged Navier-Stokes
Re	Reynolds number
Re_x	Reynolds number based on the stream-wise coordinate
Re_θ	Momentum thickness Reynolds number
rms	Root Mean Square
SST	Shear Stress Transport
TR	Time Resolved
T-S	Tollmien-Schlichting
Tu	Turbulence intensity
URANS	Unsteady Reynolds Averaged Navier-Stokes

Appendix A:

Transport Equations for the Transition SST model

The transport equation for the intermittency γ is defined as:

$$\frac{\partial(\rho\gamma)}{\partial t}+\frac{\partial\left(\rho U_j\gamma\right)}{\partial x_j}=P_{\gamma1}-E_{\gamma1}+P_{\gamma2}-E_{\gamma2}+\frac{\partial}{\partial x_j}\left[\left(\mu+\frac{\mu_t}{\sigma_\gamma}\right)\frac{\partial\gamma}{\partial x_j}\right] \qquad \text{(A.1)}$$

The transition sources are defined as follows:

$$P_{\gamma1}=C_{a1}F_{len}\quad\rho S[\gamma F_{onset}]^{C_{\gamma3}}$$

$$E_{\gamma1}=C_{e1}P_{\gamma1}\gamma$$

Where S is the strain rate magnitude, F_{length} is an empirical correlation that controls that the length of the transition region, and C_{a1} and C_{e1} hold the values of 2 and 1, respectively. The destruction/relaminarization sources are defined as follows:

$$P_{\gamma2}=C_{a2}\rho\Omega\gamma F_{turb}$$

$$E_{\gamma2}=C_{e2}P_{\gamma2}\gamma$$

Where Ω is the vorticity magnitude. The transition onset is controlled by the following functions:

$$Re_V=\frac{\rho y^2 S}{\mu}$$

$$C=\frac{\rho k}{\mu\omega}$$

$$F_{onset1}=\frac{Re_V}{2193Re_{\theta c}} \qquad \text{(A.2)}$$

$$F_{onset2}=\min\left(\max(F_{on}\quad,F_{onset1}^4),2.0\right)$$

$$F_{on}\quad=\max\left(1-\left(\frac{R_T}{25}\right)^3,0\right)$$

$$F_{onset}=\max(F_{onset2}-F_{onset3},0)$$

$$F_{turb}=e^{-\left(\frac{R_T}{4}\right)^4}$$

Where y is the wall distance and $Re_{\theta c}$ is the critical Reynolds number where the intermittency first starts to increase in the boundary layer. This occurs upstream of the transition Reynolds number $\widetilde{Re}_{\theta t}$ and the difference between the two must be obtained from an empirical correlation. Both the F_{length} and $Re_{\theta c}$ correlations are functions of $\widetilde{Re}_{\theta t}$.
The constants for the intermittency equation are:

$$C_{a1}=2;\ C_{e1}=1;\ C_{a2}=0.06;\ C_{e2}=50;\ C_{\gamma3}=0.5;\ \sigma_\gamma=1.0$$

The transport equation for the transition momentum thickness Reynolds number $\widetilde{Re}_{\theta t}$ is

$$\frac{\partial(\rho\widetilde{Re}_{\theta t})}{\partial t}+\frac{\partial(\rho U_j\widetilde{Re}_{\theta t})}{\partial x_j}=P_{\theta t}+\frac{\partial}{\partial x_j}\left[\sigma_{\theta t}(\mu+\mu_t)\frac{\partial\widetilde{Re}_{\theta t}}{\partial x_j}\right] \quad \text{(A.3)}$$

The source term is defined as follows:

$$P_{\theta t}=C_{\theta t}\frac{\rho}{t}(Re_{\theta t}-\widetilde{Re}_{\theta t})(1.0-F_{\theta t})$$

$$t=\frac{500\mu}{\rho U^2}$$

$$F_{\theta t}=\min\left(\max\left(F_{wake}e^{-\left(\frac{\gamma}{\delta}\right)^4},1.0-\left(\frac{\gamma-1/50}{1-1/50}\right)^2\right),1.0\right)$$

$$\theta_{BL}=\frac{\widetilde{Re}_{\theta t}\mu}{\rho U}$$

$$\delta_{BL}=\frac{15}{2}\theta_{BL}$$

$$\delta=\frac{50\Omega y}{U}\delta_{BL}$$

$$Re_{\omega}=\frac{\rho y^2\omega}{\mu}$$

$$F_{wake}=e^{-\left(\frac{Re_{\omega}}{1E+5}\right)^2}$$

The model constants for the $\widetilde{Re}_{\theta t}$ equation are:

$$C_{\theta t}=0.03;\ \sigma_{\theta t}=2.0$$

The boundary condition for $\widetilde{Re}_{\theta t}$ at a wall is zero flux. The boundary condition for $\widetilde{Re}_{\theta t}$ at an inlet should be calculated from the empirical correlation based on the inlet turbulence intensity.

The model contains three empirical correlations. $Re_{\theta t}$ is the transition onset as observed in experiments. This has been modified from Menter [52] et al. in order to improve the predictions for natural transition. It is used in equation A.3. F_{length} is the length of the transition zone and is substituted in equation A.1. $Re_{\theta c}$ is the point where the model is activated in order to match both $Re_{\theta t}$ and F_{length} and is used in equation A.2. These empirical correlations are provided by Langtry and Menter [109].

$$Re_{\theta t}=f(Tu,\lambda)$$

$$F_{length}=f(\widetilde{Re}_{\theta t})$$

$$Re_{\theta c}=f(\widetilde{Re}_{\theta t})$$

The first empirical correlation is a function of the local turbulence intensity, Tu:

$$Tu = \frac{100}{U}\sqrt{\frac{2}{3}k}$$

Where k is the turbulent energy.
The Thwaites' pressure gradient coefficient λ_θ is defined as

$$\lambda_\theta = (\theta^2/\nu)dU/ds$$

where dU/ds is the acceleration in the stream-wise direction.

Separation-Induced Transition Correction
The modification for separation-induced transition is:

$$\gamma_{sep} = \min\left(C_{s1}\max\left[\left(\frac{Re_V}{3235Re_{\theta c}}\right) - 1{,}0\right]F_{reattch}, 2\right)F_{\theta t} \qquad \text{(A.4)}$$

$$F_{reatt} = e^{-\left(\frac{R_T}{20}\right)^4}$$

$$\gamma_{eff} = \max(\gamma, \gamma_{sep})$$

Here, C_{s1} is a constant with a value of 2.
The model constants in equation A.4 have been adjusted from those of Menter [52] et al. in order to improve the predictions of separated flow transition. The main difference is that the constant that controls the relation between Re_V and $Re_{\theta c}$ was changed from 2.193, its value for a Blasius boundary layer, to 3.235, the value at a separation point where the shape factor is 3.5 [52]. The boundary condition for γ at a wall is zero normal flux, while for an inlet, γ is equal to 1.0.

Coupling the Transition Model and SST Transport Equations
The transition model interacts with the SST turbulence model by modification of the k equation, as follows:

$$\frac{\partial(\rho k)}{\partial t} + \frac{\partial(\rho u_i k)}{\partial x_i} = \frac{\partial}{\partial x_j}\left[\Gamma_k \frac{\partial k}{\partial x_j}\right] + G_k^* - Y_k^* + S_k$$

$$G_k^* = \gamma_{reff}\widetilde{G_k}$$

$$Y_k^* = \min(\max(\gamma_{eff}, 0.1), 1.0)Y_k$$

where $\widetilde{G_k}$ and Y_k are the original production and destruction terms for the SST model. Note that the production term in the ω-equation is not modified. The rationale behind the above model formulation is given in detail in Menter et al. [52].

In order to capture the laminar and transitional boundary layers correctly, the mesh must have a y^+ of approximately one. If the y^+ is too large (that is, > 5), then the transition onset location moves upstream with increasing y^+. It is recommended that you use the bounded second order upwind based discretization for the mean flow, turbulence and transition equations.

Appendix B:

Transport Equations for the Transition $k-kl-\omega$ model

The $k-kl-\omega$ model is considered to be a three-equation eddy-viscosity type, which includes transport equations for turbulent kinetic energy (k_T), laminar kinetic energy (k_L), and the inverse turbulent time scale (ω)

$$\frac{Dk_T}{Dt} = P_{k_T} + R + R_{NAT} - \omega k_T - D_T + \frac{\partial}{\partial x_j}\left[\left(\nu + \frac{\alpha_T}{\alpha_k}\right)\frac{\partial k_T}{\partial x_j}\right] \tag{B.1}$$

$$\frac{Dk_L}{Dt} = P_{k_L} - R - R_{NAT} - D_L + \frac{\partial}{\partial x_j}\left[\nu\frac{\partial k_L}{\partial x_j}\right] \tag{B.2}$$

$$\frac{D\omega}{Dt} = C_{\omega 1}\frac{\omega}{k_T}P_{k_T} + \left(\frac{C_{\omega R}}{f_w}\right)\frac{\omega}{k_T}(R + R_{NAT}) - C_{\omega 2}\omega^2 \tag{B.3}$$

$$+C_{\omega 3}f_\omega \alpha_T f_w^2 \frac{\sqrt{k_T}}{d^3} + \frac{\partial}{\partial x_j}\left[\left(\nu + \frac{\alpha_T}{\alpha_k}\right)\frac{\partial \omega}{\partial x_j}\right]$$

The inclusion of the turbulent and laminar fluctuations on the mean flow and energy equations via the eddy viscosity and total thermal diffusivity is as follows:

$$\overline{-u_\iota u_j} = \nu_{TOT}\left(\frac{\partial U_i}{\partial x_j} + \frac{\partial U_j}{\partial x_i}\right) - \frac{2}{3}k_{TOT}\delta_{ij} \tag{B.4}$$

$$\overline{-u_\iota \theta} = \alpha_{\theta,TOT}\frac{\partial \theta}{\partial x_i} \tag{B.5}$$

The effective length is defined as

$$\lambda_{eff} = \min\left(C_\lambda d, \lambda_T\right)$$

Where λ_T is the turbulent length scale and is defined by

$$\lambda_T = \frac{\sqrt{k}}{\omega}$$

and the small scale energy is defined by

$$k_{T,s} = f_{ss}f_w k_T \tag{B.6}$$

$$f_w = \frac{\lambda_{eff}}{\lambda_T}$$

$$f_{ss} = \exp\left[-\left(\frac{C_{ss}\nu\Omega}{k_T}\right)^2\right]$$

The large scale energy is given by

$$k_{T,l} = k_T - k_{T,s} \tag{B.7}$$

Note that the sum of equation B.6 and equation B.7 yields the turbulent kinetic energy k_T.

The turbulence production term generated by turbulent fluctuations is given by

$$P_{k_T} = \nu_{T,s} S^2$$

where the small-scale turbulent viscosity is $\nu_{T,s}$

$$\nu_{T,s} = f_\nu f_{INT} C_\mu \sqrt{k_{T,s}} \lambda_{eff}$$

and

$$C_\mu = \frac{1}{A_0 + A_s(S/\omega)}$$

$$f_\nu = 1 - \exp\left(-\frac{\sqrt{Re_{T,s}}}{A_\nu}\right)$$

A damping function defining the turbulent production due to intermittency is given by

$$f_{INT} = \min\left(\frac{k_L}{C_{INT} k_{TOT}}, 1\right)$$

$$Re_{T,s} = \frac{f_w^2 k_T}{\nu\omega}$$

In equation B.2, P_{k_L} is the production of laminar kinetic energy by large scale turbulent fluctuations, such that

$$P_{k_L} = \nu_{T,l} S^2$$

The large-scale turbulent viscosity $\nu_{T,l}$ is modeled as

$$\nu_{T,l} = \min\left\{\nu_{T,l}^*, \frac{0.5(k_L + k_{T,l})}{S}\right\} \tag{B.8}$$

Where

$$\nu_{T,l}^* = f_{\tau,1} C_{11} \left(\frac{\Omega \lambda_{eff}^2}{\nu}\right) \sqrt{k_{T,l}} \lambda_{eff} + \beta_{TS} C_{12} \varphi_{NAT} d^2 \Omega \tag{B.9}$$

The limit in equation B.8 binds the realizability such that it is not violated in the two-dimensional developing boundary layer. The time-scale-based damping function $f_{\tau,1}$ is

$$f_{\tau,1} = 1 - \exp\left(-C_{\tau,1} \frac{k_{T,l}}{\lambda_{eff}^2 \Omega^2}\right)$$

where β_{TS} from equation B.9 is

$$\beta_{TS} = 1 - \exp\left(-\frac{max\left(\varphi_{NAT} - C_{TS,crit}, 0\right)^2}{A_{TS}}\right)$$

$$\varphi_{NAT} = \frac{d^2 \Omega}{\nu}$$

Near-wall dissipation is given by

$$D_T = 2\nu \frac{\partial\sqrt{k_T}}{\partial x_j}\frac{\partial\sqrt{k_T}}{\partial x_j}$$

$$D_L = 2\nu \frac{\partial\sqrt{k_L}}{\partial x_j}\frac{\partial\sqrt{k_L}}{\partial x_j}$$

In equation B.1 to equation B.3, R represents the averaged effect of the breakdown of stream-wise fluctuations into turbulence during bypass transition:

$$R = C_R \beta_{BP} k_L \omega / f_w$$

β_{BP}, which is the threshold function controls the bypass transition process:

$$\beta_{BP} = 1 - \exp\left(-\frac{\varphi_{BP}}{A_{BP}}\right)$$

$$\varphi_{BP} = \max\left[\left(\frac{k_T}{\nu\Omega} - C_{BP,crit}\right), 0\right]$$

The breakdown to turbulence due to instabilities is considered to be a natural transition production term, given by

$$R_{NAT} = C_{R,NAT}\beta_{NAT} k_L \Omega$$

$$\beta_{NAT} = 1 - \exp\left[-\frac{\max\left(\varphi_{NAT} - \frac{C_{NAT,crit}}{f_{NAT,crit}}, 0\right)}{A_{NAT}}\right]$$

$$f_{NAT,crit} = 1 - exp\left(C_{NC}\frac{\sqrt{k_L}d}{\nu}\right)$$

The use of ω as the scale-determining variable can lead to a reduced intermittency effect in the outer region of a turbulent boundary layer, and consequently an elimination of the wake region in the velocity profile. From equation B.3, the following damping is defined as

$$f_\omega = 1 - exp\left[-0.41\left(\frac{\lambda_{eff}}{\lambda_T}\right)^4\right]$$

The total eddy viscosity and eddy diffusivity included in equation B.4 and equation B.5 are given by

$$\nu_{TOT} = \nu_{T,s} + \nu_{T,l}$$

$$\alpha_{\theta,TOT} = f_w\left(\frac{k_T}{k_{TOT}}\right)\frac{\nu_{T,s}}{Pr_\theta} + (1 - f_w)C_{\alpha,\theta}\sqrt{k_T}\lambda_{eff}$$

The turbulent scalar diffusivity in equation B.1 to equation B.3 is defined as

$$\alpha_T = f_v C_{\mu,std}\sqrt{k_{T,s}}\lambda_{eff}$$

$$K_{TOT} = K_T + K_L$$

The model constants for the $k - kl - \omega$ transition model are listed below [34]

$$A_0 = 4.04, A_s = 2.12, A_v = 6.75, A_{BP} = 0.6$$

$$A_{NAT} = 200, A_{TS} = 200, C_{BP,crit} = 1.2, C_{NC} = 0.1, C_{R,NAT} = 0.02$$

$$C_{NAT,crit} = 1250, C_{INT} = 0.75, C_{TS,crit} = 1000,$$

$$C_{11} = 3.4 \times 10^{-6}, C_{12} = 1.0 \times 10^{-10}, C_R = 0.12, C_{\alpha,\theta} = 0.035$$

$$C_{SS} = 1.5, C_{\tau,1} = 4360, C_{\omega 1} = 0.44, C_{\omega 2} = 0.92$$

$$C_{\omega 3} = 0.3, C_{\omega R} = 1.5, C_{\lambda} = 2.495, C_{\mu,std} = 0.09$$

$$Pr_{\theta} = 0.85, \sigma_k = 1, \sigma_{\omega} = 1.17$$